Optoelectronic devices based on atomically thin semiconductors and photo-oxidised HfO_x

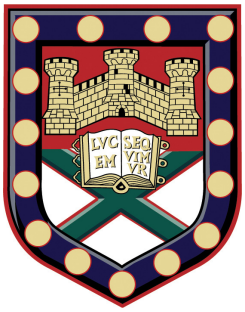

Submitted by Konstantinos-Andreas Anastasiou to the University of Exeter as a thesis for the degree of Doctor of Philosophy in Physics

August 2022

I certify that all material in this thesis which is not my own work has been identified and that no material has previously been submitted and approved for the award of a degree by this or any other university.

I acknowledge financial support from the Engineering and Physical Sciences Research Council (EPSRC) of the United Kingdom, via the EPSRC Centre for Doctoral Training in Metamaterials (Grant No. EP/L015331/1).

Konstantinos-Andreas Anastasiou

...ὡς οὐδὲν γλύκιον ἧς πατρίδος οὐδὲ τοκήων
γίγνεται, εἴ περ καί τις ἀπόπροθι πίονα οἶκον
ναίῃ ἐν ἀλλοδαπῇ ναίει ἀπάνευθε τοκήων.

Homer, *Odyssey*, IX. 34-36

ACKNOWLEDGEMENTS

A PhD is the result of hard work, but behind that there is a plethora of people that guide, support and motivate the candidate. Here I have the opportunity to thank the people that surrounded me all these years.

First of all, I would like to thank my supervisors, Prof. Saverio Russo and Prof. Monica Craciun. Saverio gave me the opportunity to become part of his group and mentored me to become an experimental scientist. In addition he gave me the freedom to work and pursue different and innovative ideas without putting unnecessary pressure. Also, I would like to thank all my colleagues with whom I shared many experiences and exciting ideas all these years. When I first joined the group, Jake and Adolfo undertook the task of introducing me to the experimental techniques and -mainly- mindset. A huge thanks to Agnes, with whom I started together, shared the wall between our desks for three and a half years (apologies for the silly donkey that kept falling all the time!) but mainly we shared our troubles, ideas and thoughts about the world. It was really a pleasure working with you and is a greater pleasure to consider you my friend. I would also like to thank the rest of the group members, Ioannis, my "young-padawan" Otto, Rosanna, Jonas, Janire, Kieran, Conor and Freddie for their help and support.

Everyone is defined by their family and I can't even describe how lucky and grateful I am for mine. My parents, Katerina and Ilias, made me who I am today by always being by my side, supporting me in every turn of the way and giving me their opinion and advice. Thank you very much for everything! I really have no words to express my gratitude, so the minimum thing I can do is to dedicate this thesis to you.

Furthermore I would like to thank my friends (and relatives) Anna, Charis, Vasilis, Dimitris, Nikos, Natasa, Kostas, Stelios, Vasilis, Eleftheria, Aphrodite, Penelope, Mary, Alexandros, Serge, Siva, Melissa, David, Sebastian and Bob who all played an important part in my life and with whom I shared many enjoyable moments.

Last and most importantly, I want to thank my partner Anna, with whom I've changed 3 cities and as many countries. Nothing would have been the same without you and for sure this thesis wouldn't exist. All these years you drive me forward and fill my life with love, happiness, excitement and...cats (thank you too Gizmo and Moca)! Thank you for everything, the best is yet to come.

Konstantinos Andreas Anastasiou
Bern
April 2022

ABSTRACT

The direction of research in solid state physics and technology has changed since the discovery of graphene. Now, a plethora of two-dimensional materials are being thoroughly investigated for their unique properties as well as for their implementation in next-generation optoelectronic devices. Of course, much effort is needed in order to reach the current level of modern electronics which is based on decades of research and development.

For example, the level of miniaturisation modern technology requires can be achieved with atomically thin materials, driving Moore's Law forward. Conventional dielectrics exhibit high leakage currents when their dimensions are reduced to the nano-scale and the need for alternative materials compatible with two-dimensional electronics arises. However, the techniques that are being used for the growth and processing of conventional semiconducting materials are not always suitable with two-dimensional materials, which need special handling. These are some of the points that will be addressed in this PhD dissertation.

Here, a new method for generating a fundamentally two-dimensional high-k dielectric which can be automatically incorporated in atomically thin optoelectronics devices is presented. The photo-oxidation of hafnium disulfide, HfS_2, is a straight-forward, non-invasive process that can be used to oxidise pristine few-layered HfS_2, opening new paths for applications ranging from optoelectronics to photonics. The resulting dielectric, Hafnium dioxide, HfO_2, exhibits outstanding properties that exceed those of silicon dioxide, SiO_2 and its atomically thin nature makes it an ideal insulating layer for next-generation nano-electronics.

Finally, the last part of this thesis is dedicated to a novel, CVD-grown, n-type monolayer of tungsten diselenide, WSe_2. This is the first time negatively doped CVD-grown WSe_2 is reported, which opens the possibility of choosing the doping of the

two-dimensional semiconductor before fabrication. For investigating and characterising this novel material, field-effect transistors are fabricated and characterised optoelectronically, shining light on the carriers' behaviour and the ability of the material in light-detection applications. Vacuum and ambient annealing of the WSe_2 based devices highlights a possible way to control the doping level of the material, and thus the electrical behaviour of the devices.

CONTENTS

LIST OF FIGURES

ACRONYMS

2D two-dimensional.
AC Alternating Current.
AFM Atomic Force Microscopy.
ALD Atomic Layer Deposition.
BNC Bayonet Neill–Concelman.
CCD Charge-Coupled Device.
CNP Charge Neutrality Point.
CVD Chemical Vapour Deposition.
DC Direct Current.
DI de-ionised.
DOS Density of States.
EDX Energy-dispersive x-ray spectroscopy.
EL electroluminescence.
EM Electromagnetic.
FBZ First Brillouin Zone.
FET Field Effect Transistor.
FL Few Layer.
hBN hexagonal boron nitride.
HRS high-resistance state.
IPA Propan-2-ol.
IQE Internal Quantum Efficiency.
IR infra-red.
LRS low-resistance state.
ML monolayer.
MOCVD Metal-Organic Chemical Vapor Deposition.
PB Photobolometric.
PC Photoconductive.
PCB Printed Circuit Board.
PDMS Polydimethylsiloxane.
PG Photogating.
PL photoluminescence.
PMMA Poly(methyl 2-methylpropenoate).
PTE Photothermoelectric.
PV Photovoltaic.
ReRAM resistive switching Random Access Memories.
RIE Reactive Ion Etching.
RRS resonant Raman scattering.
SPCM Scanning Photo-Current Mapping.
SQW single-quantum well.
STEM Scanning Transmission Electron Microscopy.
TEM Transmission Electron Microscopy.
TLM Transfer Length Method.
TMD transition metal dichalcogenides.
TP Topology.
UV ultra-violet.
vdW van der Waals.

1

THEORETICAL BACKGROUND

INTRODUCTION

In this chapter the relevant background theory that describes and explains the acquired experimental results in this PhD work will be presented. Historically, graphene was the first two-dimensional (2D) material which was isolated and characterised, making it the most well-studied 2D material. It is the material that paved the road for the research of atomically thin materials and the discovery of their unique properties that will be presented here.

In the research presented here, graphene was neither studied nor played a significant role other than being used as a material for electrodes in heterostructures, due to its unique electrical properties. This is the main reason the first section of this chapter is dedicated to the study of the basic structural and optoelectronic properties of this material. Without taking advantage of its unique transport properties, the performance of the heterostructures would be severely hindered.

In the second section, the main properties of transition metal dichalcogenides (TMD)s, which were exclusively used in the presented research, are summarised. However, due to the wide variety of materials and properties, only the most important ones will be presented in this chapter, emphasising on their diverse crystal structures and their unique optoelectronic properties, such as the large exciton binding energies and the number of layers dependent bandgap. More details for individual TMDs can be found at the relevant research chapters.

Finally, the main mechanisms of photocurrent generation in TMDs will be discussed. Those include the *photovoltaic*, the *photothermoelectric*, the *photoconductive*

and the*photogating* effects. It is important to highlight that there are several other mechanisms that give rise to photocurrent, even inTMDs, but those are the most important ones. Understanding these mechanisms is important for research in photodetectors and photosensitive devices in general.

1.1 GRAPHENE

Carbon is one of the most abundant elements on Earth and the Universe in general [1–3]. Also, it is the basic element of all known organic life and for that reason there is a dedicated branch of chemistry, called organic chemistry, that studies the structure, properties and reactions of organic compounds (compounds which contain carbon-carbon covalent bonds) [4]. The most abundant of the 3 natural isotopes of carbon (carbon-12) is formed in the nuclei of stars as a byproduct of fusion (triple-alpha process) or catalytic (C-N-O cycle) reactions and it is ejected in the interstellar medium by stellar winds, novae and supernovae [1,3,5,6]. Due to its valency (it can form 4 hydrogen bonds), it can form many different allotropes, with graphite and diamond being the most recognisable [7]. Graphite is the most common form of carbon on Earth and it's formed of stacked atomic layers of carbon atoms, weakly coupled by van der Waals (vdW) interactions [7]. Each layer has carbon atoms arranged in a two-dimensional honeycomb lattice. A single, isolated layer is called *graphene* and is one of the most studied and promising materials since it was first isolated in 2004 [8].

1.1.1 *Crystal Structure of Graphene*

Graphene and its electronic structure have been described since 1947 [9], but it was its isolation and electrical study by K.S. Novoselov and A.K. Geim in 2004 [8] that ignited the interest of the scientific community on the material. The σ bonds that are formed because of the sp^2 hybridization between one s and two p orbitals, give graphene its structural flexibility and electronic properties [10]. The honeycomb crystal lattice of graphene is shown in Figure 1.1. It is a triangular Bravais lattice, with a rhombus unit cell, described by the primitive lattice vectors

$$\vec{a_1} = \frac{\alpha}{2}\left(3, \sqrt{3}\right), \qquad \vec{a_2} = \frac{\alpha}{2}\left(3, -\sqrt{3}\right), \tag{1.1}$$

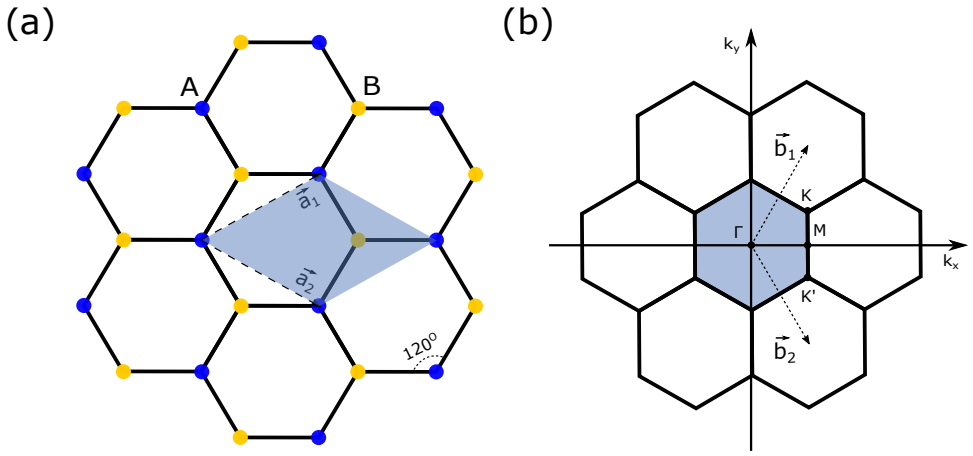

Figure 1.1: Crystal structure of graphene. (a) Honeycomb lattice of graphene in real space. This lattice can be decomposed in 2 Bravais sub-lattices, shown as A (blue) and B (gold), where each dot represents a position of a carbon atom. $\vec{a_1}$ and $\vec{a_2}$ are the lattice vectors. (b) Reciprocal lattice of graphene with FBZ (shaded area), the high symmetry points Γ, K, K', M and the lattice vectors $\vec{b_1}$ and $\vec{b_2}$.

where $\alpha \simeq 1.42$ Å is the nearest-neighbour distance between carbon atoms. The unit cell consists of 2 carbon atoms (A and B). The reciprocal lattice is also triangular with lattice vectors

$$\vec{b_1} = \frac{2\pi}{3\alpha}\left(1, \sqrt{3}\right), \qquad \vec{b_2} = \frac{2\pi}{3\alpha}\left(1, -\sqrt{3}\right), \tag{1.2}$$

while the First Brillouin Zone (FBZ) is hexagonal, with the high-symmetry points K, K' (also named *Dirac points*) and M. The positions of these points in momentum space are given by:

$$\vec{K} = \left(\frac{2\pi}{3\alpha}, \frac{2\pi}{3\sqrt{3}a}\right), \qquad \vec{K'} = \left(\frac{2\pi}{3\alpha}, -\frac{2\pi}{3\sqrt{3}a}\right), \qquad \vec{M} = \left(\frac{2\pi}{3\alpha}, 0\right). \tag{1.3}$$

As we'll see in the next section, exactly at these points the band structure of monolayer (ML) graphene exhibits specific behaviour that determines the unique properties of this material.

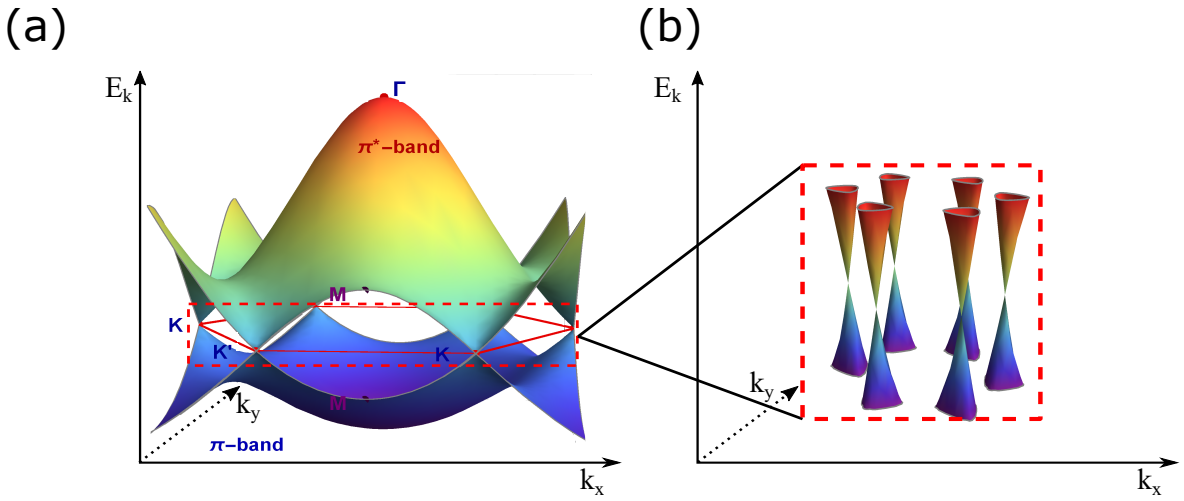

Figure 1.2: Electronic band structure of graphene. (a) Energy dispersion of ML graphene. The conduction (π^*)- and valence π-bands intersect at K and K' points. (b) Detailed depiction of the linear part of the band structure at the K and K' points.

1.1.2 *Electronic Structure of Graphene*

The electronic band structure of graphene can be approximated by using the tight-binding model[11] and considering only the π-states and nearest-neighbour hopping terms (parameter t), in order to have only hopping between different sub-lattices. Figure 1.2 (a) shows the band structure of ML graphene in nearest-neighbour tight-binding model. Whilst Figure 1.2 (b) shows the zoomed-in region around the K and K' points, where the linear dispersion of energy is clearly seen.

The Hamiltonian of graphene for the nearest-neighbour tight-binding model is described by the matrix:

$$\hat{H}(\vec{\boldsymbol{k}}) = \begin{pmatrix} 0 & tS(\vec{\boldsymbol{k}}) \\ tS^*(\vec{\boldsymbol{k}}) & 0 \end{pmatrix}, \tag{1.4}$$

where t is the hopping parameter, $\vec{\boldsymbol{k}}$ the wavevector and

$$S(\vec{k}) = \sum_{\vec{\delta}} e^{i\,\vec{k}\,\vec{\delta}} = 2\exp\left(\frac{ik_x\,\alpha}{2}\right)\cos\left(\frac{k_y\,\alpha\sqrt{3}}{2}\right) + \exp(-ik_x\alpha)\,, \tag{1.5}$$

is the *geometrical form factor*.

By solving the eigenvalues problem of the time-independent Hamiltonian (Eq. 1.4) the energy spectrum of ML graphene can be derived. The resulting spectrum is:

$$\begin{aligned} E(\vec{k}) &= \pm\, t|S(\vec{k})| \;= \pm t\sqrt{3 + f(\vec{k})}, \\ f(\vec{k}) &= 2\cos\left(\sqrt{3}\,k_x\alpha\right) + 4\cos\left(\frac{\sqrt{3}}{2}k_y\,\alpha\right)\cos\left(\frac{3}{2}k_x\,\alpha\right), \end{aligned} \tag{1.6}$$

where the + sign applies to the upper (π^*) and the − sign to the lower (π) band.

By substituting the coordinates of the high-symmetry points K and K' (Eq. (1.3)) to Eq. (1.5), we find that $S(\vec{K}) = S(\vec{K'}) = 0$. Thus, the two bands cross at this point forming a conical point, as it is depicted in Figure 1.2 (b). Eq. (1.4) can be expanded around these points (K and K')[1]

$$\hat{H}_K(\vec{\boldsymbol{q}}) = \hbar v_F \begin{pmatrix} 0 & q_x - iq_y \\ q_x + iq_y & 0 \end{pmatrix} = \hbar v_F\left(\sigma_x k_x + \sigma_y k_y\right), \tag{1.8}$$

where $\vec{k} = \vec{K} + \vec{q}$, $\vec{q}$ is the momentum relatively to the Dirac points, $v_F = 3\alpha|t|/2\hbar$ is the Fermi velocity at the Dirac points, s_i, $i = x, y$ are two Pauli matrices and $|\vec{q}| \ll \left|\vec{K}\right|$. The electronic dispersion of graphene is given by the eigenvalues of Eq.(1.8) and is found to be[9,10]:

$$E(\vec{q}) \approx \pm v_F|\vec{q}| + \mathcal{O}\left[(q/K)^2\right]. \tag{1.9}$$

Experimentally, $v_F \simeq c/300 \simeq 10^6\,\mathrm{m\,s^{-1}}$, where c is the velocity of light in vacuum.

[1] That is the result for point K. The general expression for both points is:

$$\hat{H}_K(\vec{\boldsymbol{q}}) = \hbar v_F \begin{pmatrix} 0 & \lambda q_x - iq_y \\ \lambda q_x + iq_y & 0 \end{pmatrix} = \hbar v_F\left(\lambda\sigma_x k_x + \lambda\sigma_y k_y\right), \tag{1.7}$$

where $\lambda = \pm 1$ for K and K' respectively.

For undoped graphene,the Fermi Energy (E_F) falls precisely at the crossing point of the two bands also known as conical points. This charge neutral level of E_F separates the filled valence band from the empty conduction band, implying that graphene is a *gapless semiconductor*. Although, due to quantum relativistic effects, graphene has a finite conductivity at $T = 0$K despite the vanishing Fermi surface, making graphene a *semimetal* [12,13].

The most important difference between Eq.(1.9) and the energy dispersion for massive charges, $E(\vec{k}) = \hbar^2 k^2/2m_{e^-}$, is that the Fermi velocity in Eq.(1.9) is independent of the energy or the momentum. Thus, Eq.(1.9) is similar to the energy dispersion for massless photons. This is in contrast to the usual dependence of the Fermi velocity for massive charges in a lattice, $v_F = p_F/m = \sqrt{2E_F/m}$, for which the velocity is a function of the energy of the charge carriers.

In order to describe the electron and holes states at the area where the Fermi energy is very close to the Dirac points, the effective Hamiltonian needs to be expanded around K and K' and momentum $\vec{q}$ should be replaced by its corresponding quantum operator, $q_i \to -i\boldsymbol{\nabla}_i$. Then, Eq.(1.8) takes the form:

$$\hat{H}_K = -i\hbar\, v_F \sigma_i \boldsymbol{\nabla}_i \,, \tag{1.10}$$

where σ_i , $i = x, y$ are the Pauli matrices. The above Hamiltonian is a 2D Dirac Hamiltonian for *massless fermions*, but instead of the light velocity c there is the parameter v_F (Fermi velocity).

The formula that relates the Fermi wavenumber (k_F) with the carrier density (n) is:

$$k_F = \sqrt{\frac{4\pi n}{g_s g_v}} \,, \tag{1.11}$$

where g_s and g_v are the spin and valley degeneracy, respectively (for graphene $g_v = 2$, since K and K' are not equivalent). That means that near the Dirac points, the Fermi energy can be calculated by combining Eq. (1.9) and Eq. (1.11), producing the following result:

$$E_F = \hbar v_F k_F = \hbar v_F \sqrt{\pi n} \,. \tag{1.12}$$

Finally, by following the expression for the two-dimensional (2D) Density of States (DOS)

$$D(E) = \frac{g_s g_v}{(2\pi)^2} \int\limits_{E(\vec{k})=const.} \frac{dl_E}{|dE/dk|}\,, \tag{1.13}$$

graphene's DOS is found to be:

$$D(E) = \frac{2}{\pi}\frac{|E|}{\hbar^2 v_F^2}\,. \tag{1.14}$$

1.1.3 *Transport Properties of Graphene*

The simplest way to probe the electrical transport properties of graphene is by fabricating and fully characterising a Field Effect Transistor (FET) (Figure 1.3(a)). In a typical graphene FET, a layer of graphene is deposited on top of a heavily doped (n or p) Si/SiO_2 substrate, where the thermally grown SiO_2 layer acts as a gate dielectric, with relative static permittivity $\epsilon_r \simeq 3.9$[14].

The voltage applied to the Si gate terminal (V_g) of the transistor controls the carrier concentration (n) and the type of the carriers (electrons, e^-, or holes h^+) in the channel. Graphene shows ambipolar behaviour, since it is a gapless material, thus a positive gate bias $V_g > 0$ will induce electrons in the graphene channel, while negative gate bias $V_g < 0$ will induce holes in the channel and the device will show a p-type conductivity, as depicted in Figure 1.3(b).

The geometry of the device resembles that of a parallel plate capacitor, consequently the relation between the gate bias (V_g) and the induced carrier concentration is:

$$n_i = \frac{\epsilon_0 \epsilon_r V_g}{q_e d} = \alpha V_g\ ,\ i = e^-, h^+\,, \tag{1.15}$$

where ϵ_0 and ϵ_r are the vacuum and gate dielectric permittivities, q_e the elementary charge and d the thickness of the gate dielectric. Almost all the devices presented in this thesis bear SiO_2 as gate dielectric, with a thickness of 280 nm. This thickness of the oxide, allows a safe sweeping of the gate bias in a region of about ±100V. For these devices, $\alpha = 7.698 \times 10^{10}\ \mathrm{cm^{-2}\,V^{-1}}$, and so an upper limit for the induced carrier concentration can be obtained; this is found to be $n \simeq \pm 1 \times 10^{13}\,\mathrm{cm^{-2}}$ which

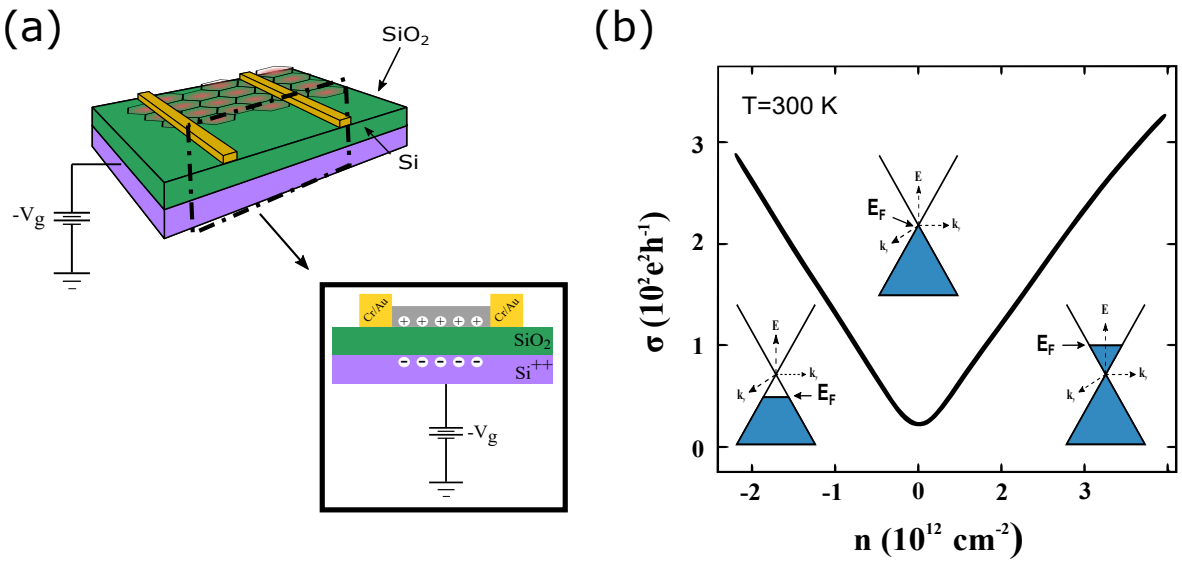

Figure 1.3: Conductivity of a graphene FET (a) Schematic of a pristine graphene Field Effect Transistor (FET) device on Si/Si^{++}, with deposited Cr/Au contacts, under negative gate bias. (b) Room temperature conductivity (σ) with carrier density. By applying gate bias, carrier concentration (thus, the Fermi energy as well) of the channel is accordingly adjusted.

when introduced to Eq. (1.12) yields a change to graphene's Fermi energy level of $\Delta E_F \simeq 370\text{meV}$.

Owing to the atomically thin nature of graphene, the charges in this material are truly confined to a 2D space. The Drude model predicts that the electrical conductivity (σ) varies linearly with the charge concentration (n) (see Figure 1.3(b)):

$$\sigma_i = n_i q_e \mu_i \ , \ i = e^-, h^+ \ , \tag{1.16}$$

where μ_i is the mobility of the charge carriers. However, this behaviour is not valid for $n_i \to 0$, where conductivity approaches a non-zero finite value, $\sigma_0 \propto q_e^2/h$.[15] By combining Eq. (1.16) with Eq. (1.15) a relation between conductivity and gate voltage can be derived

$$\sigma_i = \alpha q_e \mu_i V_g \ , \ i = e^-, h^+ \ . \tag{1.17}$$

Since the isolation of graphene in 2004[8], the research on it has revealed its remarkable transport properties, such as a very large values of room temperature charge carrier mobility (up to $2 \times 10^5 \mathrm{cm}^2\,\mathrm{V}^{-1}\,\mathrm{s}^{-1}$)[8,16] and an electron mean free path of $\sim 0.4\,\mu m$[8]. For low temperatures the observed mobilities are even higher, from $\sim 3.5 \times 10^4 \mathrm{cm}^2\,\mathrm{V}^{-1}\,\mathrm{s}^{-1}$[17] up to $\gtrsim 10^6 \mathrm{cm}^2\,\mathrm{V}^{-1}\,\mathrm{s}^{-1}$[18,19]. Of course, different substrates, device geometries, annealing procedures and many other factors can affect the value of the charge carrier mobility.

1.1.4 *Optical Properties of Graphene*

Apart from its unusual electrical and mechanical properties, graphene also exhibits unique optical properties. The light-matter interactions in graphene are surprisingly strong, leading to very high absorbance for the single-atom layer of $\sim 2.3\%$. This is the property that allowed its initial discovery under an optical microscope. As a result, optical spectroscopy is a powerful tool for probing graphene's physics.

The source of this strong coupling between graphene atoms and photons lies in the delocalised π-orbitals of the graphene electrons[9,10,20]. Furthermore, the optical properties of graphene can be tuned through electrical gating[21–23], structural engineering[24,25], and coupling between graphene layers[26]. Controlling the optical properties of graphene opens new ways both for understanding the physics of graphene and for applications in tunable photonics and optoelectronics.

1.1.4.1 *Optical Absorption, Transmission and Reflection*

In Figure 1.4 (a) the two bands (conduction and valence) of graphene are shown. At the touching point between the conduction and valence bands, the energy dispersion is linear leading to the so-called *Dirac cones*. For excitation wavelengths shorter than far infra-red there are direct interband transitions (from the valence to the conduction band) which are represented by the blue arrows, that govern the optical response of graphene[21]. By using the tight-binding model, the optical sheet conductivity that arises from these interband transitions can be calculated[28,29] and, especially for pristine graphene at $T = 0\mathrm{K}$, it is found that within the linear dispersion regime, it is independent of frequency:

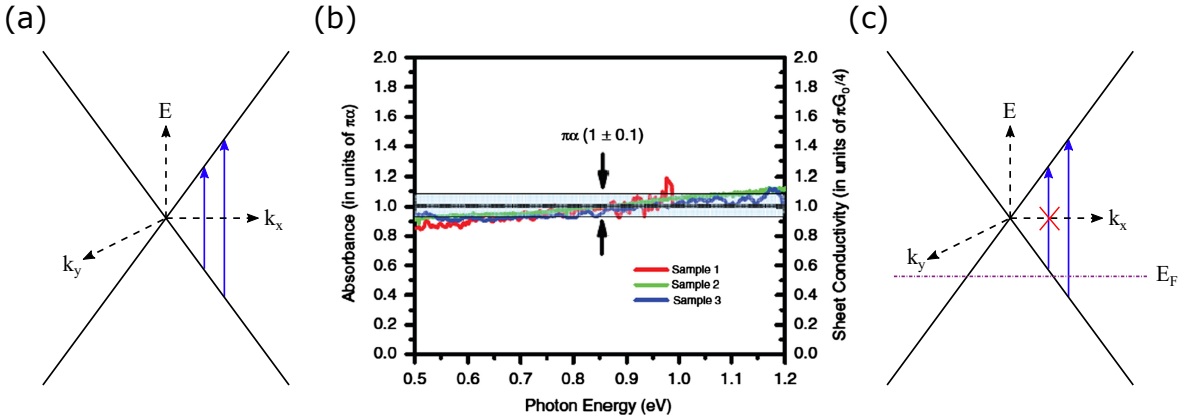

Figure 1.4: Optical sheet conductivity of graphene. (a) Dirac cone and optical interband transitions in graphene. (b) The optical sheet conductivity (right axis) and the sheet absorbance of three different samples of graphene over the photon energy range of 0.5 eV to 1.2 eV. The black horizontal line corresponds to the universal value of $\pi\alpha = 2.293\%$ for the sheet absorbance. (Adapted with permission [27]). (c) Interband transitions in hole-doped graphene through applied gate bias. Optical transitions at photon energies greater than $2|E_F|$ are allowed, but those with energies less than $2|E_F|$ are suppressed.

$$\sigma(\omega) = \frac{\pi q_e^2}{2h}. \tag{1.18}$$

This quantity is defined only by fundamental constants and does not depend on material parameters. The equivalent absorbance is:

$$A(\omega) = \frac{4\pi}{c} \cdot \sigma(\omega) = \pi\alpha \simeq 2.3\ \%, \tag{1.19}$$

where α is the fine structure constant [30,31]. For photon energies between 0.5 eV and 1.2 eV this value for absorbance remains largely constant, which means that it is not significantly affected by detailed nature of the sample or its local environment [32], as seen also in Figure 1.4 (b), where the frequency-dependent absorbance for three different graphene samples is characterised. Over this spectral range, different samples show equivalent responses not influenced by the detailed nature of the sample or its environment.

Moreover, the absorbance is largely frequency independent, with an average value

over the specified spectral range of $A = (2.28 \pm 0.14\%)$ consistent with the universal value of $\pi\alpha = 2.29\% \approx 2.3\%$[27,32]. The behaviour is not completely frequency independent, as we can see mostly for higher photon energies. The reason for this is that the band structure of graphene is not linear for energies that are not close to the Fermi energy.

As the sheet conductivity of graphene is a universal constant, its observable quantities like *Transmittance* and *Reflectance* are also universal. Indeed, for normal light incidence, the transmittance and reflectance of graphene are given by the following equations[31]

$$T = (1 + 1/2\pi\alpha)^{-2}\,, \quad R = 1/4\pi^2\alpha^2 T. \tag{1.20}$$

This dependance of the reflectance, transmission and absorbance of graphene only on fundamental parameters is regarded as a result of its structure and electronic properties. As expected, the transmittance and reflectance of graphene follow the behaviour of absorbance by remaining relatively stable across almost the entire optical spectrum[31].

Electrical doping can effectively change the Fermi energy of graphene, as well as its optical absorption by changing the interband absorption through Pauli blocking. As shown in Figure 1.4 (c), in these cases the interband transitions with $E < 2|E_F|$ are completely suppressed and thus, the optical response of graphene becomes highly tunable. In a FET, the carrier concentration and the Fermi energy can be tuned by applying a gate bias (see Section (1.1.2), Eq. (1.12) and (1.15)).

In doped graphene, the optical absorption can be described by the formula[28,32]

$$\sigma(\omega, T) = \frac{\pi q_e^2}{4h}\left[\tanh\left(\frac{\hbar\omega + 2E_F}{4k_B T}\right) + \tanh\left(\frac{\hbar\omega - 2E_F}{4k_B T}\right)\right] \tag{1.21}$$

showing how by controlling the Fermi energy it is possible to change the optical properties of graphene.

1.2 TRANSITION METAL DICHALCOGENIDES

The isolation and study of graphene marked the beginning of a new era for condensed matter physics, that of two-dimensional (2D) materials. Among these, the layered semiconducting *Transition Metal Dichalcogenides* (TMDs) present interesting opto-

electronic properties[33,34] due to the existence of an energy gap in their electronic structure. This brings them in the center of research of fundamental phenomena and a wide spectrum of applications[35,36].

Several studies[37–40] have shown that the band structure of these materials changes drastically depending on whether the examined flake is monolayer or multi-layer. Specifically, the indirect bandgap observed in multilayer TMDs is transformed to direct for monolayer TMDs[41], revealing the crucial role of interlayer hopping of carriers in these compounds[42]. In general, their electronic properties are highly tunable since they are sensitive to external conditions such as temperature, pressure and strain. This makes them ideal candidates for applications in optoelectronics[35].

In addition, there is a high interest in exploring the implementation of these materials in spintronics and valleytronics nanodevices. Due to the strong spin-orbit interaction present in semiconducting TMDs and the absence of inversion symmetry in a single atomic sheet of the material, the spin degeneracy of the energy bands is lifted[43]. Due to the conservation of time reversal symmetry, the spin splitting in different valleys is opposite. This phenomenon is called *spin-valley coupling*[44]. The coupling of the valley, the spin and the layer degrees of freedom in semiconducting TMDs opens new possibilities for applications in valleytronics and spintronics nanodevices[45–48].

Finally, manipulation of the optoelectronic properties of atomically thin TMDs has been exhibited as a result of the application of external strain, which is attributed to their high stretchability[49]. *Strain engineering* is the field that studies exactly how the physical properties of materials can be modified at will by controlling the external strain field applied to them. Especially atomically thin TMD materials are considered perfect candidates for the implementation of these techniques. For example, strain engineering has been used to probe the piezoelectric properties of 2D TMDs like $MoSe_2$, a material which is not piezoelectric in its bulk configuration. The case changes entirely for monolayer and few-layer $MoSe_2$, which becomes piezoelectric[50]. Furthermore, exciton and charge carrier funnels have been created by using non-uniform strain profiles which allow the localised concentration of carriers on a $MoSe_2$ photovoltaic device. This results in a broad range of solar spectrum being captured[51].

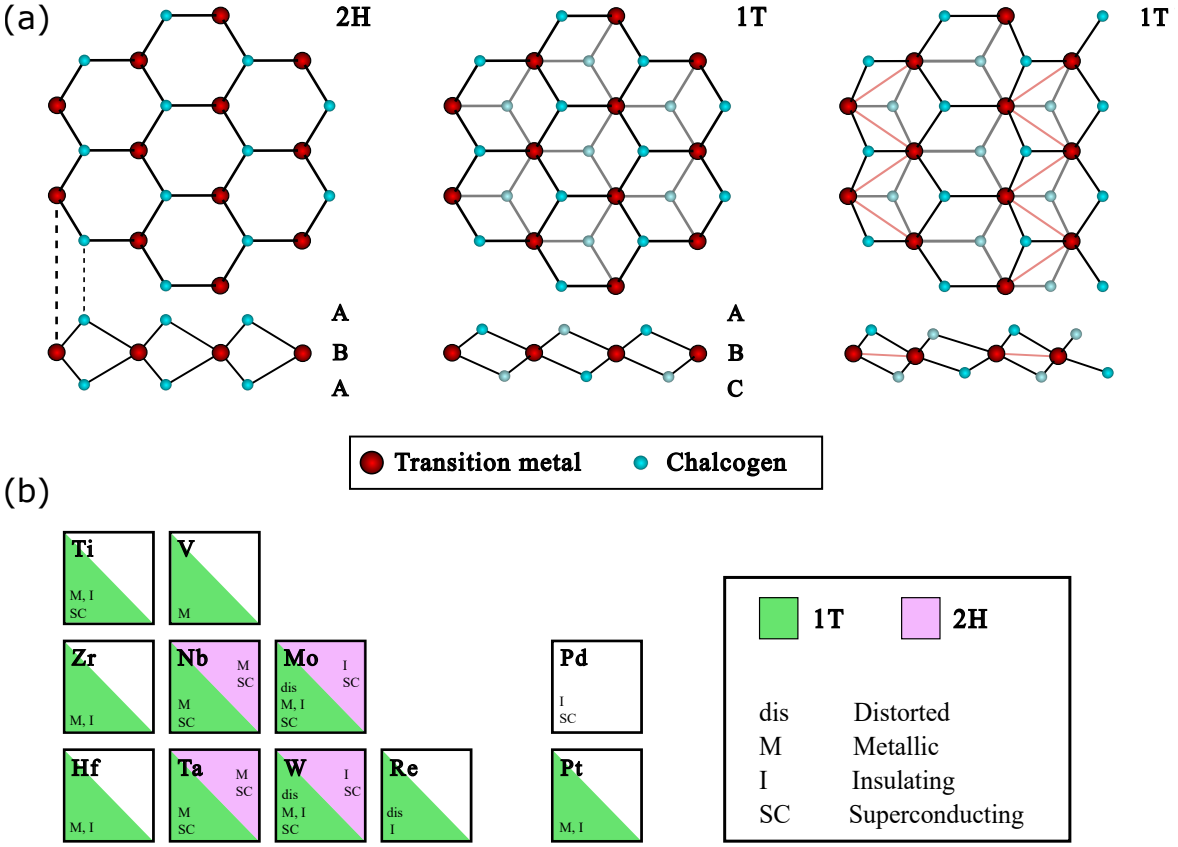

Figure 1.5: Crystal structure of TMDs. (a) Lattice arrangement of transitions metal dichalcogenides in different phases, the trigonal prismatic (2H), the distorted octahedral (1T) and the dimerised (1T'). (b) Structural phase of known TMDs depending on their respective transition metal.

1.2.1 *Crystal Structure and Electronic Properties*

TMDs consist of one transition metal (e.g. Mo, W, etc.) and two chalcogens (S, Se or Te), with a general chemical formula of MX_2, where M is the transition metal and X the chalcogen. Their crystal structure resembles this of graphene (Section 1.1.1), but since a monolayer of a TMD consists of three stacked atomic planes, the thickness of each layer is higher than that of graphene and it is approximately 6Å. The intralayer bonds are covalent, whereas the different layers are held together by vdW forces which result in strong anisotropy of physical properties (e.g. electrical conductivity) and make mechanical exfoliation easier.

TMDs crystallise in different structural phases, depending on the coordination of the metal atoms. The most common crystalline structural phases result from *trigonal prismatic* ($2H$) and *octahedral* ($1T$) coordination of metal atoms (Figure 1.5 (a)).

Another way of approaching the different structural phases is in terms of different stacking orders of the three atomic planes (X-M-X) which make the individual layers of TMDs. An A-B-A type of stacking (Figure 1.5 (a)) where the chalcogen atoms of the upper and lower atomic planes seem to occupy the same position, A, in the direction perpendicular to the layer, result to 2H crystalline phase. On the contrary, 1T crystalline phase is attained by an A-B-C stacking order. In each case, it is the combination between the metal and chalcogen atoms that determines which structural phase is thermodynamically stable. The partial periodic table in Figure 1.5 (b) summarises the existing structural phases, of the TMD compounds, indicating the presence of distorted structural phases and observed electronic phases, depending on their building transition metal.

Possible lattice distortions lower the periodicity of multilayer TMDs and can possibly lead to the formation of metal-metal bonds. For example, the dimerisation of the 1T phase of TMDs that belong to the VI group results in the 1T' distorted phase.

The crystallisation phase has great impact on the electronic properties of TMDs, meaning that different polymorphs of the same material exhibit different behaviour. Two well known examples are MoS_2 and WSe_2, which have semiconducting behaviour in the 2H phase and metallic in the 1T phase[52,53].

As in graphene, the FBZ of a monolayer TMD in the 2H phase is hexagonal. The high symmetry points K and K' of a ML TMD are the points where the direct bandgap appears. Although, when the same material is in its bulk form, the bandgap is indirect and it is located between the Q and Γ points. This transition is related to the increase in quantum confinement in the out-of-plane direction (given by the layered nature), which causes an increase in the indirect gap, without affecting the direct gap at K and K'[54–56]. Thus, the band structure of a ML TMD can be compared with that of *gapped* graphene but with broken inversion symmetry[57], since the metal and chalcogen atoms belong to different atomic layers. It can be described by a pair of degenerate conduction and valence bands at the K and K' points.

In Figure (1.6) the concept of broken symmetry and the valley-dependent optical selection rules in TMDs are described. The breaking of the inversion symmetry observed

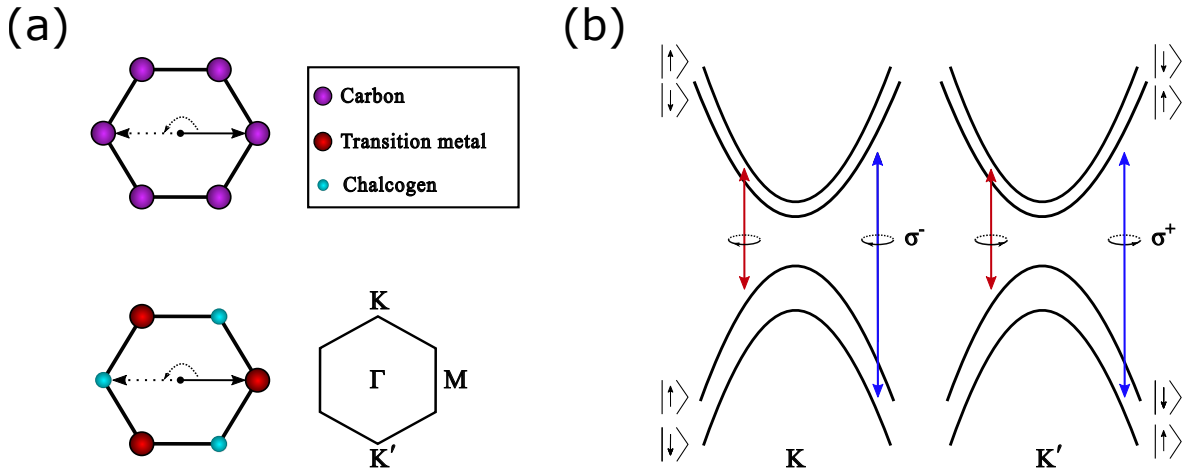

Figure 1.6: Broken inversion symmetry and valley-dependent optical selection rules in 2D TMDs. (a) Inversion symmetry in graphene's honeycomb crystal structure (top) and broken inversion symmetry in a corresponding TMD lattice (bottom). (b) Valley-dependent optical selection rules due to the lack of inversion symmetry. The electronic bands are spin-split around the K and K' points as a result of the spin-orbit interactions. The absorption of circularly polarised light corresponds to excitation of specific spin and only in a particular valley. Due to spin-orbit coupling this will define the momentum of the electron.

in TMD's allows contrasted circular dichroism in different k-space regions, leading to optical selection rules for interband transitions at the K and K' points. This results in the coupling of circularly polarized light exclusively with a specific spin, a process which defines the electron's momentum due to spin-orbit coupling. In the vicinity of the K (K') point, incoming left (right)-handed circularly polarized light σ^- (σ^+) will only excite spin-down (up) electrons[45,58]. The above concept is the cornerstone of *valleytronics*, where a specific valley can be used to store information, and TMDs seem possible candidates for the realisation of such devices[59].

1.2.2 *Optical Properties of TMDs*

The optical absorption, and the optical properties in general, of monolayer TMDs in the near-infrared (nIR) and visible regions of the Electromagnetic (EM) spectrum is dominated by direct transitions at the K and K' points[45,46,60]. The absorption spectrum of ML TMDs provides evidence of strong excitonic effects in the form of

sharp resonance features, even at room temperature[37]. Several theoretical[61,62] and experimental[63–65] studies have revealed that very large exciton binding energies can exist for monolayer TMDs, ranging from 0.5eV to as high as 1eV. This corresponds to an exciton Bohr radius (the distance of the electron-hole pair) of $\alpha_B \sim 1\text{nm} - 2\text{nm}$[66,67].

Apart from excitons, in single layer TMDs there have been observed higher-order quasi-particles including *trions* (bound states of a hole and two electrons, or vice-versa) in doped monolayer TMDs[68,69] and bi-excitons (bound states of two excitons), under pulsed optical excitations[70,71]. These quasi-particles in 2D TMDs have very high binding energies which surpass those found in conventional semiconductors about an order of magnitude. This makes the detection of these quasi-particles possible even at room temperature.

1.3 PHOTOCURRENT GENERATION MECHANISMS

There are many different mechanisms that generate photocurrent when light is impinging on a photodetector and most of the times more than one are simultaneously contributing to its total value. Depending on the material(s) that constitute the active channel, the metallic contacts and the geometry of the device in general, a specific mechanism can play more important role than the others and several can also not exist in a specific case.

When attempting a categorisation in terms of the nature of the phenomena the incident radiation produces, we can see two main categories of photocurrent generation mechanisms; *photonic* and *thermal* type. In the first case, the impinging light excites carriers inside the active channel of the detector producing electron-hole pairs, while in the latter it changes the temperature of the material leading to a change in a measurable quantity of the electrical output. Generally, photonic detectors exhibit a better performance than thermal detectors as their mechanism is faster because their output is the photoexcited carriers, resulting in a better signal-to-noise[72].

The main photonic mechanisms that generate photocurrent are: the *Photovoltaic (PV)* (or photoelectric) effect, the *Photoconductive (PC)* effect and the *edge* effect. Each of these mechanisms can be separated in several subcategories but such fragmentation is not contributing to the overall description of the phenomena attempted here. Similarly, the main thermal-type mechanisms are the *Photothermoelectric (PTE)*,

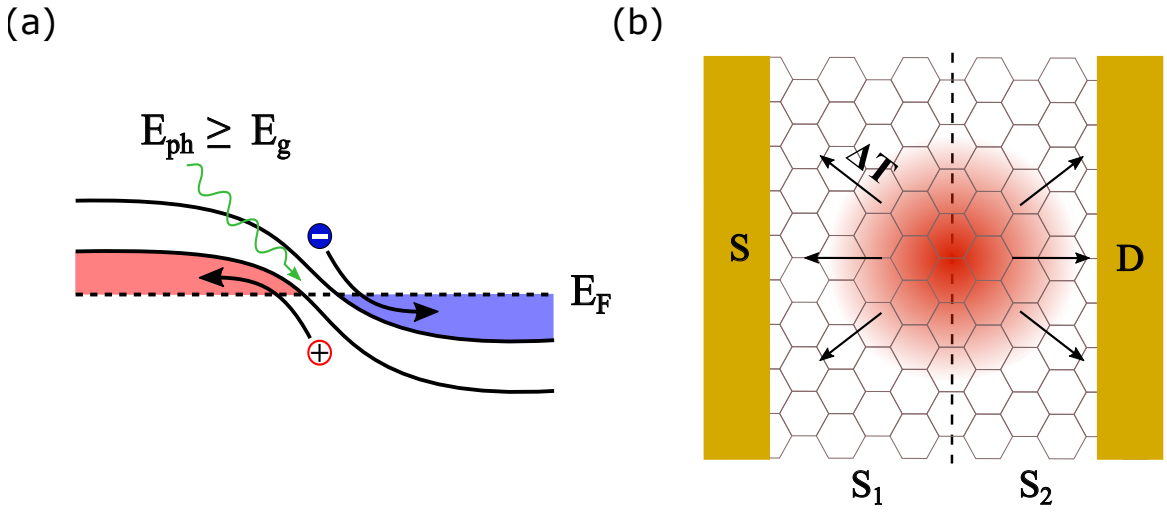

Figure 1.7: Photovoltaic and Photothermoelectric effects. (a) Schematic of the Photovoltaic (PV) effect in a p-n junction. The dashed line represents the Fermi energy (E_F) of the system. (b) Schematic of the Photothermoelectric (PTE) effect in a 2D FET. The temperature gradient, ΔT, created by impinging light, gives rise to voltage bias on the interface of two different metals or two areas with different doping. Panel (a) is reproduced from M. Buscema et al.[76] with permission from the Royal Society of Chemistry.

the *Photobolometric (PB)* and the *Topology (TP) enhancement* mechanisms. Here, only the main photocurrent generation mechanisms found in 2D photodetectors will be presented. The reader interested in a thorough analysis of all the photodetection mechanisms can check a plethora of review articles and books dedicated to photodetectors[72–75], not restricted to the references found here.

1.3.1 *Photovoltaic effect*

The Photovoltaic (PV) (or, photoelectric) effect is one of the most basic mechanisms of photodetection. It relies on the generation and subsequent separation of excitons by a built-in electric field. This can be due to a p-n junction[77–82], or a Schottky barrier formed at the interface between a 2D semiconductor and a metal contact[83,84] (for an analysis of the formation of Schottky barrier see Section 2.2.2.1). The definition of the PV effect doesn't necessarily include an electric field, but especially in the field of 2D materials it is narrowed down to the separation of the photoexcited carriers by a

built-in electric field. This electric field may also be produced, or enhanced, by means of an external voltage.

Although the separated carriers can be collected with a short-circuit configuration (no applied bias between the source and drain electrodes) they can also be accelerated by applying an electric field to the source and drain electrodes. In this case, the resulting photocurrent is proportional to the incident optical power

$$I_{pc} = \frac{\eta_i P_{opt}}{\hbar\omega_0} \frac{W}{L} \tau_c q(\mu_e + \mu_h) V_{sd} \,, \tag{1.22}$$

where η_i is the Internal Quantum Efficiency (IQE), $\hbar\omega_0$ the energy of the incident photon, W and L are the width and length of the active channel accordingly; τ_c is the photoexcited carriers' lifetime, μ_e and μ_h are the electron and hole mobilities and V_{sd} the applied voltage between the source and drain electrodes[75].

In Figure 1.7 (a), a schematic of the PV effect in a p-n junction (p-type semiconductor is on the left and n-type on the right, as indicated by the Fermi levels in the figure) is shown. When a photon of energy larger than the bandgap $E_{ph} > E_g$, is absorbed, an electron–hole pair is generated. The electron–hole pair is then separated and accelerated by the built-in electric field at the junction and collected from electrodes at the edges of the channel.

However, the PV effect is not the only mechanism found in photoconductive FETs, p-n junctions and differently doped regions of 2D materials. Specifically, a photovoltage resulting from the Photothermoelectric (PTE) effect (see Section 1.3.2) when metal-semiconductor contacts[85] or p-n juctions[86] are illuminated has been observed to contribute to the total photocurrent even more than the PV effect. Both of these mechanisms lead to moderate responsivities, $R \sim \mathrm{mA\,W^{-1}}$ [87].

1.3.2 *Photothermoelectric effect*

In the Photothermoelectric (PTE) effect, light-induced heating leads in a temperature gradient through a semiconductor channel, resulting to a temperature difference ΔT between its two ends. As a result of the Seebeck effect, this temperature difference can produce photovoltage (ΔV) at the junction

$$\Delta V = (S_1 - S_2)\, \Delta T \,, \tag{1.23}$$

where S_1, S_2 are the Seebeck coefficients of the two sides of the junction.

More generally, photovoltage is generated when exposure to light creates a temperature gradient ($\boldsymbol{\nabla} T(x)$) on a material with varying Seebeck coefficient, $S(x)$, then $\Delta V = \int S(x) \nabla T(x)\, dx$, as shown in Figure 1.7 (b). The Seebeck coefficient can be expressed using the Mott relation [88,89]

$$S = -\frac{\pi^2 k_B^2 T_h}{3\, q\sigma(E)} \left.\frac{\partial \sigma(E)}{\partial E}\right|_{E=E_F} = \frac{2\pi^2 k_B T_e}{3\, q T_F}\,, \tag{1.24}$$

where T_h is the temperature of the hot carriers, $T_F = E_F/K_B$ the Fermi temperature, σ the conductivity of the material, k_B the Boltzmann constant and q the electron charge. It is important to note that Eq. (1.24) assumes that the mobility is independent of Fermi energy E_F.

In PTE effect, photocurrent can exist without external bias voltage because of the light-induced photovoltage. Similarly, in the PV effect the built-in voltage is responsible for the separation and collection of the photoexcited carriers, without the need of an externally applied field. In the case of a heterojunction photodetector, the photocurrent produced by both mechanisms has the same direction and maximises when the light is spotted at the junction interface. As a result, the distinction of the two mechanisms is difficult.

According to the discussion in C. Yang et al., to identify the photocurrent generation mechanism there are three principles that should be followed [72]. First, in the case of PV detectors, photocurrent generation requires the incident photon energy be greater than the material bandgap. In contrast, for PTE detectors which are based on thermal effects, the spectral response is not limited by the bandgap. Second, PV detectors are based on a built-in electric field and generate a nonlinear current-voltage (I–V) curve, while PTE detectors can operate on a linear current–voltage (I–V) curve. In PV photodetectors, the photoresponse is limited to the area near the junction interface, whereas in PTE detectors the spatial distribution of photocurrents can be extensive. Third, the distinction between the different mechanisms can also be based on whether the spectral response is wavelength dependent. Specifically, the absorbance of the sensing material of a PTE detector is independent of wavelength [90]. The disadvantage of PTE photodetectors compared to the PV photodetectors is the relatively long response time of phonon-dominated transport, typically in the order of milliseconds.

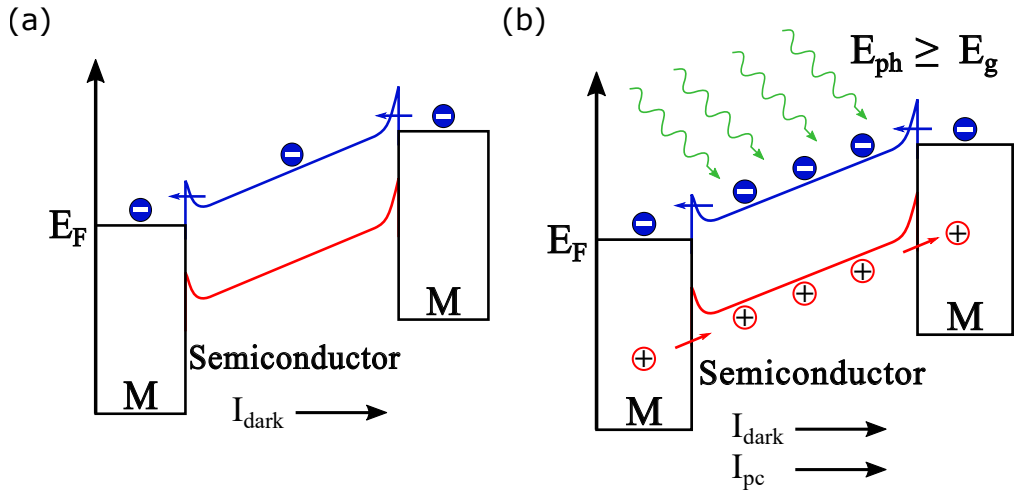

Figure 1.8: Photoconductive effect. Schematic of the Photoconductive (PC) effect in a 2D device in dark (a) and under illumination (b), where external bias has been applied between the source and drain electrodes. Reproduced from M. Buscema et al.[76] with permission from the Royal Society of Chemistry.

1.3.3 *Photoconductive and Photogating effects*

The Photoconductive (PC) effect is based on the photo-induced decrease of the resistance of the channel (increased conductance because of the excess carrier density) due to an increase to the concentration of free carriers upon photon absorption from the active layer. A descriptive schematic of the PC effect can be seen in Figure 1.8, where an external bias has been applied between the two metallic terminals of a 2D device. When the device is in dark conditions (Figure 1.8 (a)) there is a small current (dark current, I_{dark}) due to thermal excitation and the applied bias as well. However, upon illumination (Figure 1.8 (b)) with light of appropriate energy ($E_{ph} \geqslant E_g$) excitons (bound electron-hole pairs) are created. These excess carriers are separated by the applied bias voltage (V_{sd}) resulting in the measured photocurrent, which usually is orders of magnitude higher than the dark current. In comparison with the PV effect, if the bias voltage is not applied, the photocurrent of the photoconductive effect cannot be generated.

In heterogeneous structures or in the presence of disorder, the photoconductivity can be further affected by the emergence of an internal gate mechanism known as Pho-

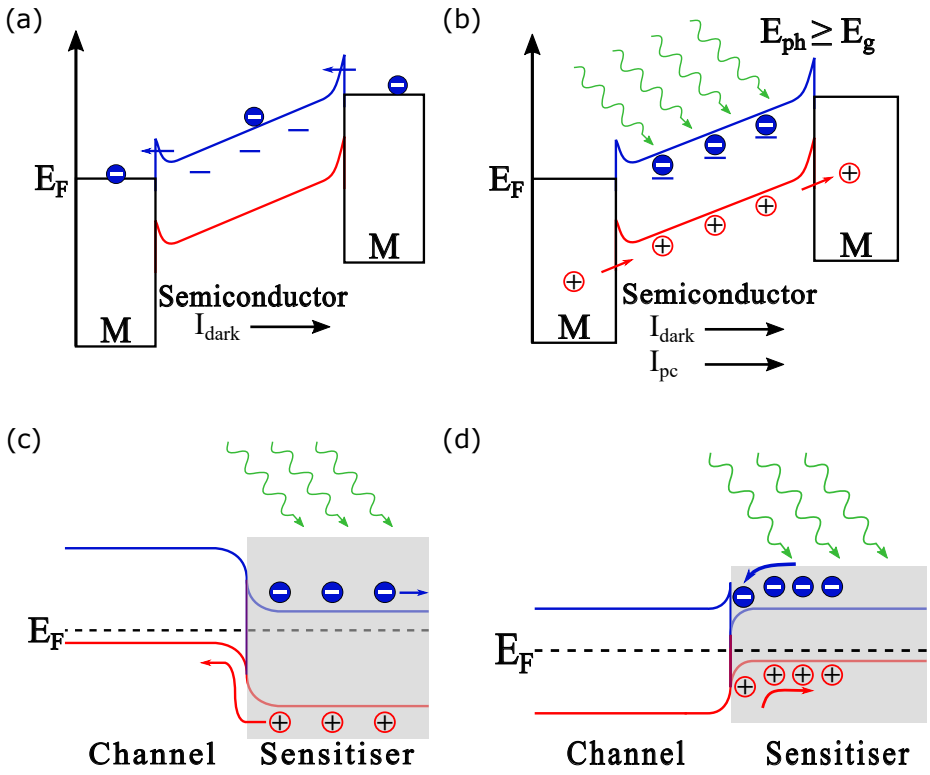

Figure 1.9: Photogating effect. (a),(b) Schematic of trap-induced Photogating (PG) effect in dark (panel a) and under illumination (panel b). (c) Schematic of Photogating (PG) effect due to the injection of photoexcited carriers from the sensitiser to the channel. (d) Schematic of Photogating (PG) effect due to the accumulation of photoexcited carriers on the interface between the sensitiser and the channel. Panels (a),(b) are reproduced from M. Buscema et al.[76] with permission from the Royal Society of Chemistry.

togating (PG) effect[91]. Here, after the electron-hole pair is created due to the exposure of the device to light, one of the carriers is either transferred to a different material in contact with the semiconducting channel (e.g. a semiconducting 2D material, quantum dot), or captured by trap states (e.g. defect states inside or on the semiconducting channel, but also adsorbed atoms and molecules as well)[87,92]. These captured carriers create strong electric fields, thus acting as a local floating gate, strongly modulating the conductance of the channel and its electrical conductivity[72].

Figure 1.9 summarises the possible microscopic scenarios leading to the PG effect. In the first case depicted in the first two panels of Figure (1.9), photogenerated electrons

are trapped into electron trap states that exist in the material, leading to hole doping of the channel and high values of I_{pc} which is added to the dark current. As a result, the transfer curve ($I_{sd} - V_{bg}$) shifts in a positive direction.

The second case where the generation of excitons takes place in a different material (sensitiser) can be seen in Figure 1.9 (c)-(d). There are 2 subcategories in this case regarding the way that carrier density in the channel is increased. Firstly, as shown in Figure 1.9 (c), after the creation of the electron-hole pairs in the sensitiser, one of the two carrier types (in this case the electrons) flows in the sensitiser which now acts as a gate (for this reason it is also called *gating material*) while the other is injected to the channel material. On the contrary, Figure 1.9 (d) shows a different case. Here, the photoexcited carriers are generated inside the sensitiser, but due to the barrier that has been formed on the interface of the two materials, no carriers are ejected to the channel. However, they accumulate on the interface between the two materials. In this particular case, electrons are accumulated on the interface, while holes flow in the sensitiser. As expected, the plethora of opposite charged carriers give rise to the photocurrent.

Photogating effect can lead to high gain (G), according to the relationship $G \sim \tau_{trap}/\tau_{transit}$, where τ_{trap} is the trapped carrier lifetime and $\tau_{transit}$ the free carrier transit time. The gain mechanism in the PG phenomenon can be described as follows; the photogenerated majority carriers (in this example, electrons) need time $\tau_{transit}$ to drift through the channel. If the time the photogenerated minority carriers remain trapped is larger, $\tau_{trap} > \tau_{transit}$, then more carriers are collected at the drain electrode before the trapped carrier recombines. However, this greatly affects the high-frequency response of the photodetector, as the large recombination times make the trapped carriers induce more majority carriers for some time after illumination stops.

BIBLIOGRAPHY

[1] Th. Henning and F. Salama. Carbon in the universe. *Science*, 282(5397):2204–2210, dec 1998.

[2] M. Asplund, N. Grevesse, A. J. Sauval, and P. Scott. The chemical composition of the sun. *Annual Review of Astronomy and Astrophysics*, 47(1):481–522, sep 2009.

[3] J. R. Rumble. *CRC Handbook of Chemistry and Physics*. Taylor & Francis Ltd, July 2022.

[4] A. M. Mannion. *Carbon and Its Domestication*. Springer Netherlands, January 2006.

[5] S. Randich and L. Magrini. Light elements in the universe. *Frontiers in Astronomy and Space Sciences*, 8, mar 2021.

[6] H. Oberhummer, A. Csoto, and H. Schlattl. Stellar production rates of carbon and its abundance in the universe. *Science*, 289(5476):88–90, jul 2000.

[7] A. Earnshaw N. N. Greenwood. *Chemistry of the Elements*. Elsevier Science & Techn., December 2012.

[8] K. S. Novoselov. Electric field effect in atomically thin carbon films. *Science*, 306(5696):666–669, oct 2004.

[9] P. R. Wallace. The band theory of graphite. *Physical Review*, 71(9):622–634, may 1947.

[10] A. H. Castro Neto, F. Guinea, N. M. R. Peres, K. S. Novoselov, and A. K. Geim. The electronic properties of graphene. *Reviews of Modern Physics*, 81(1):109–162, jan 2009.

[11] F. Bloch. Über die quantenmechanik der elektronen in kristallgittern. *Zeitschrift für Physik*, 52(7-8):555–600, jul 1929.

[12] W. G. Cullen, M. Yamamoto, K. M. Burson, J. H. Chen, C. Jang, L. Li, M. S. Fuhrer, and E. D. Williams. High-fidelity conformation of graphene to SiO_2 topographic features. *Physical Review Letters*, 105(21), nov 2010.

[13] M. Titov, P. M. Ostrovsky, I. V. Gornyi, A. Schuessler, and A. D. Mirlin. Charge transport in graphene with resonant scatterers. *Physical Review Letters*, 104(7), feb 2010.

[14] J. Robertson. High dielectric constant oxides. *The European Physical Journal Applied Physics*, 28(3):265–291, dec 2004.

[15] K. S. Novoselov, A. K. Geim, S. V. Morozov, D. Jiang, M. I. Katsnelson, I. V. Grigorieva, S. V. Dubonos, and A. A. Firsov. Two-dimensional gas of massless dirac fermions in graphene. *Nature*, 438(7065):197–200, nov 2005.

[16] S. V. Morozov, K. S. Novoselov, M. I. Katsnelson, F. Schedin, D. C. Elias, J. A. Jaszczak, and A. K. Geim. Giant intrinsic carrier mobilities in graphene and its bilayer. *Physical Review Letters*, 100(1), jan 2008.

[17] L. Banszerus, M. Schmitz, S. Engels, J. Dauber, M. Oellers, F. Haupt, K. Watanabe, T. Taniguchi, B. Beschoten, and C. Stampfer. Ultrahigh-mobility graphene devices from chemical vapor deposition on reusable copper. *Science Advances*, 1(6):e1500222, jul 2015.

[18] A. S. Mayorov, R. V. Gorbachev, S. V. Morozov, L. Britnell, R. Jalil, L. A. Ponomarenko, P. Blake, K. S. Novoselov, K. Watanabe, T. Taniguchi, and A. K. Geim. Micrometer-scale ballistic transport in encapsulated graphene at room temperature. *Nano Letters*, 11(6):2396–2399, jun 2011.

[19] E. V. Castro, H. Ochoa, M. I. Katsnelson, R. V. Gorbachev, D. C. Elias, K. S. Novoselov, A. K. Geim, and F. Guinea. Limits on charge carrier mobility in suspended graphene due to flexural phonons. *Physical Review Letters*, 105(26), dec 2010.

[20] J. C. Slonczewski and P. R. Weiss. Band structure of graphite. *Physical Review*, 109(2):272–279, jan 1958.

[21] F. Wang, Y. Zhang, C. Tian, C. Girit, A. Zettl, M. Crommie, and Y. R. Shen. Gate-variable optical transitions in graphene. *Science*, 320(5873):206–209, mar 2008.

[22] Z. Q. Li, E. A. Henriksen, Z. Jiang, Z. Hao, M. C. Martin, P. Kim, H. L. Stormer, and D. N. Basov. Dirac charge dynamics in graphene by infrared spectroscopy. *Nature Physics*, 4(7):532–535, jun 2008.

[23] J. Horng, C. F. Chen, B. Geng, C. Girit, Y. Zhang, Z. Hao, H. A. Bechtel, M. Martin, A. Zettl, M. F. Crommie, Y. R. Shen, and F. Wang. Drude conductivity of dirac fermions in graphene. *Physical Review B*, 83(16):165113, apr 2011.

[24] L. Ju, B. Geng, J. Horng, C. Girit, M. Martin, Z. Hao, H. A. Bechtel, X. Liang, A. Zettl, Y. R. Shen, and F. Wang. Graphene plasmonics for tunable terahertz metamaterials. *Nature Nanotechnology*, 6(10):630–634, sep 2011.

[25] H. Yan, X. Li, B. Chandra, G. Tulevski, Y. Wu, M. Freitag, W. Zhu, P. Avouris, and F. Xia. Tunable infrared plasmonic devices using graphene/insulator stacks. *Nature Nanotechnology*, 7(5):330–334, apr 2012.

[26] K. F. Mak, M. Y. Sfeir, J. A. Misewich, and T. F. Heinz. The evolution of electronic structure in few-layer graphene revealed by optical spectroscopy. *Proceedings of the National Academy of Sciences*, 107(34):14999–15004, aug 2010.

[27] K. F. Mak, L. Ju, F. Wang, and T. F. Heinz. Optical spectroscopy of graphene: From the far infrared to the ultraviolet. *Solid State Communications*, 152(15):1341–1349, aug 2012.

[28] T. Stauber, N. M. R. Peres, and A. K. Geim. Optical conductivity of graphene in the visible region of the spectrum. *Physical Review B*, 78(8), aug 2008.

[29] N. M. R. Peres. Colloquium: The transport properties of graphene: An introduction. *Reviews of Modern Physics*, 82(3):2673–2700, sep 2010.

[30] K. F. Mak, J. Shan, and T. F. Heinz. Electronic structure of few-layer graphene: Experimental demonstration of strong dependence on stacking sequence. *Physical Review Letters*, 104(17), apr 2010.

[31] R. R. Nair, P. Blake, A. N. Grigorenko, K. S. Novoselov, T. J. Booth, T. Stauber, N. M. R. Peres, and A. K. Geim. Fine structure constant defines visual transparency of graphene. *Science*, 320(5881):1308–1308, jun 2008.

[32] K. F. Mak, M. Y. Sfeir, Y. Wu, C. H. Lui, J. A. Misewich, and T. F. Heinz. Measurement of the optical conductivity of graphene. *Physical Review Letters*, 101(19), nov 2008.

[33] M. Chhowalla, H. S. Shin, G. Eda, L. J. Li, K. P. Loh, and H. Zhang. The chemistry of two-dimensional layered transition metal dichalcogenide nanosheets. *Nature Chemistry*, 5(4):263–275, mar 2013.

[34] F. Xia, H. Wang, D. Xiao, M. Dubey, and A. Ramasubramaniam. Two-dimensional material nanophotonics. *Nature Photonics*, 8(12):899–907, nov 2014.

[35] Q. H. Wang, K. Kalantar-Zadeh, A. Kis, J. N. Coleman, and M. S. Strano. Electronics and optoelectronics of two-dimensional transition metal dichalcogenides. *Nature Nanotechnology*, 7(11):699–712, nov 2012.

[36] D. Jariwala, V. K. Sangwan, L. J. Lauhon, Tobin J. Marks, and M. C. Hersam. Emerging device applications for semiconducting two-dimensional transition metal dichalcogenides. *ACS Nano*, 8(2):1102–1120, jan 2014.

[37] K. F. Mak, C. Lee, J. Hone, J. Shan, and T. F. Heinz. Atomically thin MoS_2: A new direct-gap semiconductor. *Physical Review Letters*, 105(13), sep 2010.

[38] W. Zhao, R. M. Ribeiro, M. Toh, A. Carvalho, C. Kloc, A. H. Castro Neto, and G. Eda. Origin of indirect optical transitions in few-layer MoS_2, WS_2, and WSe_2. *Nano Letters*, 13(11):5627–5634, nov 2013.

[39] Y. Zhang, T. R. Chang, B. Zhou, Y. T. Cui, H. Yan, Z. Liu, F. Schmitt, J. Lee, R. Moore, Y. Chen, H. Lin, H. T. Jeng, S. K. Mo, Z. Hussain, A. Bansil, and Z. X. Shen. Direct observation of the transition from indirect to direct bandgap in atomically thin epitaxial $MoSe_2$. *Nature Nanotechnology*, 9(2):111–115, dec 2013.

[40] G. Wang, X. Marie, L. Bouet, M. Vidal, A. Balocchi, T. Amand, D. Lagarde, and B. Urbaszek. Exciton dynamics in WSe_2 bilayers. *Applied Physics Letters*, 105(18):182105, nov 2014.

[41] E. Cappelluti, R. Roldán, J. A. Silva-Guillén, P. Ordejón, and F. Guinea. Tight-binding model and direct-gap/indirect-gap transition in single-layer and multilayer MoS_2. *Physical Review B*, 88(7), aug 2013.

[42] A. Castellanos-Gomez, E. Cappelluti, R. Roldán, N. Agraït, F. Guinea, and G.o Rubio-Bollinger. Electric-field screening in atomically thin layers of MoS_2: the role of interlayer coupling. *Advanced Materials*, 25(6):899–903, nov 2012.

[43] Z. Y. Zhu, Y. C. Cheng, and U. Schwingenschlögl. Giant spin-orbit-induced spin splitting in two-dimensional transition-metal dichalcogenide semiconductors. *Physical Review B*, 84(15), oct 2011.

[44] D. Xiao, G. B. Liu, W. Feng, X. Xu, and W. Yao. Coupled spin and valley physics in monolayers of mos_2 and other group-VI dichalcogenides. *Physical Review Letters*, 108(19), may 2012.

[45] H. Zeng, J. Dai, W. Yao, D. Xiao, and X. Cui. Valley polarization in MoS_2 monolayers by optical pumping. *Nature Nanotechnology*, 7(8):490–493, jun 2012.

[46] T. Cao, G. Wang, W. Han, H. Ye, C. Zhu, J. Shi, Q. Niu, P. Tan, E. Wang, B. Liu, and J. Feng. Valley-selective circular dichroism of monolayer molybdenum disulphide. *Nature Communications*, 3(1), jan 2012.

[47] S. Wu, J. S. Ross, G. B. Liu, G. Aivazian, A. Jones, Z. Fei, W. Zhu, D. Xiao, W. Yao, D. Cobden, and X. Xu. Electrical tuning of valley magnetic moment through symmetry control in bilayer MoS_2. *Nature Physics*, 9(3):149–153, jan 2013.

[48] H. Ochoa and R. Roldán. Spin-orbit-mediated spin relaxation in monolayer MoS_2. *Physical Review B*, 87(24), jun 2013.

[49] R. Roldán, A. Castellanos-Gomez, E. Cappelluti, and F. Guinea. Strain engineering in semiconducting two-dimensional crystals. *Journal of Physics: Condensed Matter*, 27(31):313201, jul 2015.

[50] W. Wu, L. Wang, Y. Li, F. Zhang, L. Lin, S. Niu, D. Chenet, X. Zhang, Y. Hao, T. F. Heinz, J. Hone, and Z. L. Wang. Piezoelectricity of single-atomic-layer mos_2 for energy conversion and piezotronics. *Nature*, 514(7523):470–474, oct 2014.

[51] J. Feng, X. Qian, C. W. Huang, and J. Li. Strain-engineered artificial atom as a broad-spectrum solar energy funnel. *Nature Photonics*, 6(12):866–872, nov 2012.

[52] A. Ambrosi, Z. Sofer, and M. Pumera. 2h $\rightarrow$ 1t phase transition and hydrogen evolution activity of MoS_2, $MoSe_2$, WS_2 and WSe_2 strongly depends on the MX_2 composition. *Chemical Communications*, 51(40):8450–8453, 2015.

[53] R. Kappera, D. Voiry, S. E. Yalcin, B. Branch, G. Gupta, A. D. Mohite, and M. Chhowalla. Phase-engineered low-resistance contacts for ultrathin MoS_2 transistors. *Nature Materials*, 13(12):1128–1134, aug 2014.

[54] T. Cheiwchanchamnangij and W. R. L. Lambrecht. Quasiparticle band structure calculation of monolayer, bilayer, and bulk MoS_2. *Physical Review B*, 85(20), may 2012.

[55] S. Lebègue and O. Eriksson. Electronic structure of two-dimensional crystals from ab initio theory. *Physical Review B*, 79(11), mar 2009.

[56] T. Li and G. Galli. Electronic properties of MoS_2 nanoparticles. *The Journal of Physical Chemistry C*, 111(44):16192–16196, nov 2007.

[57] D. Xiao, W. Yao, and Q. Niu. Valley-contrasting physics in graphene: Magnetic moment and topological transport. *Physical Review Letters*, 99(23), dec 2007.

[58] K. F. Mak, K. He, J. Shan, and T. F. Heinz. Control of valley polarization in monolayer MoS_2 by optical helicity. *Nature Nanotechnology*, 7(8):494–498, jun 2012.

[59] K. F. Mak and J. Shan. Photonics and optoelectronics of 2d semiconductor transition metal dichalcogenides. *Nature Photonics*, 10(4):216–226, mar 2016.

[60] A. Splendiani, L. Sun, Y. Zhang, T. Li, J. Kim, C. Y. Chim, G. Galli, and F. Wang. Emerging photoluminescence in monolayer MoS_2. *Nano Letters*, 10(4):1271–1275, apr 2010.

[61] T. C. Berkelbach, M. S. Hybertsen, and D. R. Reichman. Theory of neutral and charged excitons in monolayer transition metal dichalcogenides. *Physical Review B*, 88(4), jul 2013.

[62] . Ramasubramaniam. Large excitonic effects in monolayers of molybdenum and tungsten dichalcogenides. *Physical Review B*, 86(11), sep 2012.

[63] A. Chernikov, T. C. Berkelbach, H. M. Hill, A. Rigosi, Y. Li, O. B. Aslan, D. R. Reichman, M. S. Hybertsen, and T. F. Heinz. Exciton binding energy and nonhydrogenic rydberg series in monolayer ws_2. *Physical Review Letters*, 113(7), aug 2014.

[64] K. He, N. Kumar, L. Zhao, Z. Wang, K. F. Mak, H. Zhao, and J. Shan. Tightly bound excitons in monolayer wse_2. *Physical Review Letters*, 113(2):026803, jul 2014.

[65] G. Wang, X. Marie, I. Gerber, T. Amand, D. Lagarde, L. Bouet, M. Vidal, A. Balocchi, and B. Urbaszek. Giant enhancement of the optical second-harmonic emission of wse_2 monolayers by laser excitation at exciton resonances. *Physical Review Letters*, 114(9), mar 2015.

[66] A. V. Stier, K. M. McCreary, B. T. Jonker, J. Kono, and S. A. Crooker. Exciton diamagnetic shifts and valley zeeman effects in monolayer WS_2 and MoS_2 to 65 tesla. *Nature Communications*, 7(1), feb 2016.

[67] A. V. Stier, N. P. Wilson, K. A. Velizhanin, J. Kono, X. Xu, and S. A. Crooker. Magnetooptics of exciton rydberg states in a monolayer semiconductor. *Physical Review Letters*, 120(5), feb 2018.

[68] K. F. Mak, K. He, C. Lee, G. H. Lee, J. Hone, T. F. Heinz, and J. Shan. Tightly bound trions in monolayer mos_2. *Nature Materials*, 12(3):207–211, dec 2012.

[69] J. S. Ross, S. Wu, H. Yu, N. J. Ghimire, A. M. Jones, G. Aivazian, J. Yan, D. G. Mandrus, D. Xiao, W. Yao, and X. Xu. Electrical control of neutral and charged excitons in a monolayer semiconductor. *Nature Communications*, 4(1), feb 2013.

[70] J. Shang, X. Shen, C. Cong, N. Peimyoo, B. Cao, M. Eginligil, and T. Yu. Observation of excitonic fine structure in a 2d transition-metal dichalcogenide semiconductor. *ACS Nano*, 9(1):647–655, jan 2015.

[71] Y. You, X. X. Zhang, T. C. Berkelbach, M. S. Hybertsen, D. R. Reichman, and T. F. Heinz. Observation of biexcitons in monolayer wse_2. *Nature Physics*, 11(6):477–481, may 2015.

[72] C. Yang, G. Wang, M. Liu, F. Yao, and H. Li. Mechanism, material, design, and implementation principle of two-dimensional material photodetectors. *Nanomaterials*, 11(10):2688, oct 2021.

[73] B. Streetman. *Solid state electronic devices*. Pearson, Boston, 2016.

[74] F. H. L. Koppens, T. Mueller, Ph. Avouris, A. C. Ferrari, M. S. Vitiello, and M. Polini. Photodetectors based on graphene, other two-dimensional materials and hybrid systems. *Nature Nanotechnology*, 9(10):780–793, oct 2014.

[75] A. De Sanctis, J. Mehew, M. Craciun, and S. Russo. Graphene-based light sensing: Fabrication, characterisation, physical properties and performance. *Materials*, 11(9):1762, sep 2018.

[76] M. Buscema, J. O. Island, D. J. Groenendijk, S. I. Blanter, G. A. Steele, H. S. J. van der Zant, and A. Castellanos-Gomez. Photocurrent generation with two-dimensional van der waals semiconductors. *Chemical Society Reviews*, 44(11):3691–3718, 2015.

[77] A. Pospischil, M. M. Furchi, and T. Mueller. Solar-energy conversion and light emission in an atomic monolayer p–n diode. *Nature Nanotechnology*, 9(4):257–261, mar 2014.

[78] B. W. H. Baugher, H. O. H. Churchill, Y. Yang, and P. Jarillo-Herrero. Optoelectronic devices based on electrically tunable p–n diodes in a monolayer dichalcogenide. *Nature Nanotechnology*, 9(4):262–267, mar 2014.

[79] M. M. Furchi, A. Pospischil, F. Libisch, J. Burgdörfer, and T. Mueller. Photovoltaic effect in an electrically tunable van der waals heterojunction. *Nano Letters*, 14(8):4785–4791, jul 2014.

[80] C. H. Lee, G. H. Lee, A. M. van der Zande, W. Chen, Y. Li, M. Han, X. Cui, G. Arefe, C. Nuckolls, T. F. Heinz, J. Guo, J. Hone, and P. Kim. Atomically thin p–n junctions with van der waals heterointerfaces. *Nature Nanotechnology*, 9(9):676–681, aug 2014.

[81] M. C. Lemme, F. H. L. Koppens, A. L. Falk, M. S. Rudner, H. Park, L. S. Levitov, and C. M. Marcus. Gate-activated photoresponse in a graphene p–n junction. *Nano Letters*, 11(10):4134–4137, sep 2011.

[82] N. M. Gabor, J. C. W. Song, Q. Ma, N. L. Nair, T. Taychatanapat, K. Watanabe, T. Taniguchi, L. S. Levitov, and P. Jarillo-Herrero. Hot carrier–assisted intrinsic photoresponse in graphene. *Science*, 334(6056):648–652, nov 2011.

[83] C. C. Wu, D. Jariwala, V. K. Sangwan, T. J. Marks, M. C. Hersam, and L. J. Lauhon. Elucidating the photoresponse of ultrathin MoS_2 field-effect transistors by scanning photocurrent microscopy. *The Journal of Physical Chemistry Letters*, 4(15):2508–2513, jul 2013.

[84] M. Fontana, T. Deppe, A. K. Boyd, M. Rinzan, A. Y. Liu, M. Paranjape, and P. Barbara. Electron-hole transport and photovoltaic effect in gated mos_2 schottky junctions. *Scientific Reports*, 3(1), apr 2013.

[85] M. Buscema, M. Barkelid, V. Zwiller, H. S. J. van der Zant, G. A. Steele, and A. Castellanos-Gomez. Large and tunable photothermoelectric effect in single-layer MoS_2. *Nano Letters*, 13(2):358–363, jan 2013.

[86] X. Xu, N. M. Gabor, J. S. Alden, A. M. van der Zande, and P. L. McEuen. Photo-thermoelectric effect at a graphene interface junction. *Nano Letters*, 10(2):562–566, nov 2009.

[87] P. Avouris. *2D Materials: Properties and Devices*. Cambridge University Press, July 2017.

[88] M. Cutler and N. F. Mott. Observation of anderson localization in an electron gas. *Physical Review*, 181(3):1336–1340, may 1969.

[89] E. H. Hwang, E. Rossi, and S. Das Sarma. Theory of thermopower in two-dimensional graphene. *Physical Review B*, 80(23):235415, dec 2009.

[90] X. Lu, L. Sun, P. Jiang, and X. Bao. Progress of photodetectors based on the photothermoelectric effect. *Advanced Materials*, 31(50):1902044, sep 2019.

[91] X. Yu, Y. Li, X. Hu, D. Zhang, Y. Tao, Z. Liu, Y. He, M. A. Haque, Z. Liu, T. Wu, and Q. J. Wang. Narrow bandgap oxide nanoparticles coupled with graphene for high performance mid-infrared photodetection. *Nature Communications*, 9(1), oct 2018.

[92] H. Fang and W. Hu. Photogating in low dimensional photodetectors. *Advanced Science*, 4(12):1700323, oct 2017.

2

EXPERIMENTAL METHODS

INTRODUCTION

The isolation and experimental characterisation of graphene in 2004 sparked the interest of the global scientific community and paved the way for a plethora of other two-dimensional materials. Handling and investigating the properties of these materials needs the application of specific techniques that sometimes are different from the corresponding ones being used in bulk semiconductors.

In this chapter, the main optoelectronic characterisation techniques will be presented. First, Raman spectroscopy which is an important technique to identify the material and its structural properties will be thoroughly discussed, followed by a presentation of the experimental apparatus. Raman spectroscopy is a valuable tool in condensed matter physics, as a detailed examination of the Raman spectrum gives an insight on structural properties and formation of a material. In general, Raman spectroscopy was used constantly throughout the research included in this thesis, but mainly to give an insight on the quality of the crystal used for the device fabrication. As a result, only a single Raman spectrum is presented in Chapter 5, where we use the spectrum to extract useful information that are crucial to the following experiments.

All the setups that are being described in the second section are exclusively used for the optoelectronic characterisation of the samples. Designed and built by our group, these characterisation apparatus allow for complete and in-situ optoelectronic characterisation of a wide range of nanodevices, without the need to transfer them between different setups. This keeps the contamination level to a minimum, enhances the characteristics of the devices and extends their lifetime.

This will lead to the main part of the optoelectronic characterisation where the techniques used for transport measurements, photoresponsivity and photoluminescence spectroscopy are presented. Additionally, the effect of the metallic contacts on a semiconducting channel and the characterisation of contact resistance will be thoroughly discussed as it plays a very important role on the behaviour of the semiconducting devices. Finally, a summary of the basics of the Hall effect that we used for the research presented in Chapter 5 and a description of the setup conclude this chapter.

2.1 RAMAN SPECTROSCOPY

Raman spectroscopy is a non-invasive, optical technique used to characterise the properties of a material. In principle, the Raman effect is associated with the inelastic scattering of photons by the lattice vibrational modes (phonons) in a solid. Semiclassically, the covalent bonds between atoms in a molecule can be described by a spring with spring constant k. Such a description helps to illustrate the vibrations of the atoms in a molecule. Raman spectroscopy probes the spring constant of the atomic bonds resulting in a characteristic spectrum for each material and substance, thus it is widely used for chemical identification of unknown samples[1,2].

In the case of graphene and TMDs, the spring constant that describes the bonds between the atoms is highly sensitive to numerous physical parameters. Thus, careful analysis of a sample's Raman spectrum allows the determination of the number of layers[3,4], the degree of doping[1,5], disorder[6], defects[7,8] and strain[6,9,10].

For crystalline solids, the scattering takes place between an electron-hole pair and an elemental vibration (phonon) of the material. A photon impinging on the material will excite an electron from the valence band to either a virtual empty state within the bandgap or a real state in the conduction band. In the case where the excited state is a real state, the effect is referred as *resonant Raman scattering (RRS)*.

This will create an electron-hole pair, which subsequently will scatter inelastically with a phonon of the material of energy $\hbar\Omega$. Depending on whether the phonon was absorbed or emitted during the scattering, the photon resulting after the relaxation of the electron-hole pair will have frequency shift (Raman shift) of

$$\Delta\omega = \omega_i \pm \Omega\,, \tag{2.1}$$

where ω_i is the excitation frequency ($\hbar\omega_i$ is the excitation energy). The minus sign corresponds to the absorption of a phonon (Stokes process), while the plus to the emission of a phonon (anti-Stokes process).

The Raman shift between the initial and the excited state is typically reported in wavenumbers

$$\Delta k = \left(\frac{1}{\lambda_i} - \frac{1}{\lambda_{exc}} \right) , \tag{2.2}$$

where λ_i and λ_{exc} are the wavelengths corresponding to the initial and excited states respectively. In addition, Raman shift is also reported in units of reciprocal centimeters (cm^{-1}), so Eq. (2.2) can be further modified to get the result with the wanted dimensions as follows

$$\Delta k \left[\mathrm{cm}^{-1}\right] = \left(\frac{1}{\lambda_i(\mathrm{nm})} - \frac{1}{\lambda_{exc}(\mathrm{nm})} \right) \frac{10^7[\mathrm{nm}]}{[\mathrm{cm}]} . \tag{2.3}$$

In the next two sub-sections, this shift will be approached by both a classical and a quantum point of view.

2.1.1 *Classical theory of Raman scattering*

In terms of classical theory, Raman scattering is described by the interaction of an incoming EM wave that excites a diatomic molecule. The electric field carried by the EM wave along its direction of propagation, $\hat{x_j}$, is described by the equation

$$\vec{E} = E_0 \cos\omega_0 t \, \hat{x}_i \, , \tag{2.4}$$

where $\hat{x_i} \cdot \hat{x_j} = \delta_{ij}$[1], E_0 is the amplitude and $\omega_0 = 2\pi\nu_0$ the frequency of the incoming EM wave. The light source commonly used in Raman spectroscopy is a laser. The laser light is used as it is a very intense beam of nearly monochromatic light that can interact with sample molecules.

When a diatomic molecule is irradiated by this light, an electric dipole moment will

[1] Here δ_{ij} is the Kronecker delta, for which takes only the values 0 and 1 as follows

$$\delta_{ij} = \begin{cases} 1, & i = j, \\ 0, & i \neq j. \end{cases}$$

be induced

$$P_i = \alpha_{ij} E_j \,, \tag{2.5}$$

where α_{ij} is the polarisability tensor of the molecule. Let the molecule vibrating with a frequency Ω_m, then the nuclear displacement q_i along a direction $\hat{x}_i$ is given by the expression

$$\vec{q} = q_0 \cos \Omega_m t \, \hat{x}_i \tag{2.6}$$

with q_0 being the vibrational amplitude. In general, the polarisability tensor α_{ij} is a function of q, so $\alpha_{ij} = \alpha(q)_{ij}$. Thus, for small vibrations the polarisability can be expanded to gain the following expression

$$\alpha_{ij} = (\alpha_{ij})_0 + \left(\frac{\partial \alpha_{ij}}{\partial q^k} \right)_0 q_0^k + \dots \,, \tag{2.7}$$

where index i implies that quantities are calculated at the equilibrium position and only 1st order approximation terms have been kept. Finally, by introducing Eq. (2.7) and (Eq. 2.6) to Eq. (2.5), the dipole moment of a diatomic molecule irradiated by light becomes

$$\begin{aligned} P_i = {} & (\alpha_{ij})_0 E_0 \cos \omega_0 t \, \hat{x}_j \\ & + \frac{1}{2} \left(\frac{\partial \alpha_{ij}}{\partial q^k} \right)_0 q_0 E_0 \cos \left((\omega_0 - \Omega_m) t \right) \hat{x}_j \\ & + \frac{1}{2} \left(\frac{\partial \alpha_{ij}}{\partial q^k} \right)_0 q_0 E_0 \cos \left((\omega_0 + \Omega_m) t \right) \hat{x}_j \,. \end{aligned} \tag{2.8}$$

Thus, according to the classical theory of Raman scattering, Eq. (2.8) can be seen as a sum of three terms. The first describes an oscillating dipole radiating at frequency ω_0 (Rayleigh scattering) and the remaining two terms describe the inelastic (Raman) scattering at frequencies $\omega_0 - \Omega_m$ (Stokes) and $\omega_0 + \Omega_m$ (anti-Stokes). From the above expression, it can be seen that if the rate of change of polarisability with the vibration is equal to zero ($\partial \alpha_{ij} / \partial q^k = 0$), then the transition is not Raman active and the light is not scattered. Figure 2.1 summarises the Raman scattering processes within

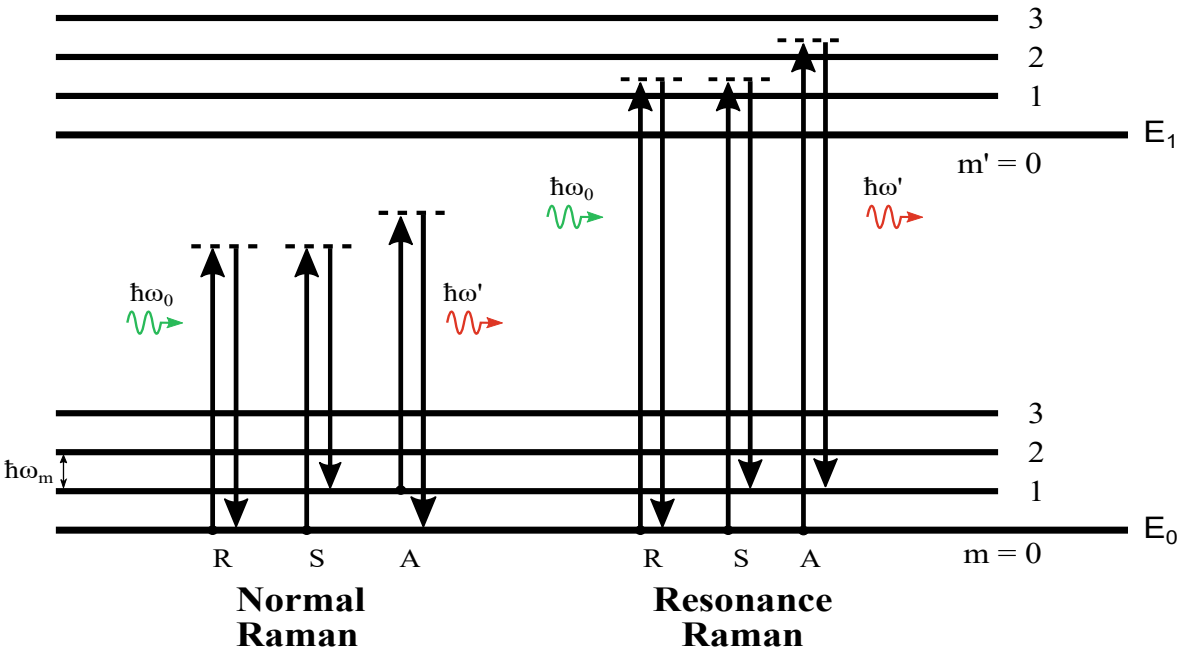

Figure 2.1: Raman scattering. Simplified Jablonski diagram for Normal and Resonance Raman transitions within a diatomic molecule. Rayleigh scattering is referred as transition "R", while the Stokes transition as "S" and the anti-Stokes as "A".

a diatomic molecule. In the case of Normal Raman spectroscopy, the energy of the excitation light ($\hbar\omega_0$) is chosen far below the first electronic excited state. As a result, the excited electrons are led to a "virtual state" (depicted here with a dotted line) to distinguish it from the real excited states.

In comparison, resonant Raman scattering (RRS) occurs when the excitation energy is chosen so that it intercepts the manifold of an electronic excited state. The excitation of continuous vibrational states found in solid, liquid and gaseous states, produces extremely strong enhancement of the Resonant Raman bands. Specifically, the intensities of Raman bands observed in this area (chromophore) are *selectively* enhanced by a factor of 10^3 to 10^5.[11]

2.1.2 *Quantum theory of Raman scattering*

Although the classical approach explains quite well the mechanisms behind the rise of Raman bands, in order to understand the phenomenon in its entirety it is necessary

to consider quantum mechanics[11–13]. Here, only a couple of important points of the quantum theory of Raman scattering will be presented as a complete approach falls out of the scope of this dissertation.

From a quantum physics point of view, Raman effect is described as an interaction of the wavefunction of the excited electron with the EM field of the incident light. The interaction of the wavefunction of the necleus with the EM field of the incident light can be treated separately due to the *Born-Oppenheimer approximation* (or adiabatic approximation). Due to the much larger mass of the atomic nuclei in comparison to that of the electrons, their motions can be separated, allowing the separate treatment of their corresponding wavefunctions. As a result, we can consider the wavefunction of a molecule as a product of a vibrational (nuclear) and an electronic wavefunction.

For the system of the excited molecule under the Born-Oppenheimer approximation, the total energy along with the crystal momentum must be conserved

$$\hbar\omega_i = \hbar\omega_s \pm \hbar\Omega\,, \tag{2.9}$$

$$\hbar\vec{k_i} = \hbar\vec{k_s} \pm \hbar\vec{q}\,, \tag{2.10}$$

where ω_i and $\vec{k_i}$ are the incident frequency and wavevector, while ω_s and $\vec{k_s}$ are the equivalent quantities of the scattered light and Ω and $\vec{q}$ are the frequency and wavevector of the phonons. Additionally, the "+" sign is true for a scattering process involving the creation of a phonon (anti-Stokes process), while the "−" sign corresponds to a scattering process where a phonon is annihilated (Stokes process).

A main point where the quantum theory of Raman scattering can shed light upon, is the different intensities between Stokes and anti-Stokes emissions. When the sample is at thermodynamic equilibrium, the upper state will be less populated than the ground state. As a result, the rate of transitions from the lower to the upper state (Stokes transitions) will be higher than in the opposite direction (anti-Stokes transitions). Correspondingly, the Stokes process is much more intense than the anti-Stokes, thus, normally, only the Stokes component is being measured. The ratio of the Stokes (S) to anti-Stokes (A) intensity depends on temperature, therefore it is used as a temperature probe according to the following equation[14,15]

$$\frac{I_S}{I_A} = C \exp\left(\frac{h\omega'_m}{k_B T}\right), \tag{2.11}$$

here, C is a parameter that depends both on the optical properties of the examined material, as well as on the optical elements of the system used.

2.1.3 *Raman spectrum of TMDs*

The crystal structure of transition metal dichalcogenides (TMD)s gives the Raman spectrum of these materials a certain degree of complexity, at least in comparison with graphene and graphite compounds. The variety of these materials in terms of lattice dynamics is almost unique, as there is a strong dependence from the number of atomic layers constituting the material of the symmetry, force constants and peak frequency[16].

Considering the unit cell of bulk MX_2, one can see that it includes 6 atoms of the X–M–X (X: chalcogen atom, M: metal atom) configuration, which implies the existence of 18 phonon (3 acoustic and 15 optical) modes. Due to the D_{6h} point group symmetry, the lattice vibrations at the Γ point can be expressed as[17]

$$\Gamma = A_{1g} + 2A_{2u} + 2B_{2g} + B_{1u} + E_{1g} + 2E_{1u} + 2E_{2g} + E_{2u}, \tag{2.12}$$

where one of the A_{2u}, E_{1u} are infra-red (IR) active while the remaining are acoustic modes, A_{1g}, E_{1g} and E_{2g} are *Raman active* and B_{2g}, B_{1u} and E_{2u} are optically inactive (silent).

However, the situation drastically changes when the thickness of the material is reduced to just a few atomic layers. In this case, due to the lack of translational symmetry along the z-axis, there is a reduction of symmetry in Few Layer (FL) TMDs[18]. Particularly, the point group symmetry of *odd number*-FL TMDs is reduced from D_{6h} to D_{3h} as a result of the existence of a reflection symmetry plane which coincides with the plane of metal atoms. Specifically for a monolayer (ML) TMD, the unit cell of which is composed of 3 atoms, the 9 normal vibrational modes at the Γ point are given by

$$\Gamma = 2A''_2 + A'_1 + 2E' + E'', \tag{2.13}$$

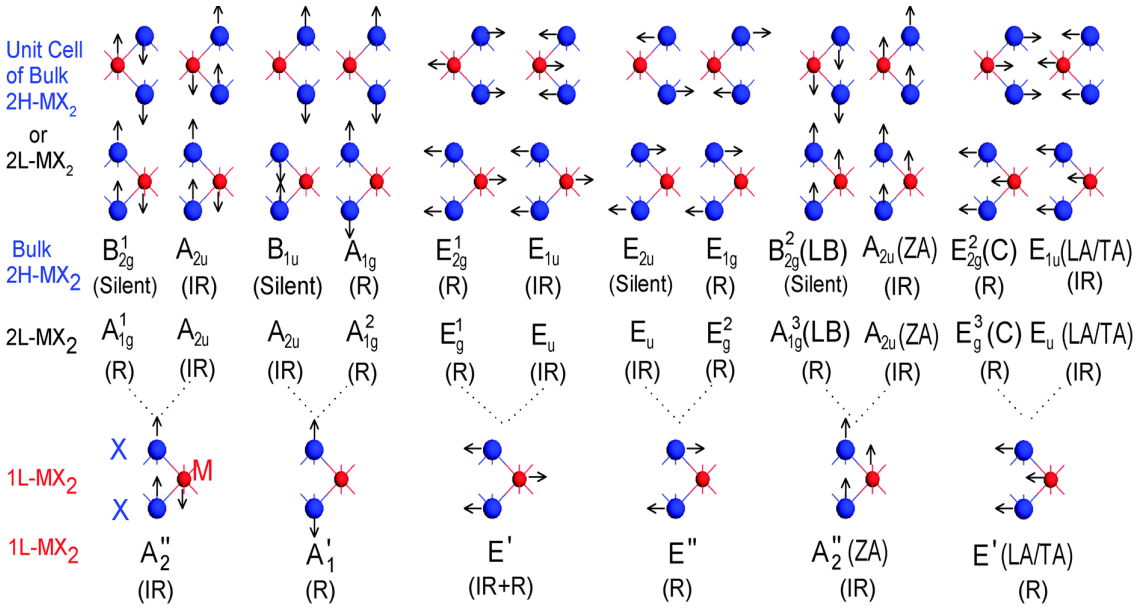

Figure 2.2: Optical vibration modes in bulk, 2-layer and monolayer 2H-MX_2. Summary of all optical phonons with identified Raman active (R), infra-red active (IR) and the corresponding inactive (silent) modes. Each optical vibration modes of a monolayer (1L) MX_2 with 2H polytype, splits into two modes in the case of bilayer (2L) and bulk material (dotted line), where one vibrates in-phase and the other out-of-phase. LA, LB (layer breathing), TA, ZA and C are different phonon modes. Reproduced with permission [16].

where A_1' and E'' are Raman active modes, one of A_2'' and E' are IR active and the rest are acoustic modes. All the optical vibration modes for bulk, bilayer and monolayer 2H-MX_2 TMDs are summarised in Figure 2.2, along with the symmetry and normal mode displacement in each case. Starting from the case of a monolayer MX_2 of 2H polytype and going to bulk material, each of the nine vibrational modes (here presented only 6, as it includes only the optical phonons) is split into two modes for a bilayer 2H-MX_2 (dotted line). In these "derivative" modes, the displacement between the top and bottom layer is in phase in one case and out of phase in the other.

At this point, the reader interested to dive into the details of the quantum description of Raman scattering is redirected to the detailed review article of Zhang et al. [16] where the physics of the phenomenon in TMDs, from bulk to monolayer, is studied in

detail.

2.2 OPTOELECTRONIC CHARACTERISATION

The following sections present a detailed overview of the bespoke experimental setups developed for the characterization of the opto-electronic properties of 2D materials with controlled atmosphere, illumination with a range of light sources (incoherent monochromatic, continuous and pulsed laser light), for a range of electrical frequencies up to 2 GHz.

2.2.1 *Experimental Setups*

To properly characterise semiconducting devices like those presented in this thesis, a combination of many different techniques was implemented. For the complete characterisation of the devices mentioned here, two custom-made experimental setups were used. These units were built and configured for minimising the exposure of the devices to contamination while maximising the different characterisation abilities.

2.2.1.1 *Multi-purpose microscope setup*

The first experimental setup is developed around an upright optical microscope (*Olympus* BX51) and it carries all the necessary components for performing different kind of optical and electrical measurements without the need of removing the sample from the holder, as shown in Figure 2.3. With this setup the user can perform low frequency electrical transport measurements, micro-Raman, photoluminescence (PL), absorption spectroscopy and mapping. Full automation of the system is achieved with a custom made LabVIEW-based software which is able to communicate to all electronic instruments via general purpose interface (GPIB)/universal serial bus (USB) and to modulate the lasers via digital-to-analog interface (DAC) (*National Instruments* NI-DAQ). The whole system is built on a vibration-isolated $120 \times 90\,\mathrm{cm}^2$ optical table.

Optical measurements are limited by the five different continuous wave lasers the machine bears, which cover an area from ultra-violet (UV) to red ($\lambda = 375, 473, 514, 561$ and $685\,\mathrm{nm}$), with powers ranging from 30 to 50 mW. The laser light delivery system is enclosed within a *ThorLabs* stackable tube lens system, allowing a light-tight con-

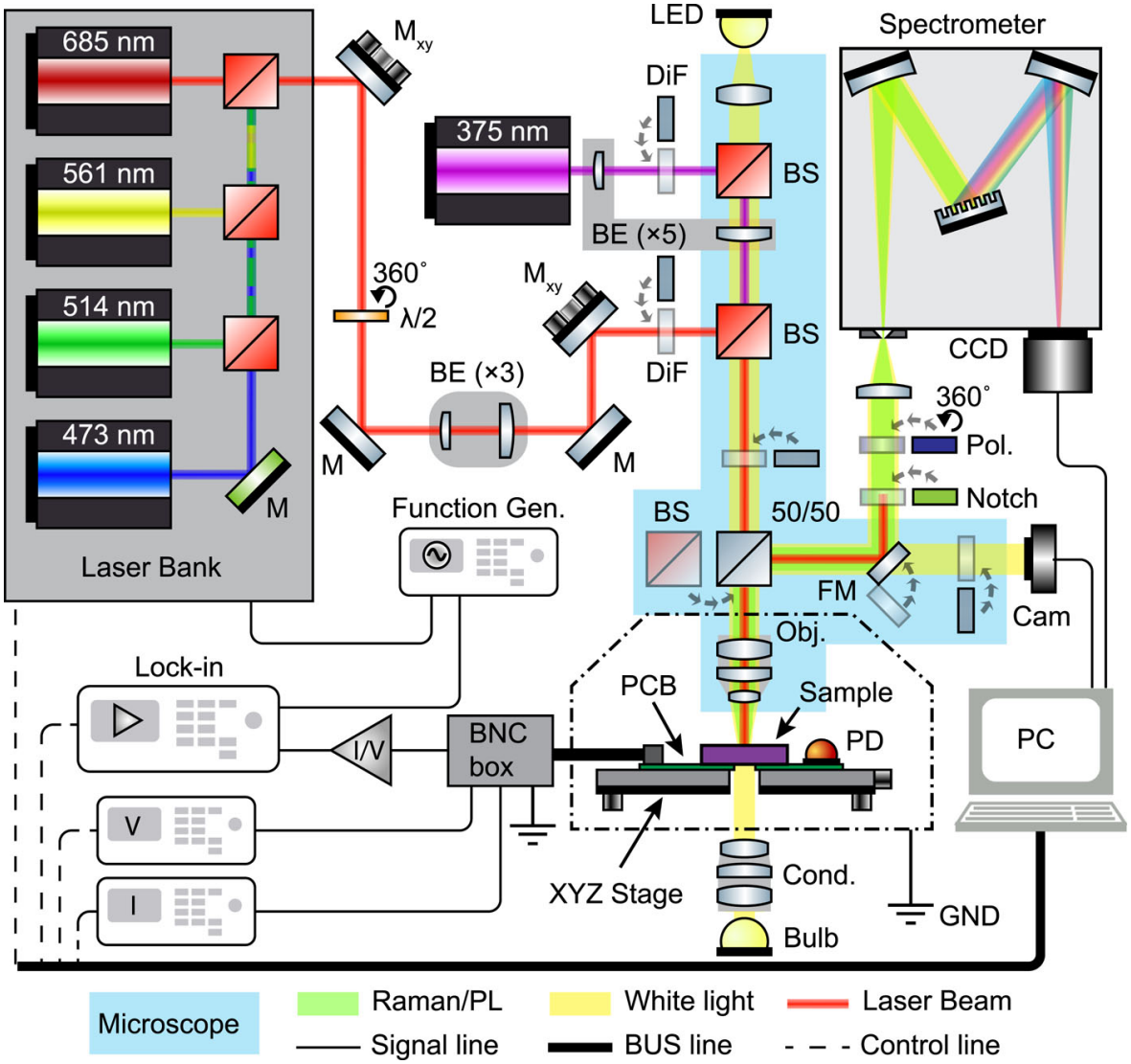

Figure 2.3: Schematic of the optoelectronic characterisation setup. The optical and electrical components of the multi-purspose microscope setup for the characterisation of 2D optoelectronic devices can be seen in detail here. Abbreviations: mirror (M), kinematic mirror (M_{xy}), half-wavelength plate ($\lambda/2$), beam expander (BE, followed by magnification), drop-in filter (DiF), beam splitter (BS, dichroic in red), Polariser/Analyser (Pol.), white light (WL), voltage (V) or current (I) sources/meters, flip mirror (FM), sample holder (PCB), photodetector (PD), condenser (Cond), microscope objective (Obj), imaging camera (Cam), spectroscopy camera (CCD), ground line (GND). Reused with permission [19].

nection. In addition, there is the possibility of changing the light polarisation by using a rotatable (360°) achromatic $\lambda/2$ plate. Also, it provides the user with the option to characterise the device in vacuum (or under a desired atmosphere), as it is equipped with a custom-made vacuum chamber. The main element for the analysis of the spectrum collected by the device is the mounted spectrometer (*Princeton Instruments* SP2500).

A high precision motorised *Prior Scientific OptiScan* ES111 with *ProScan III* controller enables the accurate control over the position of the illuminated region by a focused laser light, with a spatial accuracy of 200 nm. Focus control is also achieved through the same controller. The laser light propagates through the upright microscope column and is focused onto the sample by the chosen objective lens. Direct imaging of the sample and of the laser spot is possible by using a Charge-Coupled Device (CCD) in combination with an appropriate set of filters.

If the aim of the experiment is to measure the photocurrent produced in a device, then the generated carriers are extracted from the contacts of the device bonded to a Printed Circuit Board (PCB) and then connected though a shielded multi-core cable to a breakout Bayonet Neill–Concelman (BNC) box. This enables connections with different measuring instruments. Furthermore, there is the possibility to modulate the lasers by connecting them to a function generator, which locks them to a user-specified frequency, resembling the outcome of a mechanical chopper. The proper shielding from external electric field is achieved by using conductive fabric to enclose the microscope and then by grounding the whole measuring setup (including the optical table, the fabric and the walls of the BNC box).

In the case of a spectroscopic analysis of the device/material, the reflected light from the device is collected by the microscope's objective lens and with the use of a flip mirror (FM) is redirected to the spectrometer. The control of the spectrometer, CCD and the extraction of spectroscopic data is achieved with the use of native software (*Princeton Instruments* LightField).

2.2.1.2 *Photodetector characterisation setup*

The setup described in the above section gives only the option for narrow band excitation around five different wavelengths. Hence, the need for a different apparatus where

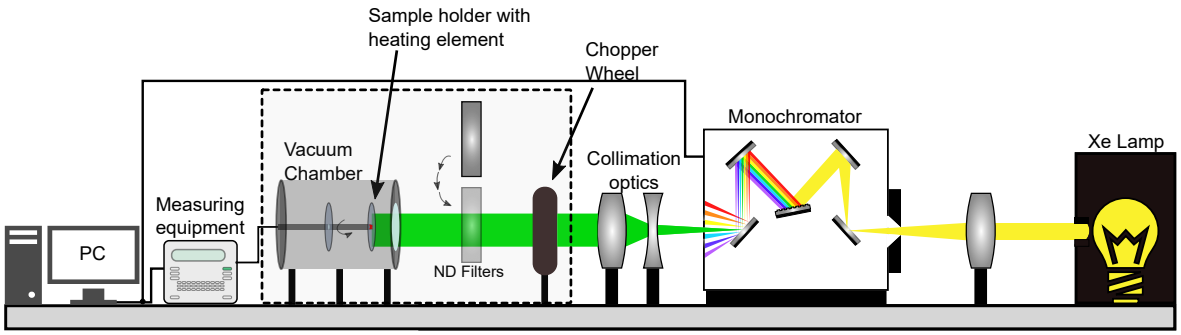

Figure 2.4: Schematic of the photodetector characterisation setup. The main optical and control elements of the setup are described here. The combination of the wide-spectrum Xenon lamp and the monochromator, offers the possibility of characterising the photoresponse of a device over a large spectral region (between 300 nm and 1150 nm). The sample along the neutral density filters and the chopper wheel is located within a light-tight enclosure to ensure minimum parasitic light detection.

the response of a device over a broad range of impinging light is possible arises. This need is covered by a second experimental setup which is mainly used to completely characterise a photodetecting device, presented in Figure 2.4.

The combination of a Xenon lamp (*Ushio* UXL 302-OX Xe 300W) which emits over a wide spectral range ($\sim$ 300 nm to 1100 nm), a monochromator (*Cornerstone* 130) and collimating optics (*Oriel* TLS-300X) results in a spectrally tunable incident light source, giving the user the ability to characterise the spectral response and the main figures of merit of a photodetector over that spectral range. For measuring a photosensitive device, the sample is loaded on a holder that bears a heating element for *in-situ* annealing and is then inserted in a custom-built vacuum chamber ($P_{min} \leq 10^{-6}$mbar). A chopper wheel and *neutral density* filters are used to attenuate and modulate the incident light, while a multi-pin feedthrough is used to extract the signal from the sample to the connected measuring equipment. The vacuum chamber along the aforementioned elements are located inside a light-tight enclosure for minimising the effects of parasitic light impinging on the device. Calibration data for the spectral measurements are acquired by use of a *ThorLabs* PM320E power meter equipped with a S130VC sensor, or by a *ThorLabs* FDS1010 photodiode connected to a *Stanford Reseasrch Systems* SR560 Low-Noise Preamplifier, depending on the needs of each

experiment.

2.2.2 *Transport Measurements*

A typical characterisation of an optoelectronic device begins with measuring its transport properties (see also Section 1.1.3). From this kind of measurements we can understand fundamental properties of the semiconductive channel, such as the resistivity of the material, the doping type, the carrier density, the contact resistance, *field effect mobility*, the ON/OFF ratio, the spectral photoresponse, etc.[20].

A complete initial characterisation of different 2D FETs can be seen in Figure 2.5. Initially, the transfer curves of the device under a source-drain bias are measured under dark conditions to determine the threshold voltage V_T, where the channel starts conducting (Figure 2.5 (b)). After that, we characterise the source-drain output of the device over a wide range of back gate biases (Figure 2.5 (c)), still without any exposure to light. This gives a complete characterisation of the device in dark conditions. The final step of the initial characterisation is to measure the photocurrent produced when the device is exposed to light. The spectral dependence of the photocurrent is determined using the monochromator, making it possible to identify the wavelength at which the largest photoresponse is measured. The photocurrent is calculated as

$$I_{ph} = I_{sd,illum} - I_{sd,dark}, \tag{2.14}$$

where $I_{sd,illum}$ is the current running between the source and the drain when the device is illuminated (with light of a specific wavelength) and $I_{sd,dark}$ is the dark current.

2.2.2.1 *Metal-Semiconductor Contact & Contact Resistance*

When a semiconductor comes in contact with a metal, an energy barrier is formed at the interface. This barrier controls the current conduction as well as its capacitance behaviour and has been widely studied since 1875 when F. Braun investigated rectifying metal-semiconductor systems[21]. A more in-depth analysis on this potential barrier was performed by Schottky in 1938[22], while the same year a more complete theoretical model of the metal-semiconductor contact was put forward. The potential barrier formed at the interface of a metal and a semiconductor in contact is called *Schottky barrier* and the theoretical model describing the ideal metal-semiconductor contact is

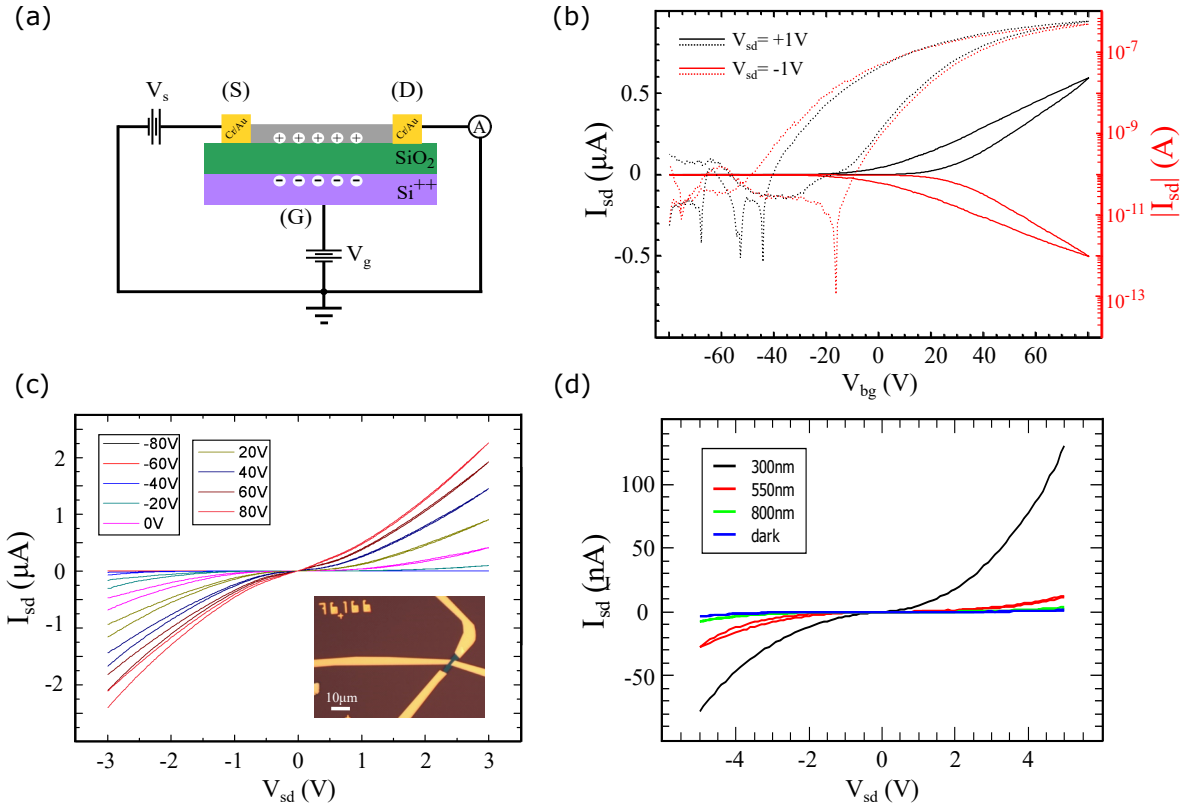

Figure 2.5: Drain characteristics of 2D FET devices. (a) Schematic of a simple 2D FET on a Si^{++}/SiO_2 substrate. (b) Transfer characteristics of the same $ReSe_2$ FET for different source-drain biases. The absolute value of the same data is also plotted in logarithmic scale where the behaviour of the transistor can be seen easier. The voltage is applied at the Source (S) terminal and the signal is measured from the Drain (D) terminal. The channel conductivity is controlled by the applied bias at the Gate (G) terminal. (c) Output characteristics of the 2D $ReSe_2$ FET shown in the inset, taken for different back gate biases. The measurements were taken at room temperature and under vacuum ($P = 10^{-3}$ Torr). (d) Output characteristic curves of a device with TiO nanoparticle ink as an active channel, in dark (blue curve) and under illumination (300nm - black curve, 550nm - red curve and 800nm - green curve). The measurements were taken at room temperature, without back-gate bias ($V_{bg} = 0V$) and under vacuum ($P = 10^{-3}$ Torr).

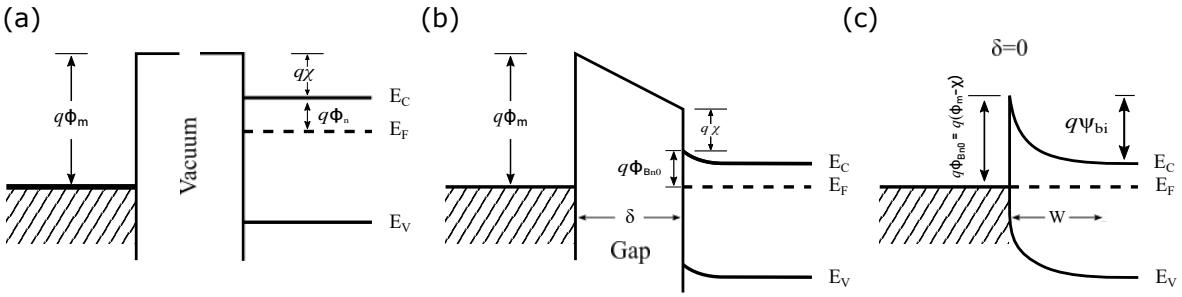

Figure 2.6: Energy-band diagrams describing the formation of Schottky barrier. (a) Metal (left) and semiconductor (right) as separated systems. (b) Metal and semiconductor in close contact with a separation length δ, connected in one system. (c) The Schottky barrier is formed when $\delta \to 0$.

called *Schottky-Mott rule* and predicts the height of the Schottky barrier.

The formation of a Schottky barrier between a metal with high work function and a n-type semiconductor is shown in Figure 2.6, where we consider the ideal case where no surface traps or other defects are present. When the two materials are isolated, they keep their band characteristics (Figure 2.6 (a)). However, the moment they start interacting and charge flow is established at a separation length δ, then thermal equilibrium is achieved at the system and the Fermi energies are aligned (Figure 2.6 (b)). Specifically, the Fermi energy of the semiconductor is reduced by the difference between the two work functions, relative to the Fermi level of the metal.

The work function of a material is defined as the energy difference between the Fermi energy and the vacuum level of this material. In this analysis, the work function of the metal is denoted as $q\,\phi_m$ and in the case of the semiconductor is the sum $q(\chi+\phi_n)$, where $q\chi$ is the electron affinity measured from the bottom of the conduction band, while E_C and $q\phi_n$ is the energy difference between E_C and the Fermi energy of the semiconductor (E_F). The potential difference between the two work functions, $\phi_m - (\chi + \phi_n)$, is called *contact potential.* As the separation δ between the metal and the semiconductor decreases, the electric field within the gap increases, making the negative charge flowing in from the semiconductor to the metal to accumulate on the metal surface. This leads also to an accumulation of an equal positive charge inside the semiconductor depletion region (W). When $\delta \to 0$, the gap becomes transparent to electrons and the limiting value of the potential barrier height $q\phi_{Bn0}$ is

$$q\phi_{Bn0} = q(\phi_m - \chi). \tag{2.15}$$

However, in reality such a simple description of a Schottky barrier height is never achieved, because an interface layer between the metal and the semiconductor is always formed, making $\delta \neq 0$ along with the existence of interface states (e.g. dangling bonds). Since the mechanism is not entirely predictable, the fabrication of the desired contact for a device is not trivial and there is a great amount of research effort directed towards contacts engineering.

Macroscopically, the quality of a contact is expressed by the parameters of *specific contact resistivity* (or *specific contact resistance*), ρ_c ($\Omega\,\mathrm{cm}^2$), and *contact resistance* R_C (Ω)[23]

$$\rho_c = \left(\frac{\partial J}{\partial V}\right)^{-1}_{V\to 0}, \quad R_C = \frac{\rho_c}{A_c}, \tag{2.16}$$

where A_C is the area of the contact that overlaps with the semiconductor.

From the above, it is evident that when characterising the resistivity (or conductivity) of a semiconducting material, the existence of metal contacts affects the measurements. As a result, special measuring techniques need to be implemented to bypass the effect of the contacts and gain a result just for the material itself. In general, several methods are being used. However, we will analyse the two methods used in the presented research, which are the *Transfer Length Method* and the *four terminal contact resistance method*.

The Transfer Length Method, often abbreviated as TLM (also know as *Transmission Line Measurement*), requires a semiconducting channel with more than three identical metal contacts deposited on top but with different spacing between them, as shown in Figure 2.7 (a). Here, a simplified version of the method is presented, emphasising only on some key points that were used in the research. Several aspects that were either not applicable in the cases studied or concern parameters that did not need to be calculated for the purposes of the experiment are omitted. This method combines the easiness of the two-terminal measurements along with a straightforward data analysis which provides relatively robust results.

When characterising a semiconducting device, its total resistance R_T is a sum of

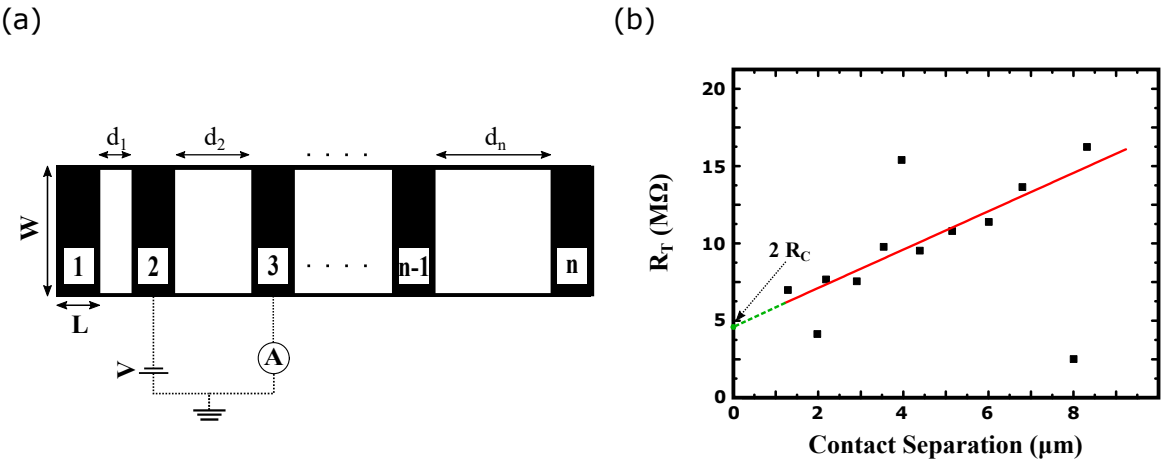

Figure 2.7: Transfer Length Method. (a) Device geometry and measuring circuit (dashed lines) for Transfer Length Method. The metal contacts have the same geometrical characteristics: they cover the full width of the channel and the separation for each pair is different. For determining the contact resistance, multiple two-terminal measurements of the adjacent contact pairs are needed, with prior knowledge of the separation between them. (b) Data of total resistance (R_T) plotted as a function of the separation between the contact pairs. The red line is fitted on the measured data and by extrapolating it at $d = 0$ (green dashed line), we get a value for contact resistance, R_C.

the resistance of the channel and the resistance caused by the contacts

$$R_T = 2R_m + 2R_C + R_{sc} \tag{2.17}$$

where R_m is the resistance of the metal(s) comprising the contacts, R_C is the contact resistance and R_{sc} is the resistance of the semiconducting channel. The contact and metal resistance is multiplied by a factor of 2, since the carriers pass through two metal contacts in a two-terminal measurement, the Source terminal and the Drain terminal contact.

Usually, $R_m \ll R_C$ and so it is ignored in most of the cases. For R_{sc} it is known that

$$R_{sc} = \rho_s \frac{d}{W} \ , \tag{2.18}$$

where ρ_s is the semiconducting channel's resistivity, d is the length and W the width of the contact. Thus, Eq. (2.7) gives

$$R_T = 2R_C + \rho_s \frac{d}{W} \, . \tag{2.19}$$

This is the equation of a straight line of slope ρ_s/W, while for $d = 0$ the contact resistance is obtained. Finally, the *transfer length* is calculated by taking the intercept of the fitted line at $R_T = 0$, giving $2L_T = d|_{(R_T=0)}$. The transfer length can be thought of as the distance over which most of the current transfers from the semiconductor into the metal or vice-versa. The last result is obtained after taking into account several simplifications of a more general equation than Eq. (2.19) but this detail is out of the scope of this thesis. For a detailed analysis of the method, the reader is redirected to the textbook of D.K. Schroder [20].

From the graph in Figure 2.7 (b) we can see that there is some uncertainty in the fitted line, which leads to errors in the calculation of R_T and ρ_c. Additionally, the uncertainty of the exact value of sheet resistance under the contacts (along with the assumption of constant electrical and geometrical contact parameters across the device) add even more to the error of the calculations.

The last method that was used during the experiments that led to this PhD thesis is the *four-terminal method*. These measurements are used to evaluate the intrinsic transport properties of 2D materials by isolating and separating, to some degree, the effects of the conducting metal conductor or the Schottky barriers formed between the metal conducts and the semiconducting channel.

The working principal of four-terminal method along with the appropriate circuit is illustrated in Figure 2.8 (a), where the device is under bias, applied between contact 1 and contact 4. At this point, the current I flowing through the device is stable and same through the whole channel, because the voltmeter connected at contacts 2 and 3 has very high input impedance ($Z \geq 1\,\mathrm{G}\Omega$) prohibiting the current to flow through it. Hence, the voltage drops across the voltage probe and the contact of the metal with the semiconducting channel are negligibly small and can be neglected. As a result, the measured voltage is essentially the voltage drop across the tested device (i.e. between contacts 2 and 3 in Figure 2.8 (a)) and the semiconducting channel's resistance (R_{sc}) can be extracted from the four-terminal I-V characteristics by using [24]

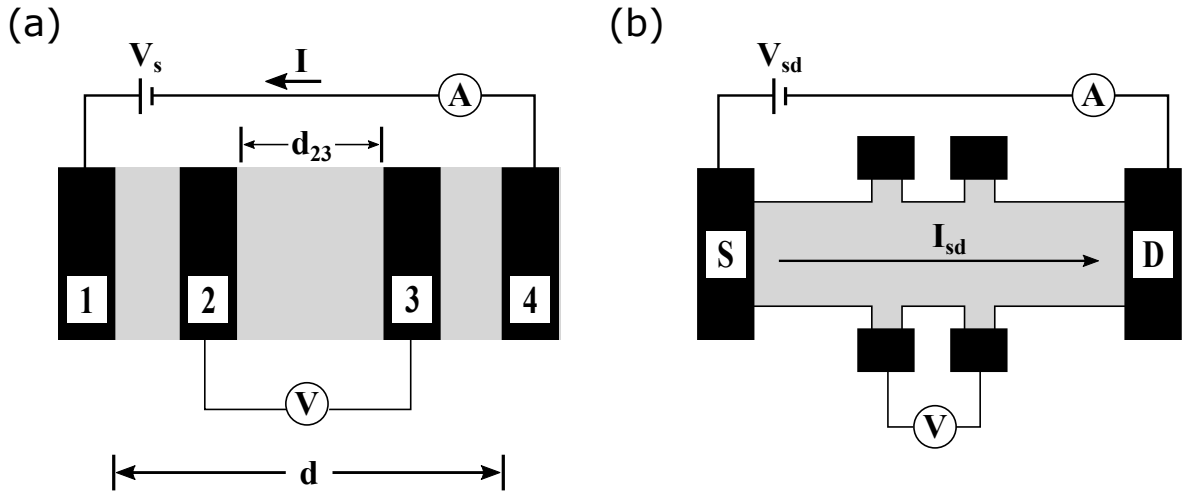

Figure 2.8: Four-terminal contact resistance method. (a) Device geometry and measuring circuit for the four-terminal method. Ideally, the contacts need to cover the whole width of the channel to avoid current flow around the contact. The voltmeter used to measure the voltage drop between contacts 2 and 3 has a high-input impedance to minimise the current flow through it. (b) Hall bar geometry used in four-terminal measurements. Here, the voltage probes are located further away from the channel of the device where the carriers' transport is taking place. Since the voltmeter has high input impedance, there is no current flow through the voltage probes and on average the flow of charges is restricted to the direction parallel to the channel.

$$R_{sc} = \frac{V_{23}}{I}\frac{d}{d_{23}}\,, \tag{2.20}$$

where d is the length of the semiconducting channel and d_{23} is the length of the channel between contact pads 2 and 3.

Furthermore, the contact resistance (R_C) can be extracted by subtracting the calculated channel resistance R_{sc} from the total (or two terminal) resistance, R_T.

Although four-terminal method is generally preferred for the characterisation of 2D devices, it has several disadvantages that need to be taken into account. First of all, in 2D materials, the middle probes affect the transport of the carriers. Due to the atomical thickness of the material, when the voltage probes are deposited directly on the channel they affect the flow of carriers inside the material. Specifically, the

depletion region of the Schottky barrier created can be comparable to the thickness of the channel, thus restricting the flow of carriers.

An alternative method for contact deposition would be to fabricate a *Hall bar* geometry, where the contacts are located further away from the channel where the current is flowing, as illustrated in Figure 2.8 (b). However, this means reshaping of the channel material by using processes (mainly Reactive Ion Etching (RIE)) which can affect the intrinsic transport properties of the material. Finally, the assumption that no current is flowing through the voltage probes is valid only if the input impedance of the voltmeter (Z) is much higher than the channel's resistance ($Z \gg R_C$), which experimentally is translated to $Z/R \geqslant 10^2$. This condition is not always fulfilled, especially when a device is in the OFF state ($V_{bg} < V_T$)), where the channel is completely depleted of carriers and the resistance of the channel is very high.

2.2.3 *Photoresponsivity*

Photoresponsivity, $R = I_{ph}/P_{opt}$, is one of the most important figures-of-merit of a photodetector and measures the electrical output I_{ph} per optical input power. All photoresponsivity measurements presented here were performed with the setup described in Section 2.2.1.2.

The process includes the measurement of the photocurrent produced by impinging light over a wide spectral area, mostly between 350 nm and 1100 nm. However, the emission spectrum, and consequently the emitted power of the lamp changes with time and for this reason an additional calibration measurement is needed. Then, right before or after the main measurement, the lamp's emission spectrum is measured over the same spectral area by using a calibrated photodiode (*ThorLabs* FDS1010). Only then the optical power can be efficiently determined to allow proper data analysis.

2.2.4 *Scanning Photocurrent Mapping*

Scanning Photo-Current Mapping (SPCM) is a technique that allows the mapping of the spatial distribution of the photocurrent. For performing SPCM the microscope setup described in Section 2.2.1.1 is used. Initially, the sample is attached on the PCB that bears the electrical contacts circuit which takes the generated signal out of the device and leads it to the BNC box where the measuring instruments are connected.

Then, the sample is loaded in the vacuum chamber and an appropriate wavelength laser beam is focused on the device and the induced photocurrent is recorded as a function of position. The local photoconductivity is mapped with sub-micrometer precision due to the diffraction limited spot size and the $\sim 100\,\text{nm}$ resolution of the stage.

2.2.5 *Photoluminescence Spectroscopy*

All semiconducting optoelectronic devices belong to the family of *luminescent devices*. Luminescence is the emission of optical radiation (infra-red, visible, ultra-violet) resulting from the excitation of electrons in the device's active material and the subsequent radiative recombination of the excited carriers. Depending on the type of the source of excitation, luminescence can be distinguished in 4 categories, which are *photoluminescence*, *cathodoluminescence*, *radioluminescence* and *electroluminescence*.

In cathodoluminescence, the excitation source is an electron beam or a cathode ray, while in radioluminescence the excitation is caused by other fast particles or even high energy radiation. Electroluminescence is caused by an electric field or a current and finally, the source of photoluminescence is impinging optical radiation.

In-situ measurements of the electroluminescence and the photoluminescence spectra of the devices were possible with the setup described in Section 2.2.1.1. As was mentioned in Section 1.2, monolayer TMDs have direct bandgap and large exciton binding energy. Thus, even at room temperature these material exhibit strong light emission, which makes them promising for light-emitting applications.

2.3 HALL EFFECT

Hall measurements are essential in the characterisation of semiconductors. Especially, in 2D semiconductors the reduced dimensions of the channel give rise to several interesting phenomena[25–29]. In the research presented here, we used the Hall effect for the determination of carrier concentration in monolayer CVD-grown WSe_2. Therefore, some basic elements of the theory of Hall effect and a brief description of the experimental setup used in this PhD work are presented in the following sections.

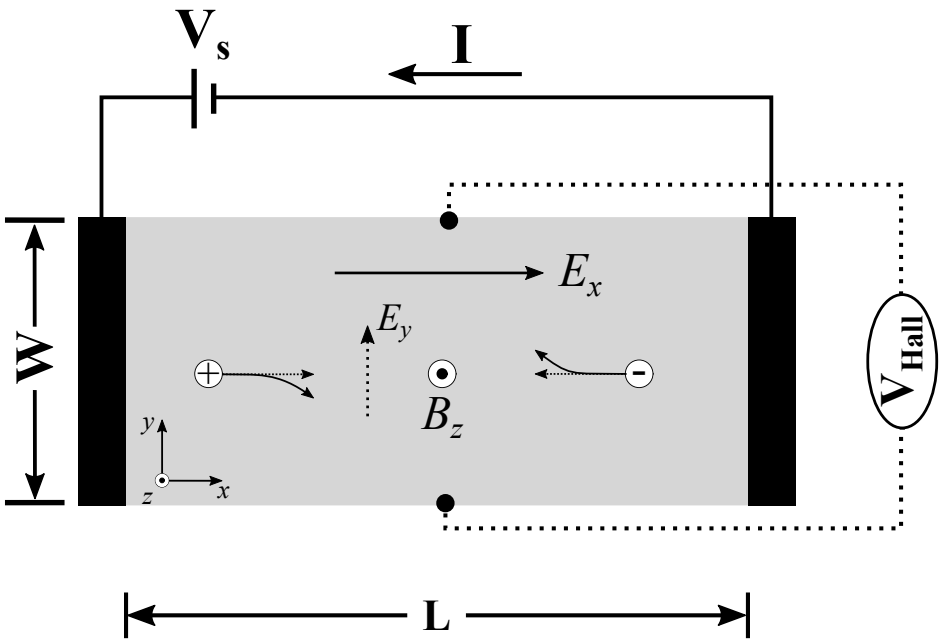

Figure 2.9: Hall effect geometry for 2D material. When magnetic field transverse to the current flow is present, the carriers are experiencing a Lorentz force which makes them accumulating at the edge of the channel. Thus, a transverse electric field is created and steadily increasing up to the point where the Coulomb force exerted on the charge carriers by it balances the Lorentz force from the magnetic field. At this point, a steady state is reached where the carriers' flow is suppressed only parallel to the channel.

2.3.1 *Basic Theory*

Hall effect is one of the most fundamental and useful phenomena as it allows the direct determination of the carrier concentration, the mobility and the charge carrier type (p or n). This phenomenon was named after E. H. Hall who was the first to study it in 1879[30].

Figure 2.9 shows the standard geometry for Hall measurements where an electrical field is applied on the x-direction ($\vec{E} = E_x\hat{x}$) and a magnetic field on the z-direction ($\vec{B} = B_z\hat{z}$). The *Lorentz* force applied on the carriers due to the existence of transverse electric and magnetic field ($\vec{F} = q(\vec{E} + \vec{u} \times \vec{B})$) causes the charges to deviate from their initial path parallel to E_x and accumulate on the edges of the channel. Consequently, the accumulated carriers give rise to an electric field E_y (Hall field) which eventually

stabilises when the force applied by it completely balances the Lorentz force so that the carriers travel in a path parallel to E_x. This is the *steady state* of the system where there is no current flowing on the y-direction.

In the presence of an external magnetic field applied to the material, the magneto-conductivity (σ_{ij}) and magnetoresistivity (ρ_{ij}) relate the current density to the electric field through the identities

$$J_i = \sum_j \sigma_{ij}(B) E_j \,, \quad E_i = \sum_j \rho_{ij}(B) J_j \,, \quad i,j = x,y,z \,. \tag{2.21}$$

The components of the magnetoresistivity tensor can be experimentally determined in a magneto-transport experiment conducted in a Hall bar geometry (Figure 2.9), in the steady state, where $J_y = 0$, as follows

$$\begin{pmatrix} E_x \\ E_y \end{pmatrix} = \begin{pmatrix} \rho_{xx}(B) & \rho_{xy}(B) \\ \rho_{yx}(B) & \rho_{yy}(B) \end{pmatrix} \begin{pmatrix} J_x \\ J_y = 0 \end{pmatrix} \Leftrightarrow \begin{cases} E_x = \rho_{xx}(B) J_x \\ E_y = \rho_{yx}(B) J_x \end{cases} . \tag{2.22}$$

The off-diagonal magnetoresistivity component, ρ_{yx}, is $\rho_{yx}(B) = -\rho_{xy}(B) = \frac{E_y}{J_x}$ which is also known as *Hall resistivity*. From this quantity, one can extract the *Hall coefficient*

$$A_{Hall} = \frac{\rho_{yx}(B)}{B} = \frac{E_y}{B J_x} = \frac{1}{n\, e} \,, \tag{2.23}$$

which is a function of the free charge carrier density and type (+ for hole and - for electrons).

The current flowing parallel to the x-axis is proportional to the current density and the length of the channel (for a 2D material), $I = J_x L$, where L is the length of the channel. The accumulation of carriers at the edges of the channel leads to *Hall potential* $V_{Hall} = E_y W$, where W is the width of the channel.

The simplest application of the Hall theory is achieved when considering an isotropic one-band model (single type of carriers in a parabolic energy band) for a semiconducting 2D channel. Starting from Eq. 2.23 and Eq. 1.16 ($\sigma_x = n_{2D} q_e \mu$), we can calculate the carrier concentration and sign in the semiconducting channel, as well as the mobility

of the carriers as follows

$$n_{2D} = \frac{dB}{\rho_{xy}|q|} = \frac{I/|q|}{dV_H/dB} \quad and \quad \mu = \frac{A_{Hall}}{\rho_{xx}} = \frac{I/|q|}{n_{2D}V_xW/L}\,. \tag{2.24}$$

To use Eq. 1.16 we consider that the basic assumptions of the classical Drude model are valid in the semiconducting channel. Drude built the model for the case of metals, where he approximated the metal as a gas of mobile electrons that collide with positively-charged ions that are immobile and much heavier. However, since free carriers introduced into semiconductors by doping behave in many ways like those in simple metals, the Drude model serves as a good approximation and can be used in this case.

The first hypothesis of the model is that between two collisions, the electrons do not interact with neither ions (*free electron approximation*) nor between them (*independent electron approximation*), thus moving in a straight line. Also, in the frame of this model, an electron undergoes a collision with a probability per unit time $1/\tau$, where τ is known as the *relaxation time* and has an important part in the theory of metal conduction. This means that on average, an electron will travel for a time τ before its next collision. The final of the main assumptions of the model is that thermal equilibrium is achieved only through collisions.

2.3.2 *Experimental setup*

In the research presented here, Hall measurements were performed to determine the carriers concentration and type (i.e. electrons or holes) in CVD-grown WSe_2. The measurements were conducted at cryogenic temperatures with the sample in vacuum using a ICE^{CP} *COLD PROBE* where the sample is loaded, after it is attached to a 3D-printed, 1cm $\times$ 1cm receptacle that bears 12 electrical connections. A superconducting magnet is attached to the end of the probe, with the sample resting in the middle of the solenoid, which can create a varying magnetic field up to 2T.

The ICE^{CP} COLD PROBE is operated in a cryogenic dewar containing liquid helium, $T \sim 4.15$K.

BIBLIOGRAPHY

[1] Y. Y. Wang, Z. H. Ni, T. Yu, Z. X. Shen, H. M. Wang, Y. H. Wu, W. Chen, and A. T. S. Wee. Raman studies of monolayer graphene: The substrate effect. *The Journal of Physical Chemistry C*, 112(29):10637–10640, jun 2008.

[2] A. Jorio, R. Saito, G. Dresselhaus, and M. S. Dresselhaus. *Raman Spectroscopy in Graphene Related Systems*. Wiley-VCH Verlag GmbH & Co. KGaA, jan 2011.

[3] A. C. Ferrari, J. C. Meyer, V. Scardaci, C. Casiraghi, M. Lazzeri, F. Mauri, S. Piscanec, D. Jiang, K. S. Novoselov, S. Roth, and A. K. Geim. Raman spectrum of graphene and graphene layers. *Physical Review Letters*, 97(18):187401, oct 2006.

[4] H. Li, Q. Zhang, C. C. R. Yap, B. K. Tay, T. H. T. Edwin, A. Olivier, and D. Baillargeat. From bulk to monolayer mos_2: Evolution of raman scattering. *Advanced Functional Materials*, 22(7):1385–1390, jan 2012.

[5] A. Das, S. Pisana, B. Chakraborty, S. Piscanec, S. K. Saha, U. V. Waghmare, K. S. Novoselov, H. R. Krishnamurthy, A. K. Geim, A. C. Ferrari, and A. K. Sood. Monitoring dopants by raman scattering in an electrochemically top-gated graphene transistor. *Nature Nanotechnology*, 3(4):210–215, mar 2008.

[6] D. M. Basko, S. Piscanec, and A. C. Ferrari. Electron-electron interactions and doping dependence of the two-phonon raman intensity in graphene. *Physical Review B*, 80(16):165413, oct 2009.

[7] M. A. Pimenta, G. Dresselhaus, M. S. Dresselhaus, L. G. Cançado, A. Jorio, and R. Saito. Studying disorder in graphite-based systems by raman spectroscopy. *Phys. Chem. Chem. Phys.*, 9(11):1276–1290, 2007.

[8] S. Mignuzzi, A. J. Pollard, N. Bonini, B. Brennan, I. S. Gilmore, M. A. Pimenta, D. Richards, and D. Roy. Effect of disorder on raman scattering of single-layer mos_2. *Physical Review B*, 91(19):195411, may 2015.

[9] J. E. Lee, G. Ahn, J. Shim, Y. S. Lee, and S. Ryu. Optical separation of mechanical strain from charge doping in graphene. *Nature Communications*, 3(1), jan 2012.

[10] A.s Castellanos-Gomez, R. Roldán, E. Cappelluti, M. Buscema, F. Guinea, H. S. J. van der Zant, and G. A. Steele. Local strain engineering in atomically thin mos_2. *Nano Letters*, 13(11):5361–5366, oct 2013.

[11] K. Nakamoto J. Ferraro. *Introductory Raman Spectroscopy*. Academic Press, January 2003.

[12] D. A. Long. *The Raman Effect: A Unified Treatment of the Theory of Raman Scattering by Molecules*. WILEY, May 2002.

[13] S.-Y. Lee. Placzek-type polarizability tensors for raman and resonance raman scattering. *The Journal of Chemical Physics*, 78(2):723–734, jan 1983.

[14] T. R. Hart, R. L. Aggarwal, and B. Lax. Temperature dependence of raman scattering in silicon. *Physical Review B*, 1(2):638–642, jan 1970.

[15] G. E. Jellison, D. H. Lowndes, and R. F. Wood. Importance of temperature-dependent optical

properties for raman-temperature measurements for silicon. *Physical Review B*, 28(6):3272–3276, sep 1983.

[16] X. Zhang, X.-F. Qiao, W. Shi, J.-B. Wu, D.-S. Jiang, and P.-H. Tan. Phonon and raman scattering of two-dimensional transition metal dichalcogenides from monolayer, multilayer to bulk material. *Chemical Society Reviews*, 44(9):2757–2785, 2015.

[17] J. L. Verble and T. J. Wieting. Lattice mode degeneracy in mos_2 and other layer compounds. *Physical Review Letters*, 25(6):362–365, aug 1970.

[18] J. Ribeiro-Soares, R. M. Almeida, E. B. Barros, P. T. Araujo, M. S. Dresselhaus, L. G. Cançado, and A. Jorio. Group theory analysis of phonons in two-dimensional transition metal dichalcogenides. *Physical Review B*, 90(11):115438, sep 2014.

[19] A. De Sanctis, G. F. Jones, N. J. Townsend, M. F. Craciun, and S. Russo. An integrated and multi-purpose microscope for the characterization of atomically thin optoelectronic devices. *Review of Scientific Instruments*, 88(5):055102, may 2017.

[20] Schroder D. K. *Semiconductor materials and device characterisation.* John Wiley and Sons, January 2006.

[21] F. Braun. Ueber die stromleitung durch schwefelmetalle. *Annalen der Physik und Chemie*, 229(12):556–563, 1875.

[22] W. Schottky. Halbleitertheorie der sperrschicht. *Die Naturwissenschaften*, 26(52):843–843, dec 1938.

[23] C.Y. Chang, Y.K. Fang, and S.M. Sze. Specific contact resistance of metal-semiconductor barriers. *Solid-State Electronics*, 14(7):541–550, jul 1971.

[24] S. B. Mitta, M. S. Choi, A. Nipane, F. Ali, C. Kim, J. T. Teherani, J. Hone, and W. J. Yoo. Electrical characterization of 2d materials-based field-effect transistors. *2D Materials*, 8(1):012002, nov 2020.

[25] Z. Wu, Benjamin T. Zhou, X. Cai, P. Cheung, G.-B. Liu, M. Huang, J. Lin, T. Han, L. An, Y. Wang, S. Xu, G. Long, C. Cheng, K. T. Law, F. Zhang, and N. Wang. Intrinsic valley hall transport in atomically thin mos_2. *Nature Communications*, 10(1), feb 2019.

[26] Z. Jiang, Y. Zhang, Y.-W. Tan, H.L. Stormer, and P. Kim. Quantum hall effect in graphene. *Solid State Communications*, 143(1-2):14–19, jul 2007.

[27] Y. Zhang, Y.-W. Tan, H. L. Stormer, and P. Kim. Experimental observation of the quantum hall effect and berry's phase in graphene. *Nature*, 438(7065):201–204, nov 2005.

[28] O. L. Berman, R. Ya. Kezerashvili, and Y. E. Lozovik. Spin hall effect for polaritons in a transition metal dichalcogenide embedded in a microcavity. *Physical Review B*, 99(8):085438, feb 2019.

[29] T. Cao, G. Wang, W. Han, H. Ye, C. Zhu, J. Shi, Q. Niu, P. Tan, E. Wang, B. Liu, and J. Feng. Valley-selective circular dichroism of monolayer molybdenum disulphide. *Nature Communications*, 3(1), jan 2012.

[30] E. H. Hall. On a new action of the magnet on electric currents. *American Journal of Mathematics*, 2(3):287, sep 1879.

3

CONTRAST ANALYSIS OF GRADIENTLY PHOTO-INDUCED HFO_2

NOTE: The ideas and data presented in this chapter have been the subject of the following publication: *Laser writable high-k dielectric for van der Waals nano-electronics.* Science Advances, 2019. N. Peimyoo, M. D. Barnes, Jake D. Mehew, A. De Sanctis, I.Amit, J. Escolar, K. A. Anastasiou, A. P. Rooney, S. J. Haigh, S. Russo, M. F. Craciun and F. Withers.

In this publication, my contribution was in the fabrication of the resistive-switching Random Access Memory devices.

INTRODUCTION

Dielectric materials constitute a vital part of all optoelectronic and photonic devices. However, 2D devices are not exhibiting their full potential when they are in contact with commonly used amorphous oxides like silicon oxide, SiO_2. This is due to the existence of many defects inside and on the surface of these materials which create defect states that hamper the electrical transport properties in 2D materials[1,2]. Furthermore, some of the industrially used dielectrics are not inert and react with the 2D semiconducting layers, greatly affecting the channel properties and limiting the capabilities of the examined device[3–5].

A possible solution to this problem would be to substitute these materials with 2D dielectrics, such as HfO_2, ZrO_2, hBN and CaF, among others. These materials have dangling bond-free surfaces resulting in sharp interfaces with 2D semiconductors. Additionally, layered dielectrics like hexagonal boron nitride (hBN) can be exfoliated

and stacked with other TMDs to make complex vdW heterostructures, resulting in more complex and sophisticated devices while maintaining two-dimensional character (i.e. clean interfaces, reduced defects, nano-scale dimensions, high exciton energies, transparency and flexibility). However, hBN is shown to have extremely large leakage currents for sub-1nm equivalent oxide thickness (the thickness of SiO_2 which would produce the same capacitance as the insulator in use) which is due to its rather narrow bandgap and low permittivity[6]. A more suitable candidate for the replacement of currently used dielectrics would be HfO_2, which is the native oxide of the TMD HfS_2 and is shown to have a very high dielectric constant.

Bulk three-dimensional hafnium oxide can be grown by a number of methods including CVD, atomic layer deposition and sputtering. However, none of the aforementioned methods is suitable for the synthesis of a single layer of HfO_2. For this task, a novel approach is required such as the recently discovered photo-oxidation of HfS_2 first demonstrated by De Sanctis et al[7]. This technique can revolutionise the fabrication of 2D devices, as it is simple in application and produces high quality oxide. However the novelties do not stop here, as it also allows the oxidation of a HfS_2 within a vdW heterostructure without affecting the surrounding layers. Finally, it allows the detailed definition of nano-patterns of HfO_2 on the HfS_2 flake, opening new paths for atomically thin waveguides and their implementation to complex nanophotonic and nanoelectronic hybrid systems.

In this chapter the photo-oxidation process will be presented, along with a study of optical contrast between photo-oxidised areas which were exposed to different laser powers and for different time. This study will reveal the level of oxidation along this gradient of HfO_2 which is an important step in understanding the layer-by-layer formation of the oxide. Ultimately, photo-oxidised HfS_2 can play a central role in the development of 2D graded dielectrics.

3.1 PHOTO-OXIDATION MECHANISM

A major part of the research presented in this dissertation is on photo-oxidised Hafnium disulfide (HfS_2) and its use as a high-k ($k \sim 15$)[8] dielectric in 2D devices. Therefore, a description of the mechanism of photo-oxidation of HfS_2 is essential for understanding the phenomenon and the innovation behind the technique that was used.

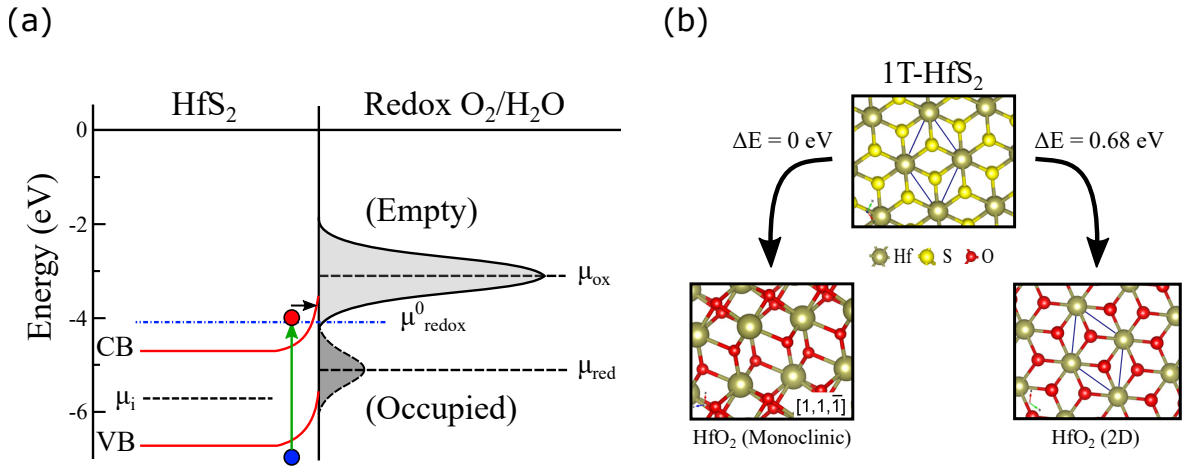

Figure 3.1: Charge-transfer model for the photo-oxidation of HfS_2. (a) Schematic energy diagram of multi-layer HfS_2 in contact with the redox couple O_2/H_2O present in air in ambient conditions[14]. The following parameters were used for the calculation of the redox couple Density of States (DOS): the chemical potentials of the oxidizing and reducing species are $\mu_{ox} = -3.1\,\text{eV}$ and $\mu_{red} = -5.1\,\text{eV}$, respectively; the chemical potential of the oxygen acceptor state is $\mu^0_{redox} = -4.1\,\text{eV}$; the intrinsic work function of HfS_2 is $\mu_i = -5.7\,\text{eV}$ with $E_g = 1.96\,\text{eV}$. (b) Simulated crystal structure of 1T-HfS_2, monoclinic HfO_2 and 2D HfO_2. The energy required for the reactions leading to the formation of the oxides is shown in respect to the formation of monoclinic HfO_2 ($\Delta E = -11.58\,\text{eV}$). Adapted with permission[7].

HfS_2 is a semiconducting TMD crystallising in a 1T phase, with an indirect bandgap that ranges between 2 eV[9] and 2.8 eV (bulk)[10] decreasing down to approximately 1.2 eV for monolayer material[11]. When the material is exposed to light of appropriate wavelength and power in ambient conditions, it oxidises due to charge transfer between the surface and oxygen in the air, or surface-bound water[7,12,13].

Specifically, the oxidation occurs via the *oxygen-water redox couple*. Redox, or reduction-oxidation, is a chemical reaction where the oxidation states of atoms change due to transfer of electrons between chemical substances. The oxygen-water redox reaction occurs in ambient conditions wherever moisture is present

$$2H_2O \rightleftharpoons O_2\,(aq) + 4e^- + 4H^+\,, \tag{3.1}$$

and creates the O_2 which will bind to Hf and S atoms of HfS_2.

The model for the reaction leading to the formation of HfO_2 is shown in Figure 3.1 (a). It is important to highlight that photo-oxidation relies on the band alignment of the material with the redox potential and as a result, only specific 2D materials can be photo-oxidised. In that model, the intrinsic chemical potential of HfS_2 is $\mu_i = -5.2\,\text{eV}$ (calculated from the distance from the vacuum level to the top of the valence band, $\phi = -6.68\,\text{eV}$ and indirect bandgap $E_g = 1.96\,\text{eV}$), while that of the oxygen acceptor state is $\mu^0_{redox} = -4.1\,\text{eV}$. This induces a band-bending at the surface of the layered semiconductor such that an optical transition above the bandgap can make an electron ready to be transferred to the oxygen empty states, making the photo-oxidation reaction highly feasible across the whole visible range, explaining the high instability of few-layer HfS_2 in atmospheric conditions[7].

When the material is exposed to light, impinging photons of energy $h\nu$ optically excite HfS_2

$$HfS_2 + h\nu \longrightarrow HfS_2{}^* \,, \tag{3.2}$$

which creates an abundance of carriers that will take part to the charge transfer process at the surface of the material, as described by

$$HfS_2{}^* + O_2\,(aq) \longrightarrow HfS_2 + O_2{}^{\bullet-}(aq) + h^+ \,. \tag{3.3}$$

The produced oxygen radical ion $O_2{}^{\bullet-}(aq)$ then reacts with HfS_2 and upon cleavage of the Hf-S bond binds to both substances

$$Hf + 2S + 3O_2{}^{\bullet-}(aq) + 3h^+ \longrightarrow HfO_2 + 2SO_2(g)\,. \tag{3.4}$$

The above reactions can be combined to give a single chemical reaction that describes the whole process

$$HfS_2(s) + 3O_2(aq) + h\nu \longrightarrow HfO_2(s) + 2SO_2(g)\,. \tag{3.5}$$

In the model described above, the energy costs for the formation of different crystal phases of HfO_2 were calculated, for Eq. (3.5). The most favourable was found to be the formation of monoclinic HfO_2 with an energy cost of -11.58 eV per HfS_2, while the formation of two-dimensional (2D) or cubic HfO_2 have higher energy requirements. Thus, the photo-oxidation of HfS_2 in ambient conditions leads to the formation of

monoclinic HfO_2. The crystal structure of HfS_2, monoclinic HfO_2 and 2D HfO_2 can be seen in Figure 3.1 (b).

As a consequence of photo-oxidation of HfS_2, the bandgap of the material is increased to $E_g \sim 4\,\text{eV}$, resulting in an electrical insulating material[8,15–17]. Furthermore, the photo-oxidation can occur even when the HfS_2 layer is embedded in heterostructures, or even under metal contacts due to the diffraction of light in the latter. The mechanism likely involves migration of interfacial water between the 2D material-HfS_2/HfO_x interface to the reaction site that is being irradiated. Upon exfoliation, the surface layer of the HfS_2 will naturally oxidize within 10 to 15 minutes prior to encapsulation, which could allow for diffusion of atmospheric water between the graphene and the more hydrophilic HfO_x surface. Similar diffusion effects have previously been observed for graphene on SiO_2[18]. This selective oxidation of HfS_2 in complex heterostructures, allows the definition of the insulating layer after the fabrication of complex devices without using invasive or destructive techniques.

3.2 IMPLEMENTATION OF THE PHOTO-OXIDATION PROCESS

The oxidation of HfS_2 was carried out by exposing the microcleaved 2D semiconductors to blue ($\lambda = 473\text{nm}$) or UV ($\lambda = 375\text{nm}$) laser light in ambient conditions. The control of the laser source as well as the stage is crucial for writing correctly the desired pattern on the flake and for this reason a custom-made, *NI LabView*-based software was used. This software accepts as input the desired laser parameters as well as a pattern that the user has defined prior to the oxidation. By choosing the correct scale at the software's interface, the desired pattern is written with very high precision due to the diffraction limited laser light spot and the $\sim 100\,\text{nm}$ resolution of the stage.

3.3 FORMATION OF HFO_x

To demonstrate the creation of a uniform layer of HfO_x and perform an initial characterisation of the laser-written HfO_x we fabricated a MoS_2 FET with an $8\,nm$ HfS_2 flake separating bottom layer of graphene that serves as gate electrode and the Cr/Au contacts deposited on top, as shown in Figure 3.2 (a). After laser exposure, the transparency of the HfS_2 film increases significantly, indicating an increase in the bandgap to

much larger values than the 2.85 eV characterising HfS_2, consistent with the formation of an oxide ($E_g \simeq 5.5\,\text{eV}$, expected for HfO_x [19]).

Vertical electron transport through the oxide further supports the transformation to the oxide and indicates that oxidation occurs not only under the flakes of 2D materials but also under the thick Au contacts ($d = 60\,\text{nm}$) facilitated by diffraction of the laser beam around the approximately micrometer-wide contacts. Figure 3.2 (b) shows the I_{sd}-V_{sd} characteristics for such a device. I_{sd}-V_{sd} values were collected using a *Keithley 2400* voltage/current source meter. Before oxidation, the I_{sd}-V_{sd} shows the typical nonlinear behaviour expected for electron transport through a series of semiconducting materials [22], with a low-bias vertical resistivity $R \simeq 20 \times 10^6\,\Omega\,\mu\text{m}$. After oxidation, the resistivity around $V_{sd} = 0\,\text{V}$ increases to $R \sim 10^{11}\,\Omega\,\mu\text{m}$, consistent with an increased barrier height.

Further evidence for the oxidation of the oxidation of HfS_2 are given by means of Energy-dispersive x-ray spectroscopy (EDX) analysis of a simple heterostructure constituting of HfO_x sandwiched between two graphene layers on SiO_2, where the HfO_x channel results from the photo-oxidation of a HfS_2 layer. Figure 3.2 (c) shows a high-resolution Scanning Transmission Electron Microscopy (STEM) image [20,21] of the cross section of this device, where the few-layer top and bottom graphene electrodes are still clearly visible, while the long-range crystal order of HfS_2 is lost and the resultant material appears in an amorphous phase. EDX analysis confirms that the only species present in this phase are hafnium and oxygen, with only low levels of sulfur left after laser irradiation, as shown in the right panel of Figure 3.2 (c).

For further details regarding the properties of the photo-induced oxide, see Section 4.2.

3.4 CONTRAST STUDY OF GRADED PHOTO-OXIDISED HFS_2

The photo-oxidation of HfS_2 depends highly on the laser power, the exposure time, the concentration of O_2 and H_2O as well as the thickness of the flake. Thus, it is possible to control these parameters in order to achieve a layer-by-layer oxidation of the HfS_2 flake. This can be very important for the creation of graded dielectrics, such as graded refractive index materials that can be used to define waveguides in vdW heterostructures. In our system, we use a custom-made *LabView* software to control

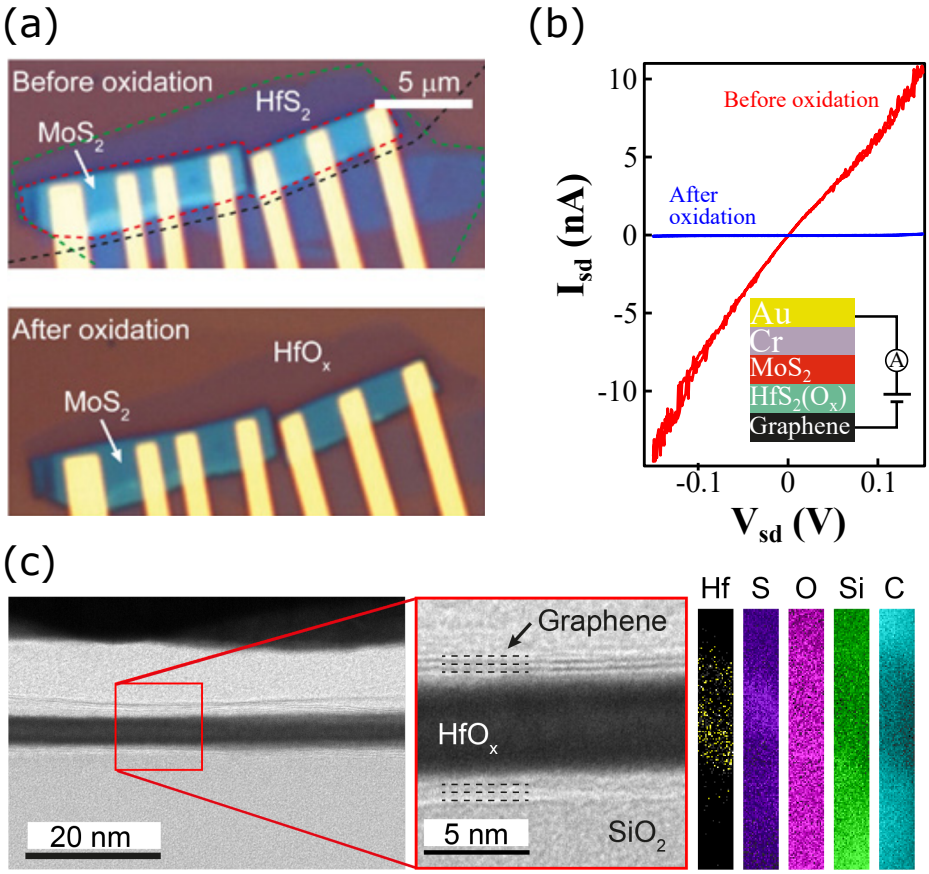

Figure 3.2: Formation of HfO_x insulating layer. (a) Optical image of a graphene-HfS_2/MoS_2 heterostructure before (top) and after (bottom) oxidation. Black outlines the region of the graphene back gate, green outlines the HfS_2, and red outlines the MoS_2. (b) Current (I_{sd}) versus applied voltage (V_{sd}) for the heterostructure in (a) before (red) and after (green) photo-induced oxidation. Inset shows the stacking sequence. (c) High resolution STEM image showing a cross section of a graphene/HfO_x/graphene device on SiO_2 after laser-assisted oxidation (left) and EDX elemental analysis (right). The panels on the right part of the image correspond to the cross section of the heterostructure shown in the middle panel. The bright spots represent detected atoms of the corresponding element in this heterostructure, thus higher brightness corresponds to higher concentration of an element at the corresponding area. For convenience, red dashed lines extend the HfO_x channel of the middle panel to the EDX elemental maps on the right.

the laser power and set it to gradually increase/decrease with each step when oxidising HfS_2.

Upon oxidation, a HfS_2 flake becomes transparent for optical wavelengths as the bandgap of the newly-formed HfO_2 increases to $\sim 5.5\,\text{eV}$ [8]. When a multi-layer HfS_2 flake is written with varying laser power, the contrast along the written area changes gradually from the region of HfS_2 to the transparent fully oxidized part of the sample. Therefore, optical contrast study can reveal the level of oxidation of the semiconductor.

So far there are many attempts to establish a way to determine the number of layers of a 2D material with optical contrast analysis [23–26], as it is a very quick and effective way to get the thickness of a semiconductor which is most of the times an important parameter for device fabrication. The analysis presented in this chapter aims to explore the use of contrast analysis to determine the level of oxidation induced in HfS_2 by laser exposure.

3.4.1 *Analysis of graded 2D oxide*

Contrast is the difference in brightness between a specific region of interest relative to the background brightness. The contrast of an object relative to its background is determined by numerous factors like the absorption of light, brightness, reflectance, birefringence, light scattering, diffraction, fluorescence, or color variations. As a result, different semiconducting materials of the same thickness and on the same substrate will exhibit different contrast with the background due to the different bandgap energies which control their absorbance.

There are several definitions and mathematical expressions of contrast that have to do mainly with specific details of the background, the material and the distribution of light and features across the image. In this research we considered the *Webber contrast*

$$C_W = \frac{I_s - \overline{I_b}}{\overline{I_b}}\,, \tag{3.6}$$

and the *Michelson contrast*

$$C_M = \frac{I_s - \overline{I_b}}{\overline{I_b} + I_s^{max}}\,, \tag{3.7}$$

where I_s is the brightness of the examined area (sample), $\overline{I_b}$ is the mean value of the

brightness of the background and I_s^{max} is the maximun intensity of the pristine HfS_2 flake.

Eventually, in our analysis we used the *Michelson* contrast as its values do not strongly depend on the selected substrate.

A CVD-grown HfS_2 crystal purchased from *HQ Graphene* was mechanically exfoliated and transferred on quartz and *p*-doped Si wafer with 300 nm of thermal oxide (SiO_2). Multi-layer flakes of thickness $t \geqslant 20$ nm ($\sim$ 30 HfS_2 layers) were identified by means of optical microscopy and exposed to blue ($\lambda = 473$ nm) laser light of linearly varying power ($P_{in} = 3.7$mW, $P_{fin} = 0$W, $\Delta P/step = 74$µW, step size: 0.25µm, $t_{exp} = 0.2$s) over a length of 50 µm. This resulted in gradients of HfO_2 being written on the flakes, as shown in the panels of Figure 3.3 (a),(b).

To perform the contrast analysis, high-quality optical images of the flakes were acquired and the optical contrast of a multi-layer flake and substrate was directly measured by using the software *ImageJ*. The optical contrast is calculated using the brightness values of the red (R), green (G) and blue (B) channels of the pixels comprising the colour image. RGB pixels are converted to brightness values using the formula $I = (R + G + B)/3$ and these values are used for the calculation of the contrast.

The extracted contrast profile along the specified line is shown in Figure 3.3 (a) for gradient written in a HfS_2 flake exfoliated on top of quartz substrate (Figure 3.3 (b)). Here, the contrast is calculated with respect to the fully oxidised area at the beginning of the gradient (see Figure 3.3 (b)), thus negative contrast values correspond to brighter regions of the image (see Eq. 3.7), while positive values correspond to the darker quartz substrate. This difference between the substrate contrast and that of the fully oxidised region is a result of the loss of power due to the multiple reflections from the layers of oxidised material and absorption from the substrate and the microscope stage. However, since both the oxide and the substrate are transparent, the losses are relatively small, resulting in a contrast difference of ~ 0.06.

By close examination of the curves, it is clear that the contrast value follows the written pattern. It exhibits a steep rise of the contrast value when going from the unoxidised to the fully oxidised part of the gradient and then the contrast values slowly decay, reaching the value of unoxidised flake after about 50 µm. This corresponds to the actual length of the written region, implying that even low laser power can oxidise the upper HfS_2 layer. In Figure 3.3 (a), after the gradient, the contrast values present

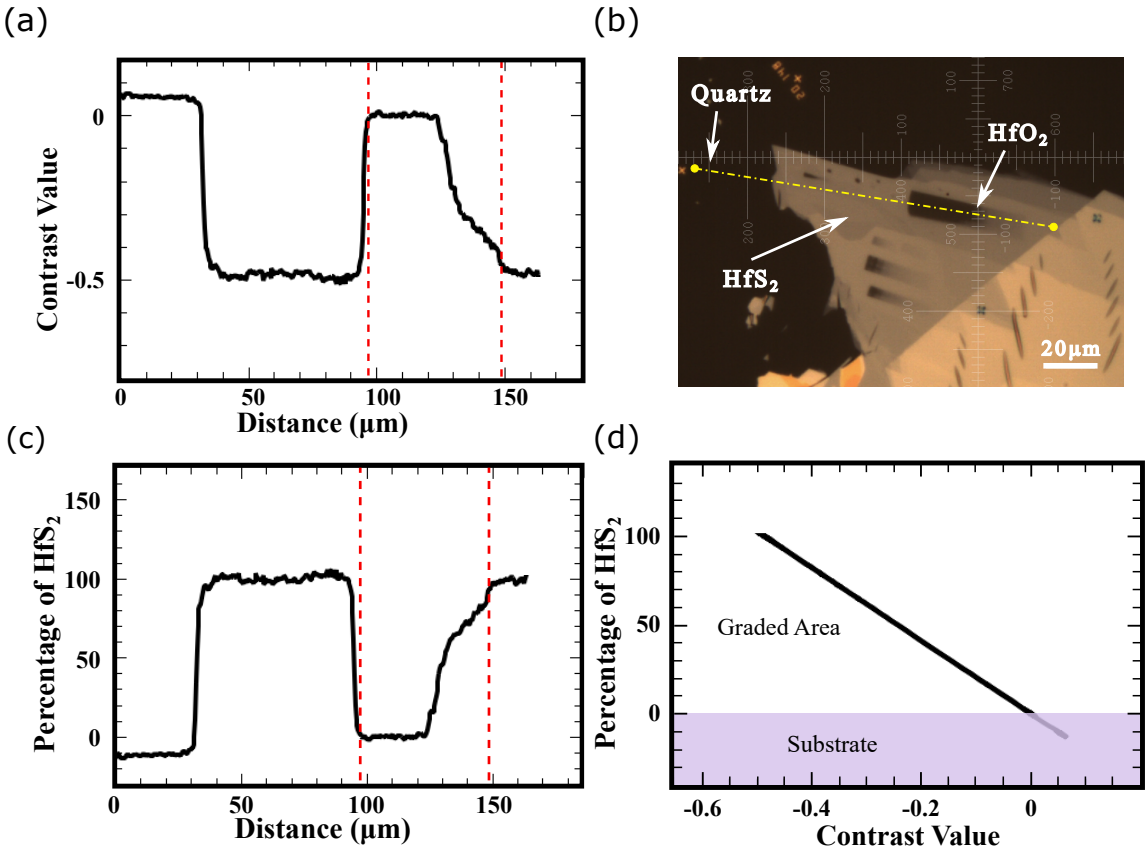

Figure 3.3: Analysis of optical contrast along a HfO_x graded area. (a) Contrast along the line starting from the quartz substrate and finishing outside of the oxidised region. The red vertical lines delimit the length of the graded area. (b) Optical image of the flake with the graded oxide and the path (yellow dashed line) along which contrast is measured. (c) Percentage of remaining HfS_2 along the line shown in panel (b). The red vertical lines delimit the length of the graded area. (d) Percentage of remaining HfS_2 as a function of contrast value for sample shown in panel (b). Negative contrast values correspond to the quartz substrate while values higher than 100% correspond to thicker unoxidised material.

a steep fall, which is due to the increase of thickness of the flake on the right side (see Figure 3.3 (b)), making it appearing brighter.

The part of the graded area that was exposed to the higher laser power shows almost zero contrast with the SiO_2 reference background (the small difference from the values of SiO_2 region are due to the aforementioned energy losses). Along with the uniformity the material shows after oxidation under examination with optical microscope (see Figure 3.3 (b)), we have strong evidence that the HfS_2 oxidation is only complete, with only residues of sulfur remaining (as in Figure 3.2 (c). The uniformity of the material is important, as it shows that the oxidation process did not lead to extreme rise of the local temperature in the material causing structural damages which could expose the substrate and thus, affecting the contrast values. More information and examples of damaged flakes due to oxidation process can be found at the supplementary information of De Sanctis et al[7].

As a result, we can estimate the percentage of semiconducting HfS_2 remaining after oxidation, along the line we took the contrast measurements. This estimation is presented in Figure 3.3 (c) and shows that for a length of about 25µm the laser power was high enough to almost completely oxidise the exposed area. After that, the percentage of HfS_2 starts gradually rising, which reveals that the oxidation is not complete and some absorbing semiconducting material remains in the exposed area. As expected, after the 50µm that correspond to the exposed area, the measurements reach a plateau at 100% HfS_2 since these regions were not exposed to laser light.

Finally, a reference plot where the percentage of unoxidised HfS_2 is plotted against the contrast values across the gradient can be seen in Figure 3.3 (d). This can be used as a reference for instantly identifying the level of oxidation and choosing the flake according to the needs of any potential experiment and/or application.

3.5 SUMMARY AND OUTLOOK

In summary, in this chapter the controlled photo-oxidation of ultrathin HfS_2 was presented, showing a straight-forward and non-invasive technique to calculate the percentage of semiconducting material left after oxidation at an area of graded oxide. This graded oxide was created after exposing the semiconducting HfS_2 thin flakes to a raster laser scan of linearly varying power. According to the findings, the photo-oxidation

process is readily controllable and can be used to embed dielectric layers in complex systems, as well as to create graded dielectrics with a variety of applications.

Furthermore, a contrast analysis of an area written by linearly varying laser power was discussed. We showed that optical contrast is a robust method for quick determination of the level of oxidation, which is crucial in avoiding further exposition of the 2D flake to a series of different measurements for determining the appropriate flake to use. Although the findings are already interesting, the gradiently oxidised areas also present high scientific interest as they can be used as waveguides for excitons in vdW heterostructures, which is a concept being tested at the moment.

However, there are several aspects that need further studying. First of all, the contrast method does not provide any information on the layer arrangement of a non-uniformly oxidised area. For example, the oxidation can occur layer-by-layer starting with the top and moving towards the bottom. But it is also possible that the top and bottom layers are oxidised simultaneously, since between the flake and the substrate and at the top of the flake there is the highest concentration of aqueous oxygen. To determine the exact arrangement of the HfS_2 and HfO_2 layers, TEM should be performed on a gradient of HfO_2 to see exactly how the material is oxidised, as it is a very important parameter. This would give more information that would assist in optimising the coupling between the excitons and the photo-induced HfO_2 in vdW heterostructures. Additionally, the effect of the spot size of the focused laser beam on the resulting material should be systematically studied to determine how it affects the resolution of the oxidation (i.e. how uniform is the oxide).

Finally, in order to pursue the development of graded dielectrics from photo-oxidised HfS_2, a detailed characterisation of the refractive index along a gradient of HfO_2 should be performed. In this direction, absorbance spectroscopy and micro-ellipsometry could be used to give a thorough and robust characterisation of the refractive index.

BIBLIOGRAPHY

[1] D. Rhodes, S. H. Chae, R. Ribeiro-Palau, and J. Hone. Disorder in van der waals heterostructures of 2d materials. *Nature Materials*, 18(6):541–549, may 2019.

[2] C. Lee, S. Rathi, M. Atif Khan, D. Lim, Y. Kim, S. J. Yun, D.-H. Youn, K. Watanabe, T. Taniguchi, and G.-H. Kim. Comparison of trapped charges and hysteresis behavior in hbn encapsulated single mos_2 flake based field effect transistors on sio_2 and hbn substrates. *Nanotechnology*, 29(33):335202, jun 2018.

[3] M. Xiao, C. Qiu, Z. Zhang, and L.-M. Peng. Atomic-layer-deposition growth of an ultrathin hfo_2 film on graphene. *ACS Applied Materials & Interfaces*, 9(39):34050–34056, sep 2017.

[4] S. McDonnell, B. Brennan, A. Azcatl, N. Lu, H. Dong, C. Buie, J. Kim, C. L. Hinkle, M. J. Kim, and R. M. Wallace. Hfo_2 on mos_2 by atomic layer deposition: Adsorption mechanisms and thickness scalability. *ACS Nano*, 7(11):10354–10361, oct 2013.

[5] H. G. Kim and H.-B.-R. Lee. Atomic layer deposition on 2d materials. *Chemistry of Materials*, 29(9):3809–3826, apr 2017.

[6] L. Britnell, R. V. Gorbachev, R. Jalil, B. D. Belle, F. Schedin, M. I. Katsnelson, L. Eaves, S. V. Morozov, A. S. Mayorov, N. M. R. Peres, A. H. Castro Neto, J. Leist, A. K. Geim, L. A. Ponomarenko, and K. S. Novoselov. Electron tunneling through ultrathin boron nitride crystalline barriers. *Nano Letters*, 12(3):1707–1710, mar 2012.

[7] A. De Sanctis, I. Amit, S. P. Hepplestone, M. F. Craciun, and S. Russo. Strain-engineered inverse charge-funnelling in layered semiconductors. *Nature Communications*, 9(1), apr 2018.

[8] N. Peimyoo, M. D. Barnes, J. D. Mehew, A. De Sanctis, I. Amit, J. Escolar, K. Anastasiou, A. P. Rooney, S. J. Haigh, S. Russo, M. F. Craciun, and F. Withers. Laser-writable high-k dielectric for van der waals nanoelectronics. *Science Advances*, 5(1), jan 2019.

[9] L. Roubi and C. Carlone. Temperature and pressure dependence of the optical gaps in $hf_{1-x}zr_xs_2$. *Canadian Journal of Physics*, 66(7):633–637, jul 1988.

[10] M. Traving, T. Seydel, L. Kipp, M. Skibowski, F. Starrost, E. E. Krasovskii, A. Perlov, and W. Schattke. Combined photoemission and inverse photoemission study of hfs_2. *Physical Review B*, 63(3):035107, jan 2001.

[11] T. Kanazawa, T. Amemiya, A. Ishikawa, V. Upadhyaya, K. Tsuruta, T. Tanaka, and Y. Miyamoto. Few-layer hfs_2 transistors. *Scientific Reports*, 6(1), mar 2016.

[12] W. Jaegermann and D. Schmeisser. Reactivity of layer type transition metal chalcogenides towards oxidation. *Surface Science*, 165(1):143–160, jan 1986.

[13] A. Favron, E. Gaufrès, F. Fossard, A. L. Phaneuf-L'Heureux, N. Y-W. Tang, P. L. Lévesque, A. Loiseau, R. Leonelli, S. Francoeur, and R. Martel. Photooxidation and quantum confinement effects in exfoliated black phosphorus. *Nature Materials*, 14(8):826–832, may 2015.

[14] R. Memming. *Semiconductor Electrochemistry*. Wiley, Hoboken, 2015.

[15] N. M. R. Peres. Colloquium: The transport properties of graphene: An introduction. *Reviews of Modern Physics*, 82(3):2673–2700, sep 2010.

[16] A. Ramasubramaniam. Large excitonic effects in monolayers of molybdenum and tungsten dichalcogenides. *Physical Review B*, 86(11):115409, sep 2012.

[17] J. Robertson. High dielectric constant oxides. *The European Physical Journal Applied Physics*, 28(3):265–291, dec 2004.

[18] D. Lee, G. Ahn, and S. Ryu. Two-dimensional water diffusion at a graphene–silica interface. *Journal of the American Chemical Society*, 136(18):6634–6642, apr 2014.

[19] M. C. Cheynet, S. Pokrant, F. D. Tichelaar, and J. L. Rouvière. Crystal structure and band gap determination of HfO2 thin films. *Journal of Applied Physics*, 101(5):054101, mar 2007.

[20] A. P. Rooney, A. Kozikov, A. N. Rudenko, E. Prestat, M. J. Hamer, F. Withers, Y. Cao, K. S. Novoselov, M. I. Katsnelson, R. Gorbachev, and S.J. Haigh. Observing imperfection in atomic interfaces for van der waals heterostructures. *Nano Letters*, 17(9):5222–5228, aug 2017.

[21] S. J. Haigh, A. Gholinia, R. Jalil, S. Romani, L. Britnell, D. C. Elias, K. S. Novoselov, L. A. Ponomarenko, A. K. Geim, and R. Gorbachev. Cross-sectional imaging of individual layers and buried interfaces of graphene-based heterostructures and superlattices. *Nature Materials*, 11(9):764–767, jul 2012.

[22] T. Georgiou, R. Jalil, B. D. Belle, L. Britnell, R. V. Gorbachev, S. V. Morozov, Y-J. Kim, A. Gholinia, S. J. Haigh, O. Makarovsky, L. Eaves, L. A. Ponomarenko, A. K. Geim, K. S. Novoselov, and A. Mishchenko. Vertical field-effect transistor based on graphene–WS2 heterostructures for flexible and transparent electronics. *Nature Nanotechnology*, 8(2):100–103, dec 2012.

[23] X. Li, X.F. Qiao, Y.F. Shi, L. Liu, T.J. Wang, X.H. Zhao, and B.L. Liang. Study on the optical properties of res_2 flakes by unpolarized and polarized optical contrast measurements. *Optical Materials Express*, 8(5):1107, apr 2018.

[24] Z. H. Ni, H. M. Wang, J. Kasim, H. M. Fan, T. Yu, Y. H. Wu, Y. P. Feng, and Z. X. Shen. Graphene thickness determination using reflection and contrast spectroscopy. *Nano Letters*, 7(9):2758–2763, jul 2007.

[25] D. Bing, Y. Wang, J. Bai, R. Du, G. Wu, and L. Liu. Optical contrast for identifying the thickness of two-dimensional materials. *Optics Communications*, 406:128–138, jan 2018.

[26] H. Li, J. Wu, X. Huang, G. Lu, J. Yang, X. Lu, Q. Xiong, and H. Zhang. Rapid and reliable thickness identification of two-dimensional nanosheets using optical microscopy. *ACS Nano*, 7(11):10344–10353, oct 2013.

4

LASER WRITABLE HIGH-K DIELECTRIC FOR VAN DER WAALS NANOELECTRONICS

NOTE: The ideas and data presented in this chapter have been the subject of the following publication: *Laser writable high-k dielectric for van der Waals nano-electronics.* Science Advances, 2019. N. Peimyoo, M. D. Barnes, Jake D. Mehew, A. De Sanctis, I.Amit, J. Escolar, K. A. Anastasiou, A. P. Rooney, S. J. Haigh, S. Russo, M. F. Craciun and F. Withers.

In this publication, my contribution was in the fabrication of the resistive switching Random Access Memories devices.

INTRODUCTION

The high quality of the native oxide that can be grown on the surface of silicon has underpinned the wide success of modern micro- and nanoelectronics. In recent years, high-k dielectrics such as HfO_2 have been adopted to reduce the dimensions of nanoelectronic components and boost their performance[1]. Recent work has shown similar native oxides in two-dimensional (2D) materials such as $HfSe_2$, $ZrSe_2$[2], TaS_2[3] and $TaSe_2$[4]. However, use of these oxides embedded within van der Waals (vdW) heterostructures has not been shown. In comparison to silicon, vdW heterostructure devices are likely to play an important role in future electronic device applications[5].

With a rapidly growing family of layered 2D materials[6], the multitude of possible heterostructure combinations available will allow for device designs with unprecedented functionalities and improved performance[2]. To date, many such vdW heterostructure devices have been demonstrated, such as vertical tunneling transistors[7] with nega-

tive differential resistance[8], light-emitting quantum wells[9,10], photovoltaics[11–16] and memory devices[17].

Contrary to the conventional molecular beam epitaxy growth of semiconductor devices, vdW heterostructures make it possible to produce atomically sharp interfaces between different materials (i.e. semiconductors, insulators, semimetals etc.) without concerns for their intercompatibility during fabrication. The absence of dangling bonds on the surface of atomically thin materials allows for the creation of atomically sharp interfaces, eliminating the problem of interdiffusion known to impose severe limitations on the downscaling of devices fabricated by standard semiconductors.

To date, the state-of-the-art vdW devices studied experimentally rely on the use of high-purity hexagonal boron nitride (hBN) as a gate dielectric, a tunnel barrier, or a high-quality substrate material[18]. Such high-quality hBN crystals are not widespread, and scalable chemical vapor deposition versions typically contain impurities that lead to leakage current in transistor devices[19,20]. Furthermore, the dielectric constant of hBN ($k \simeq 4$) is comparable to that of SiO_2 ($k \simeq 3.9$), thus limiting the downscaling in vdW nanoelectronics[21]. Common deposition techniques used for SiO_2 and HfO_2 are not directly compatible with 2D materials[22,23]. In general, these methods tend to damage or modify the electronic properties of the underlying 2D crystal[24], especially when the 2D material is thinned to single- unit cell thickness. Other options include exploring atomically flat layered oxides such as mica or V_2O_5 and assembling them layer by layer. However, these dielectrics also result in a significant level of charge transfer to neighbouring 2D materials, large hysteresis in field-effect devices, and significant reduction of the mobility[25]. Therefore, the search for alternative dielectrics or novel technologies, compatible with 2D materials which give good interface quality and with high-k is needed.

In the published work, we demonstrated a route to embed ultrathin HfO_x in vdW heterostructures using selective photo-oxidation of HfS_2. As mentioned in section 3.1, HfS_2 is a layered semiconductor with an indirect bandgap of 2.85 eV in its bulk form[26–28] and has comparable surface roughness to other 2D crystals after exfoliation (for more information see the section for Atomic Force Microscopy (AFM) in the Supplementary Materials of the paper this chapter is based on). We found that the photo-oxidation process can be enabled using laser light even when the HfS_2 is embedded within complex heterostructures and under metallic contacts. This fabrica-

tion technique eliminates the need for invasive sputtering or Atomic Layer Deposition (ALD) methods[29]. Finally, we demonstrated that the photo-induced HfO_x has a dielectric constant $k \simeq 15$ and that this dielectric can be incorporated into four classes of devices enabling different applications: flexible FETs, resistive switching random access memories (ReRAMs), vertical light emitters, and photodetectors.

However, this chapter presents in greater detail the ReRAM devices, to which I have directly contributed with the fabrication of materials and structures. The rest of the results will be briefly presented for completeness purposes.

4.1 DEVICE FABRICATION

The devices presented in this chapter were fabricated using standard micromechanical exfoliation of bulk crystals and then by making use of a Polydimethylsiloxane (PDMS) stamp transfer technique[30] to form the heterostructures. Initially, graphene is mechanically exfoliated onto a thermally oxidized silicon wafer and appropriate flakes are chosen after optical inspection. After this, the HfS_2 flakes are exfoliated onto PDMS and transferred on the selected graphite flakes. The HfS_2 flakes are released from the PDMS between $50 - 60°C$. This process is then repeated for the subsequent layers of the device as required. Here, for fabricating the optoelectronic devices (Section 4.4) hBN is used as an atomically flat substrate on to which the subsequent flakes can be assembled. For devices on hBN substrates a PMMA membrane is used and the graphene is dry peeled from the PMMA onto the hBN[25,31].

Following heterostructure production, the contacts were structured using either optical or electron beam lithography, followed by thermal evaporation of Cr/Au (5/60 nm) electrodes. After assembling the heterostructure, photo-oxidation of the HfS_2 layer was performed by rastering either UV ($\lambda = 375\,\text{nm}$) or visible ($\lambda = 473\,\text{nm}$) laser light focused to a diffraction-limited spot in the custom-built setup described in Section 2.2.1.1. A typical energy density of $53\,\text{mJ}\,\mu\text{m}^{-2}$ was used for exposures lasting $1 - 2$s per point of the HfS_2 layer. The focused spot size was $d_s = 264\,\text{nm}$ for the UV laser and $d_s = 445\,\text{nm}$ for the visible wavelength.

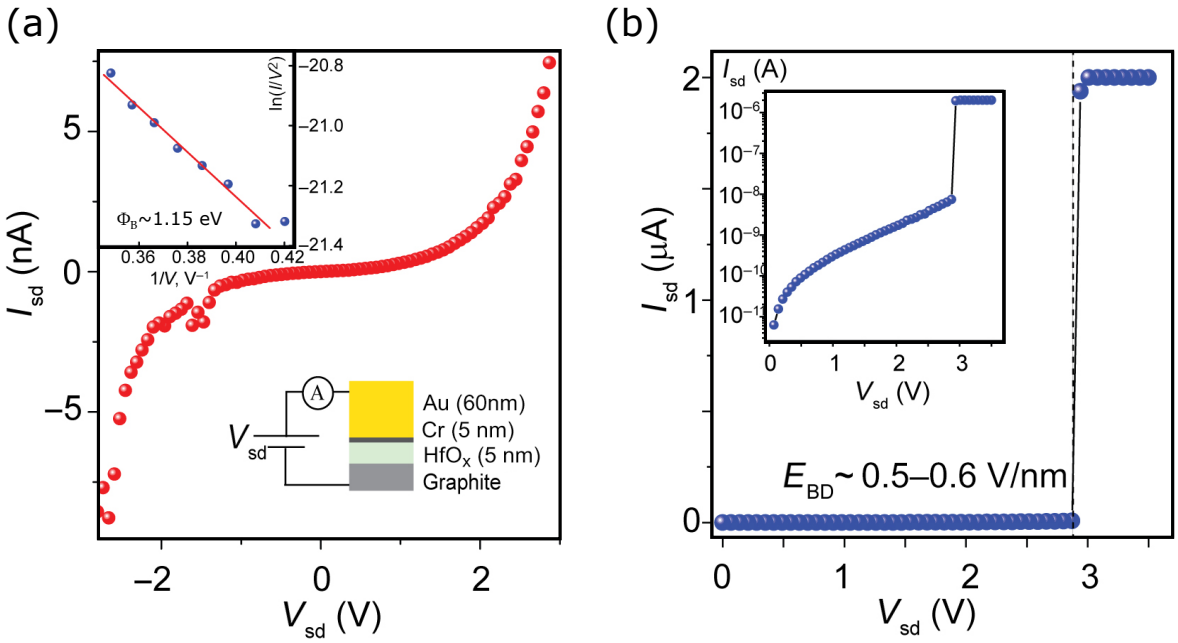

Figure 4.1: Breakdown of HfO_x dielectrics. (a) $I_{sd} - V_{sd}$ characteristics for a 5-nm graphite-HfO_x-Cr/Au junction. Top left inset: Fowler-Nordheim tunneling theory. Bottom right inset: Device schematic. (b) $I_{sd} - V_{sd}$ for an extended voltage range showing the breakdown field for the dielectric. Inset: Log scale plot of the same data showing the exponential dependence of tunneling current with bias voltage.

4.2 CHARACTERISATION OF HFO_2 INSULATING PROPERTIES

The characterization of dielectric properties such as the DC dielectric constant and the breakdown field has been conducted using a *Keithley 2400* voltage/current source meter. The electrical characterisation of graphene and TMD FETs was performed using standard low-noise AC lock-in techniques using a *Signal Recovery 7225* lock-in amplifier and a *Keithley 2400* source meter providing the gate voltage. All electrical transport measurements were performed either in a vacuum (10^{-3} mbar) or in helium atmosphere.

The breakdown voltage of the laser-written oxide was measured in a heterostructure consisting of graphite-HfO_x-Cr (5 nm)/Au (60 nm) as schematically shown in the inset of Figure 4.1 (a). Tunneling current can be measured when a source-drain bias is applied across the vertical junction, as shown in Figure 4.1 (a). The tunnel current

is found to increase exponentially until an electric field of $E_{BD} \simeq 0.5$ to $0.6\,\mathrm{V\,nm^{-1}}$ is applied, at which point the current discontinuously increases to the compliance level of the voltage source meter, as shown in Figure 4.1 (b). This breakdown field is comparable to that of SiO_2 and hBN (0.6 to 2.5 $\mathrm{V\,nm^{-1}}$ and 1 $\mathrm{V\,nm^{-1}}$, respectively)[32,33]. The tunnel current is well fit by the Fowler-Nordheim tunneling model (Figure 4.1 (a), inset). We were able to estimate the barrier height value of $\Phi_B \simeq 1.15\,\mathrm{eV}$[34]. This value is smaller than expected for a graphene-HfO_2 barrier $\Phi_B \simeq 1.78\,\mathrm{eV}$, likely related to the nonstoichiometry of the amorphous oxide and finite impurity content, leading to an impurity band forming below the conduction band edge.

Scaling of the tunnel conductivity with oxide thickness was found to be unreliable with thin oxides $d < 3\,\mathrm{nm}$ displaying significantly lower than expected resistivity ($\sim 10^6$ to $10^7\,\Omega\,\mu\mathrm{m}^2$), while oxides of thickness $d > 10\,\mathrm{nm}$ show similar resistivity to 5-nm-thick oxides ($\sim 10^{11}$ to $10^{12}\,\Omega\,\mu\mathrm{m}^2$). This can be explained as follows: in thin flakes, there is a higher chance for electrical pinholes caused by impurities or defects that shunt the current away from high-resistance paths, whereas thicker flakes do not fully oxidise for the same irradiation energy (which was kept constant in this work at $53\,\mathrm{mJ\,\mu m^{-2}}$ for exposures lasting 1 to 2 s per point of the HfS_2 layer), leading to higher than expected conductivity. Optimal thickness for uniform oxidation was found to be 4 to 8 nm. We expect that the oxide quality could easily be improved by optimising for laser excitation energy, excitation power, and laser spot dwell time during the writing procedure.

To better understand the dielectric properties of the laser-written HfO_x, we fabricated dual-gated graphene FETs. An optical micrograph of a FET constructed on a Si/SiO_2 (285 nm) substrate from a stack of bilayer graphene/HfO_x (7 nm) and Cr/Au contacts is shown in the inset of Figure 4.2 (a). The metal contacts are placed directly on the bilayer graphene (contacts 1, 2, and 11) and on top of the HfO_x (contacts 3 to 10). To form a contact between the top Cr/Au metal lead and the graphene underneath the HfO_x, we rely on the formation of a stable conductive filament produced by the intentional breakdown of the dielectric. In this way, we can use contacts 7 and 8 in the inset of Figure 4.2 (b) as source and voltage probes; contacts 9, 10, and 11 as drain and voltage probes, while the other metal leads (3 to 6 and 8) are used as top gates. The $I_{sd} - V_{sd}$ characteristics showing stable filament formation are shown in Figure 4.2 (a), where the red curve shows the initial dielectric breakdown at a vertical electric field of $\sim 0.5\mathrm{V\,nm^{-1}}$. Further cycling of the source-drain bias with increasing current

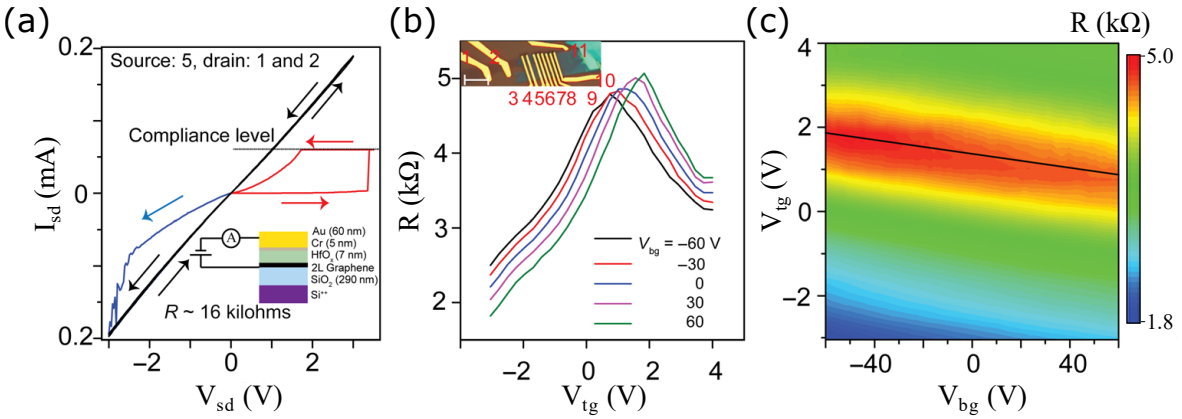

Figure 4.2: HfO_x as an electrical contact material and gate oxide in a dual-gated graphene FET. (a) V_{sd} indicating that the formation of a conductive filament in the oxide (red curve) further reduces resistance to the 10 kΩ level (blue and black curves). (b) R(V_{tg}) for different values of V_{bg} from -60 V to +60 V. Inset: Optical micrograph of the heterostructure device consisting of Gr-HfOx-Cr/Au. (c) Contour map of the channel resistance between contacts 8 and 10, with contact 9 acting as the top gate electrode.

compliance leads to stable non-reversible filament formation that allows for direct contact of the underlying graphene channel. Typical contact resistances of $\sim 5.5\,\mathrm{k\Omega}$ are achieved after filamentation (as the area of conductive filament is unknown, we cannot estimate the resistivity in this case). Back gate (SiO_2) sweeps of the resistance show the bilayer graphene to be heavily $p-$doped with the Charge Neutrality Point (CNP) lying at $V_{CNP} \sim 80$V. These $p-$type doping levels are attributed to the oxygen plasma cleaning of the Si-SiO_2 substrate, used to promote the adhesion of graphene before exfoliation.

Figure 4.2 (c) shows a four-terminal top gate – back gate contour plot of the four-point channel resistance between contacts 7 and 9 (contacted through filamentation), with contact 8 serving as the top gate electrode. From the slope of the neutrality point, dV_{tg}/dV_{bg}, and the thickness of the oxide (determined from the AFM data), we calculated the dielectric constant of the HfO_x material to be $k \sim 15 \pm 1$. This value is similar to literature values for amorphous HfO_x [35,36]. Therefore, having confirmed that the dielectric properties of our laser-written HfO_x are comparable to those of sputtered HfO_x films, we turned our attention to its implementation in electronic devices.

4.3 RESISTIVE SWITCHING MEMORY DEVICES

4.3.1 *Resistive Switching Mechanism*

The formation of conducting filaments illustrated in Figure 4.1 (b) allows for switching between two resistance states, creating a device known as resistive switching Random Access Memory ReRAM element[37–41]. ReRAM devices represent a promising emerging memory technology with several advantages over conventional technologies including increased speed, endurance, and device density.

A resistive switching Random Access Memories (ReRAM) element is a simple type of non-volatile memory device consisting of a dielectric layer sandwiched between two metallic electrodes, as shown in the left panel of Figure 4.3 (a). Initially, a ReRAM device is subjected to the operation of *electroforming*, or simply *forming*, which is a "soft" (i.e. reversible) breakdown of the dielectric due to the formation of a conductive filament between the top and bottom electrode (Figure 4.3 (a), middle panel). During electroforming, a voltage bias is applied between the top and bottom electrode and the current is limited by a compliance system, which allows the size of the contactive filament to be controlled and avoids the destructive (hard) breakdown of the switching layer.

Now, the system has two resistance states it can operate on; one where the top and bottom electrodes are connected with the conductive filament(s) and is known as the low-resistance state (LRS) and one where the conducting filament has been depleted of carriers and is known as the high-resistance state (HRS), as depicted in the right panel of Figure 4.3 (a). The mechanism of switching between the two resistance states is called *resistive switching*. It includes the process of switching from the HRS to the LRS, which is called *SET* process, and switching from the LRS to the HRS, which is called *RESET*.

The switching modes of metal–oxide ReRAM can be broadly classified into two switching modes: unipolar and bipolar[42]. Figures 4.3 (b),(c) show the I-V characteristics of the unipolar and bipolar modes respectively. In unipolar switching, as can be deduced from Figure 4.3 (b), the amplitude of the applied bias is responsible for the switching and not the polarity, thus SET/RESET occur in the same polarity. If the unipolar switching can symmetrically occur at both positive and negative voltages, it is also referred as a *non-polar* switching mode. On the other hand, in bipolar

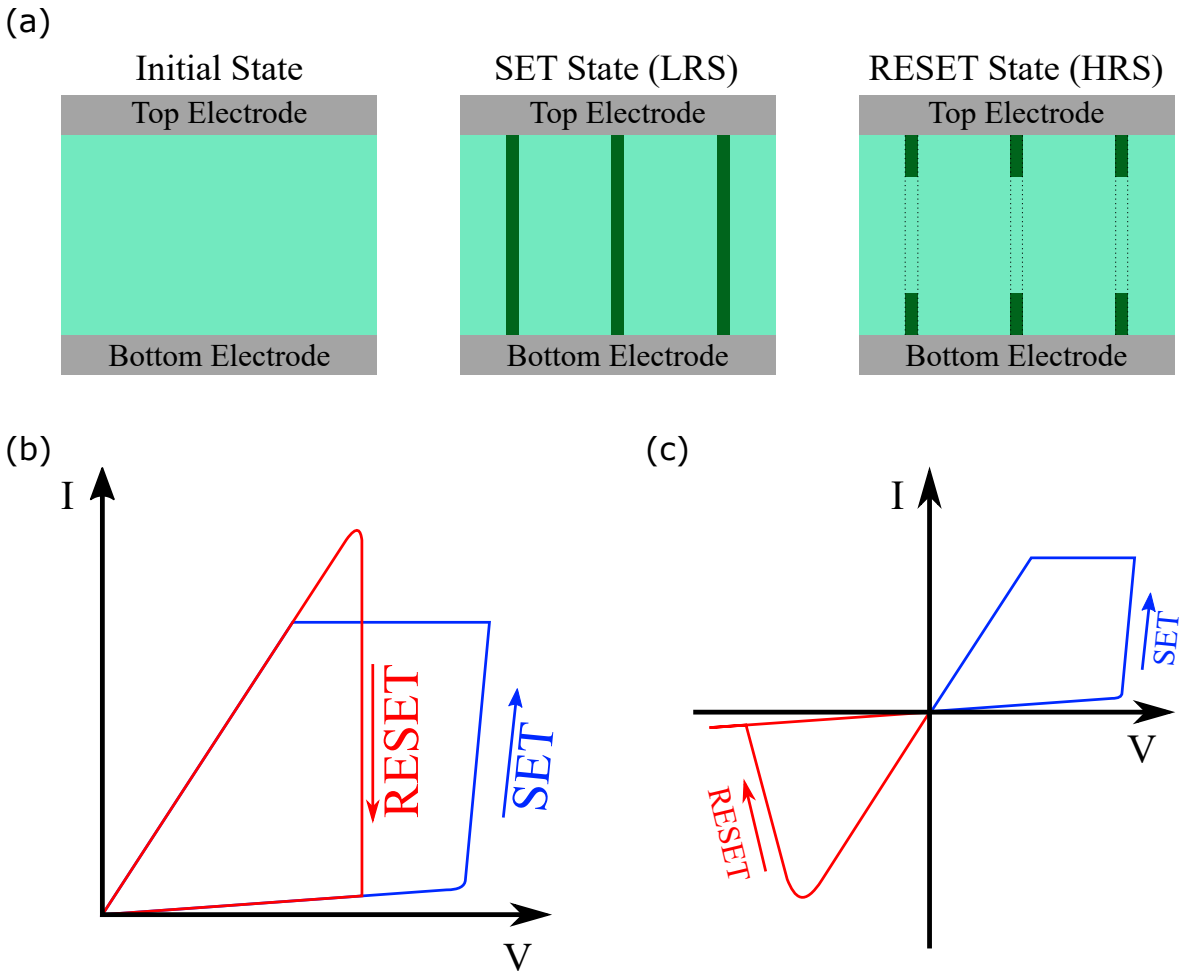

Figure 4.3: ReRAM operation. (a) Schematic of a ReRAM device (left panel). After electroforming, a conductive filament is formed connecting the top and the bottom electrode, thus resulting in the SET or low-resistance state (LRS) of the memory device (middle panel). (b) I-V characteristics of a unipolar switching mode. (c) I-V characteristics of a bipolar switching mode.

switching the switching direction depends on the polarity of the applied bias. As a result, SET and RESET processes only occur in different polarities. For both switching modes, the current is limited by a compliance system to avoid permanent dielectric breakdown[39–41].

4.3.2 *ReRAM Devices with HfO_x*

Amongst the range of materials that show resistive switching, transition metal oxides including HfO_x are of particular interest[43] owing to a range of unique properties such as high mechanical flexibility, reduced power consumption, and potential for high-density memory devices based on stacks of vdW heterostructures[44]. Figure 4.4 shows representative device characteristics for a typical resistive switching element based on photo-oxidised few-layer HfS_2. Our devices consist of a Au top electrode with either titanium or chromium used as an adhesion layer deposited on top of the HfS_2-graphite heterostructure (see Figure 4.4 (a), inset). Following photo-oxidation of the HfS_2, the device is subjected to repeated current-voltage sweeps, where the top metal electrode is voltage-biased with respect to the bottom graphite electrode. During the initial voltage sweeps, the current compliance and bias voltage are incrementally increased until stable and repeatable resistance cycling is achieved (increasing the current compliance and V_{bg} further will lead to non-reversible conductive filaments, as discussed in the previous section).

Figure 4.4 (a) shows a subsequent switching loop after the initial breakdown. At $V_{sd} = +1\text{V}$, an abrupt increase in current is observed as the device switches from a HRS to a LRS (SET process). The device maintains its LRS as the polarity is reversed and swept down to -1V, where a reduction in current for increasing negative voltage is observed, while the device switches back to the HRS (RESET process). The use of thin flakes allows for low-voltage operation, with the SET/RESET voltages around $|V_{sd}| \simeq 1\,\text{V}$. The memory window of devices measured here (R_{HRS}/R_{LRS}) varies from ~ 5 up to $\sim 10^4$, with the larger values observed for Au/Ti top electrodes. Figure 4.4 (b) shows similar current-voltage behaviour for the 1st and 100^{th} cycle. The results of repeated cycling are shown in Figure 4.4 (c) in which R_{HRS}/R_{LRS} (with both resistance values extracted at $V_{sd} = 100\,\text{mV}$) shows little variation over 100 cycles. Lastly, we investigated the long-term stability of this ReRAM device (Figure 4.4 (d)) and found

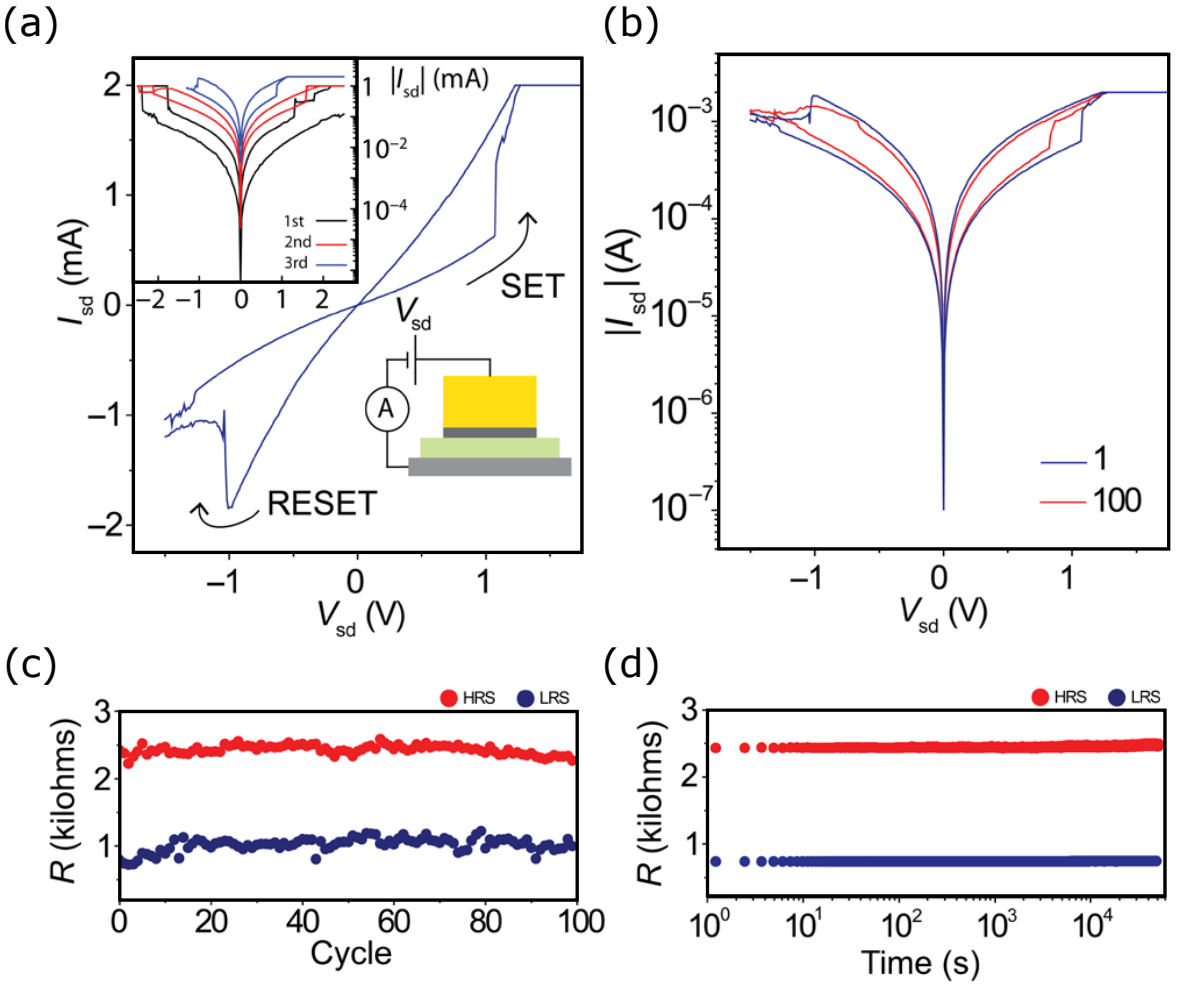

Figure 4.4: HfO_x as an electrical contact material and gate oxide in a dual-gated graphene FET. (a) Example of a switching cycle for the device architecture shown in the bottom right inset. Top left inset: Initial filament formation sweeps before repeatable switching was achieved. (b) First and 100^{th} switching cycle for the same device. (c) Resistance versus cycle number for the two resistance states plotted for the LRS (blue) and HRS (red). (d) Time stability for the two resistance states.

that the resistance levels measured for $V_{sd} = 250\,\mathrm{mV}$, were consistent and well defined for more than $10^4\,\mathrm{s}$.

We note that resistive switching in devices using graphene for both top and bottom electrodes was unreliable, suggesting that electrode material asymmetry is crucial for reliable device performance. This bipolar switching is consistent with the formation and rupture of conducting filaments. However, further studies are required to optimise device performance and to better understand the role played by disorder, oxide thickness, and contact chemistry.

4.4 OPTOELECTRONIC DEVICES

Vertically stacked heterostructures of 2D materials provide a framework for the creation of large-area, atomically thin and flexible optoelectronic devices such as photodetectors[11,13,45] and light-emitting diodes[9,10,46]. To date, only hBN tunnel barriers have been demonstrated; however, other wide-gap material oxides have not been explored when combined with vdW heterostructures. Here, we demonstrate the use of ultrathin HfO_x tunnel barriers in vertical light-emitting tunneling transistor device geometries.

Figure 4.5 (a) shows the current-voltage curve of a $HfOx_x$ single-quantum well (SQW) device formed by the encapsulation of monolayer MoS_2 in 1nm to 2nm of HfO_x. Applying a bias voltage between the top and bottom graphene electrodes (G_t and G_b) allows a current to tunnel through the thin HfO_x layers and into the MoS_2. As we increase the bias voltage from zero, the current increases nonlinearly. Outside of a low-bias regime ($|V_{sd}| > 1\mathrm{V}$), we observed an increase in the current due to tunneling into the conduction band of MoS_2. In addition, an asymmetry between the current at positive and negative bias voltage is observed, which is likely due to both a variation in doping between G_t and G_b and a different thickness of the top and bottom HfO_x. This behaviour is similar to previous work using hBN tunnel barriers[9].

The active area of the heterostructure was determined using scanning photocurrent microscopy, whereby a laser beam is rastered across the device while photocurrent is acquired simultaneously. Photocurrent measurements were performed using a continuous-wave laser ($\lambda_{in} = 514\,\mathrm{nm}, P = 15\,\mathrm{W\,cm^{-2}}$) rastered on the devices to produce spatial maps of the photoresponse. The electrical signal was acquired by a *DL Instruments model 1211* current amplifier connected to a *Signal Recovery model 7124*

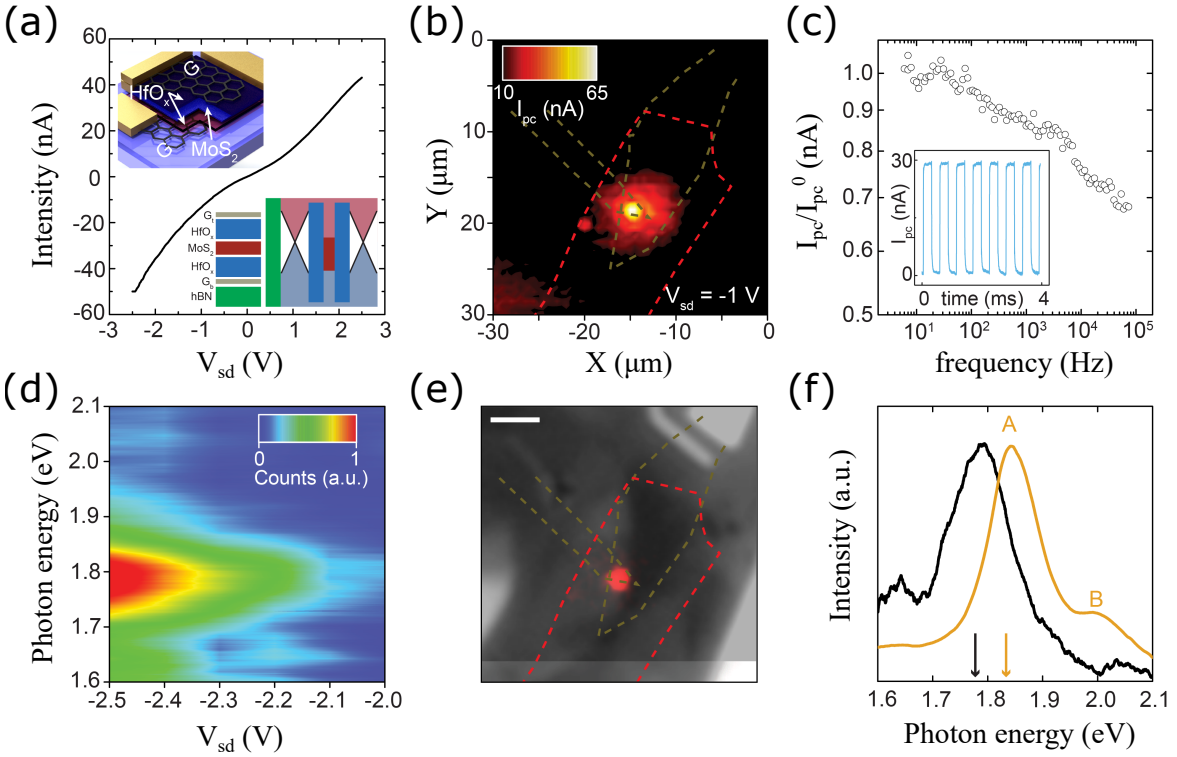

Figure 4.5: Thin HfO_x barriers for optoelectronic applications. (a) Current-voltage characteristics for the SQW. Insets: Device architecture (top) and schematic of the heterostructure band alignment (hBN-Gr_b-HfO_x-MoS_2-HfO_x-Gr_t) (bottom). (b) Scanning photocurrent map acquired with a bias of $V_{sd} = -1$V applied between the top and bottom graphene electrodes. The red dashed lines correspond to the MoS_2 flake, while the grey ones to the graphene electrodes. (c) Normalised photocurrent as a function of modulation frequency. Inset: The temporal response of the photocurrent at $f = 1.8$ kHz. (d) Color map of the EL spectra as a function of V_{sd}. (e) False-color charge-coupled device image of the EL overlaid on an optical image of the device. Scale bar, 5 µm. (f) Comparison between the normalised intensities of the EL (black) and PL (brown) acquired at $V_{sd} = -2.5$ V and $V_{sd} = 0$ V, respectively.

digital signal processing lock-in amplifier. The lasers were modulated by using an external function generator at a frequency of $f_0 = 73.87\,\mathrm{Hz}$. The laser modulation works as a mechanical chopper, operating at a frequency F_0, and along with the detection of the produced signal by the current amplifier (lock-in frequency set also at f_0) allows the measurement of small electrical signals, for example, in samples with a low responsivity and high dark current. The description of the characterisation setup can be found in Chapter 2.2.1.1.

Figure 4.5 (b) shows that, under a moderate bias ($V_{sd} = -1\mathrm{V}$), the photocurrent is predominately localised to regions of overlap between the top and bottom graphene flakes, each outlined in light green. Photoexcited carriers in MoS_2 (red outline) are separated by the graphene electrodes because of the applied vertical electric field. Away from this region, the photocurrent (I_{pc}) drops from > 65 to $< 10\,\mathrm{nA}$. As shown in Figure 4.5 (c), we measured a reduction in the magnitude of the photocurrent as we increased the light modulation frequency. For this device, the -3-dB bandwidth was found to be $f_{-3dB} = 40\,\mathrm{kHz}$ and the rise time $t_r = 0.35/f_{-3dB} \sim 8.8\,\mu\mathrm{s}$. The inset of Figure 4.5 (c) shows multiple iterations of the photocurrent obtained at 1.8 kHz. The measured response time is 10^3 to 10^6 times faster than that of typical planar MoS_2 photodetectors[47]; a result arising from the use of a vertical, as opposed to lateral, contact geometry. The small electrode separation of $\sim 6\,\mathrm{nm}$ and large electric fields of ~ 0.1 to $0.2\,\mathrm{V\,nm^{-1}}$ minimise the transit time of the photoexcited carriers. Hence, these vertical heterostructures of MoS_2 encapsulated in HfO_x are a promising high-speed light-detection architecture.

As the bias voltage is further increased, the quasi–Fermi levels of the graphene electrodes allow for simultaneous injection of electrons into the conduction band of MoS_2 and holes into the valence band. The carrier confinement set by the HfO_x tunnel barriers allows for exciton formation in the MoS_2. The subsequent decay of those excitons leads to light emission at the excitonic gap of MoS_2. Figure 4.5 (d) shows the electroluminescence (EL) intensity map as a function of photon energy and bias voltage, where the main EL band appears at 1.78 eV.

Electroluminescence is only observed for $V_{sd} < -2\mathrm{V}$, with a more intense signal recorded by increasing $|V_{sd}|$. The emergence of EL at $-2\,V$ corresponds well with the single-particle bandgap of monolayer MoS_2[48,49] while the negative threshold voltage can be attributed to the asymmetric device structure.

Figure 4.5 (e) shows a false-color Charge-Coupled Device (CCD) image of the EL overlaid on a monochrome image of the device at an applied bias voltage of -2.5 V. The EL is localised to the active area of the device previously identified in Figure 4.5 (b) through photocurrent mapping. To further understand the emission, normalised EL and photoluminescence (PL) spectra are shown in Figure 4.5 (f). The main PL emission peak is assigned to the A exciton seen at an energy of 1.8 eV. The energy of the main EL band red-shifts from that of PL by 53 meV. Typically, the exfoliated monolayer MoS_2 is $n-$doped, which favours the formation of negatively charged excitons [50], which have $\sim$ 30 meV lower emission energy than neutral exciton. Therefore, we attributed the main feature in EL spectra at 1.78 eV to the radiative recombination of the charged exciton. Moreover, the dissociation energy (i.e. energy shift referring to that of neutral exciton) of the charged exciton is proportional to the doping concentration [50]. Therefore, it is likely that the large energy difference between EL and PL is an indication of high doping in monolayer MoS_2, which is due to doping of the as-exfoliated natural MoS_2 flakes.

4.5 SUMMARY AND OUTLOOK

In this chapter the results of the characterisation of photo-oxidised HfS_2 as a dielectric layer for vdW heterostructures were presented, along with memory and opotoelectronic devices that incorporate the photo-induced HfO_x. We showed that ultrathin few-layer HfS_2 can be incorporated into a variety of vdW heterostructures and selectively transformed into an amorphous high-k oxide using laser irradiation.

In contrast to sputtering or ALD, the use of photo-oxidised HfS_2 allows for clean interfaces without damaging the underlying 2D materials. We demonstrated that the laser-written HfO_x has a dielectric constant $k \sim 15$ and a breakdown field of ~ 0.5 to $0.6\,\mathrm{V\,nm^{-1}}$. These properties allow us to demonstrate several promising high-quality vdW heterostructure devices using this oxide: (i) ReRAM elements that operate in the voltage limit of ~ 1 V; and (ii) optoelectronic devices based on quantum well architectures, which can emit and detect light in the same device, with EL intensities and drive voltages comparable to devices with hBN barriers and photodetection response times up to 10^6 times faster than equivalent planar MoS_2 devices. Moreover, the high-k dielectric constant, the compatibility with 2D materials, and the ease of

laser-writing techniques[51] will allow for significant scaling improvements and greater device functionality, which we predict to be an important feature for future flexible semi-transparent vdW nanoelectronics.

However, especially for the case of memory devices, further studies are required in order to optimise device performance and to better understand the role played by disorder, oxide thickness, and contact chemistry, as mentioned in section 4.3.2. Regarding the optoelectronic devices, future research should focus on increasing the quantum efficiency both of photodetection and of electroluminescence. In this direction, replacing monolayer MoS_2 with a multilayer direct band gap material or stacking multiple HfO_x encapsulated monolayers could be the main paths to follow.

BIBLIOGRAPHY

[1] A. I. Kingon, J.-P. Maria, and S. K. Streiffer. Alternative dielectrics to silicon dioxide for memory and logic devices. *Nature*, 406(6799):1032–1038, aug 2000.

[2] M. J. Mleczko, C. Zhang, H. R. Lee, H.-H. Kuo, B. Magyari-Köpe, R. G. Moore, Z.-X. Shen, I. R. Fisher, Y. Nishi, and E. Pop. $Hfse_2$ and $zrse_2$: Two-dimensional semiconductors with native high-k oxides. *Science Advances*, 3(8), aug 2017.

[3] B. Chamlagain, Q. Cui, S. Paudel, M. M.-C. Cheng, P.-Y. Chen, and Z. Zhou. Thermally oxidized 2d tas_2 as a high-k gate dielectric for mos_2 field-effect transistors. *2D Materials*, 4(3):031002, jun 2017.

[4] S. J. Cartamil-Bueno, P. G. Steeneken, F. D. Tichelaar, E. Navarro-Moratalla, W. J. Venstra, R. van Leeuwen, E. Coronado, H. S. J. van der Zant, G. A. Steele, and A. Castellanos-Gomez. High-quality-factor tantalum oxide nanomechanical resonators by laser oxidation of $tase_2$. *Nano Research*, 8(9):2842–2849, jul 2015.

[5] A. K. Geim and I. V. Grigorieva. Van der waals heterostructures. *Nature*, 499(7459):419–425, jul 2013.

[6] P. Miró, M. Audiffred, and T. Heine. An atlas of two-dimensional materials. *Chem. Soc. Rev.*, 43(18):6537–6554, 2014.

[7] L. Britnell, R. V. Gorbachev, R. Jalil, B. D. Belle, F. Schedin, A. Mishchenko, T. Georgiou, M. I. Katsnelson, L. Eaves, S. V. Morozov, N. M. R. Peres, J. Leist, A. K. Geim, K. S. Novoselov, and L. A. Ponomarenko. Field-effect tunneling transistor based on vertical graphene heterostructures. *Science*, 335(6071):947–950, feb 2012.

[8] A. Mishchenko, J. S. Tu, Y. Cao, R. V. Gorbachev, J. R. Wallbank, M. T. Greenaway, V. E. Morozov, S. V. Morozov, M. J. Zhu, S. L. Wong, F. Withers, C. R. Woods, Y-J. Kim, K. Watanabe, T. Taniguchi, E. E. Vdovin, O. Makarovsky, T. M. Fromhold, V. I. Fal'ko, A. K. Geim, L. Eaves, and K. S. Novoselov. Twist-controlled resonant tunnelling in graphene/boron nitride/graphene heterostructures. *Nature Nanotechnology*, 9(10):808–813, sep 2014.

[9] F. Withers, O. Del Pozo-Zamudio, A. Mishchenko, A. P. Rooney, A. Gholinia, K. Watanabe, T. Taniguchi, S. J. Haigh, A. K. Geim, A. I. Tartakovskii, and K. S. Novoselov. Light-emitting diodes by band-structure engineering in van der waals heterostructures. *Nature Materials*, 14(3):301–306, feb 2015.

[10] F. Withers, O. Del Pozo-Zamudio, S. Schwarz, S. Dufferwiel, P. M. Walker, T. Godde, A. P. Rooney, A. Gholinia, C. R. Woods, P. Blake, S. J. Haigh, K. Watanabe, T. Taniguchi, I. L. Aleiner, A. K. Geim, V. I. Fal'ko, A. I. Tartakovskii, and K. S. Novoselov. Wse_2 light-emitting tunneling transistors with enhanced brightness at room temperature. *Nano Letters*, 15(12):8223–8228, nov 2015.

[11] L. Britnell, R. M. Ribeiro, A. Eckmann, R. Jalil, B. D. Belle, A. Mishchenko, Y.-J. Kim, R. V. Gorbachev, T. Georgiou, S. V. Morozov, A. N. Grigorenko, A. K. Geim, C. Casiraghi, A. H. Castro Neto, and K. S. Novoselov. Strong light-matter interactions in heterostructures of atomically thin films. *Science*, 340(6138):1311–1314, jun 2013.

[12] J. D. Mehew, S. Unal, E. T. Alonso, G. F. Jones, S. F. Ramadhan, M. F. Craciun, and S. Russo. Fast and highly sensitive ionic-polymer-gated ws_2 -graphene photodetectors. *Advanced Materials*, 29(23):1700222, apr 2017.

[13] M. M. Furchi, A. Pospischil, F. Libisch, J. Burgdörfer, and T. Mueller. Photovoltaic effect in an electrically tunable van der waals heterojunction. *Nano Letters*, 14(8):4785–4791, jul 2014.

[14] C.-H. Lee, G.-H. Lee, A. M. van der Zande, W. Chen, Y. Li, M. Han, X. Cui, G. Arefe, C. Nuckolls, T. F. Heinz, J. Guo, J. Hone, and P. Kim. Atomically thin p-n junctions with van der waals heterointerfaces. *Nature Nanotechnology*, 9(9):676–681, aug 2014.

[15] F. Withers, H. Yang, L. Britnell, A. P. Rooney, E. Lewis, A. Felten, C. R. Woods, V. Sanchez Romaguera, T. Georgiou, A. Eckmann, Y. J. Kim, S. G. Yeates, S. J. Haigh, A. K. Geim, K. S. Novoselov, and C. Casiraghi. Heterostructures produced from nanosheet-based inks. *Nano Letters*, 14(7):3987–3992, jun 2014.

[16] D. McManus, S. Vranic, F. Withers, V. Sanchez-Romaguera, M. Macucci, H. Yang, R. Sorrentino, K. Parvez, S.-K. Son, G. Iannaccone, K. Kostarelos, G. Fiori, and C. Casiraghi. Water-based and biocompatible 2d crystal inks for all-inkjet-printed heterostructures. *Nature Nanotechnology*, 12(4):343–350, jan 2017.

[17] S. Bertolazzi, D. Krasnozhon, and A. Kis. Nonvolatile memory cells based on mos_2/graphene heterostructures. *ACS Nano*, 7(4):3246–3252, mar 2013.

[18] C. R. Dean, A. F. Young, I. Meric, C. Lee, L. Wang, S. Sorgenfrei, K. Watanabe, T. Taniguchi, P. Kim, K. L. Shepard, and J. Hone. Boron nitride substrates for high-quality graphene electronics. *Nature Nanotechnology*, 5(10):722–726, aug 2010.

[19] M. Venkata Kamalakar, André Dankert, Paul J. Kelly, and Saroj P. Dash. Inversion of spin signal and spin filtering in ferromagnet—hexagonal boron nitride-graphene van der waals heterostructures. *Scientific Reports*, 6(1), feb 2016.

[20] M. Gurram, S. Omar, S. Zihlmann, P. Makk, Q. C. Li, Y. F. Zhang, C. Schönenberger, and B. J. van Wees. Spin transport in two-layer-CVD-hBN/graphene/hBN heterostructures. *Physical Review B*, 97(4):045411, jan 2018.

[21] G. D. Wilk, R. M. Wallace, and J. M. Anthony. High-k gate dielectrics: Current status and materials properties considerations. *Journal of Applied Physics*, 89(10):5243–5275, may 2001.

[22] H. G. Kim and H.-B.-R. Lee. Atomic layer deposition on 2d materials. *Chemistry of Materials*, 29(9):3809–3826, apr 2017.

[23] S. McDonnell, B. Brennan, A. Azcatl, N. Lu, H. Dong, C. Buie, J. Kim, C. L. Hinkle, M. J. Kim, and R. M. Wallace. Hfo_2 on mos_2 by atomic layer deposition: Adsorption mechanisms and thickness scalability. *ACS Nano*, 7(11):10354–10361, oct 2013.

[24] M. Xiao, C. Qiu, Z. Zhang, and L.-M. Peng. Atomic-layer-deposition growth of an ultrathin hfo_2 film on graphene. *ACS Applied Materials & Interfaces*, 9(39):34050–34056, sep 2017.

[25] A. V. Kretinin, Y. Cao, J. S. Tu, G. L. Yu, R. Jalil, K. S. Novoselov, S. J. Haigh, A. Gholinia, A. Mishchenko, M. Lozada, T. Georgiou, C. R. Woods, F. Withers, P. Blake, G. Eda, A. Wirsig, C. Hucho, K. Watanabe, T. Taniguchi, A. K. Geim, and R. V. Gorbachev. Electronic properties of

graphene encapsulated with different two-dimensional atomic crystals. *Nano Letters*, 14(6):3270–3276, may 2014.

[26] C. Gong, H. Zhang, W. Wang, L. Colombo, R. M. Wallace, and K. Cho. Band alignment of two-dimensional transition metal dichalcogenides: Application in tunnel field effect transistors. *Applied Physics Letters*, 103(5):053513, jul 2013.

[27] M. Traving, T. Seydel, L. Kipp, M. Skibowski, F. Starrost, E. E. Krasovskii, A. Perlov, and W. Schattke. Combined photoemission and inverse photoemission study of hfs_2. *Physical Review B*, 63(3):035107, jan 2001.

[28] C. Kreis, S. Werth, R. Adelung, L. Kipp, M. Skibowski, E. E. Krasovskii, and W. Schattke. Valence and conduction band states of hfs_2: From bulk to a single layer. *Physical Review B*, 68(23):235331, dec 2003.

[29] X. Tang, N. Reckinger, O. Poncelet, P. Louette, F. Ureña, H. Idrissi, S. Turner, D. Cabosart, J.-F. Colomer, J.-P. Raskin, B. Hackens, and L. A. Francis. Damage evaluation in graphene underlying atomic layer deposition dielectrics. *Scientific Reports*, 5(1), aug 2015.

[30] A. Castellanos-Gomez, M. Buscema, R. Molenaar, V. Singh, L. Janssen, H. S. J. van der Zant, and G. A. Steele. Deterministic transfer of two-dimensional materials by all-dry viscoelastic stamping. *2D Materials*, 1(1):011002, apr 2014.

[31] L. Wang, I. Meric, P. Y. Huang, Q. Gao, Y. Gao, H. Tran, T. Taniguchi, K. Watanabe, L. M. Campos, D. A. Muller, J. Guo, P. Kim, J. Hone, K. L. Shepard, and C. R. Dean. One-dimensional electrical contact to a two-dimensional material. *Science*, 342(6158):614–617, nov 2013.

[32] Y. Hattori, T. Taniguchi, K. Watanabe, and K. Nagashio. Layer-by-layer dielectric breakdown of hexagonal boron nitride. *ACS Nano*, 9(1):916–921, dec 2014.

[33] E. Harari. Conduction and trapping of electrons in highly stressed ultrathin films of thermal sio_2. *Applied Physics Letters*, 30(11):601–603, jun 1977.

[34] W.J. Zhu, T.-P. Ma, T. Tamagawa, J. Kim, and Y. Di. Current transport in metal/hafnium oxide/silicon structure. *IEEE Electron Device Letters*, 23(2):97–99, feb 2002.

[35] F. Choy. Characterization of hafnium oxide thin films prepared by mocvd. In *AIP Conference Proceedings*. AIP, 2003.

[36] M. Osada and T. Sasaki. Two-dimensional dielectric nanosheets: Novel nanoelectronics from nanocrystal building blocks. *Advanced Materials*, 24(2):210–228, oct 2011.

[37] D. Ielmini. Resistive switching memories based on metal oxides: mechanisms, reliability and scaling. *Semiconductor Science and Technology*, 31(6):063002, may 2016.

[38] D.-H. Kwon, K. M. Kim, J. H. Jang, J. M. Jeon, M. H. Lee, G. H. Kim, X.-S. Li, G.-S. Park, B. Lee, S. Han, M. Kim, and C. S. Hwang. Atomic structure of conducting nanofilaments in tio_2 resistive switching memory. *Nature Nanotechnology*, 5(2):148–153, jan 2010.

[39] R. Waser and M. Aono. Nanoionics-based resistive switching memories. *Nature Materials*, 6(11):833–840, nov 2007.

[40] X. Guan, S. Yu, and H.-S. P. Wong. On the switching parameter variation of metal-oxide RRAM

- part i: Physical modeling and simulation methodology. *IEEE Transactions on Electron Devices*, 59(4):1172–1182, apr 2012.

[41] M. K. F. Lee, Y. Cui, T. Somu, T. Luo, J. Z., W. T. Tang, W.-F. Wong, and R. S. M. Goh. A system-level simulator for RRAM-based neuromorphic computing chips. *ACM Transactions on Architecture and Code Optimization*, 15(4):1–24, dec 2018.

[42] H.-S. Philip Wong, H.-Y. Lee, S. Yu, Y.-S. Chen, Y. Wu, P.-S. Chen, B. Lee, F. T. Chen, and M.-J. Tsai. Metal–oxide RRAM. *Proceedings of the IEEE*, 100(6):1951–1970, jun 2012.

[43] S. Yu, H.-Y. Chen, B. Gao, J. Kang, and H.-S. Philip Wong. $Hfox_x$-based vertical resistive switching random access memory suitable for bit-cost-effective three-dimensional cross-point architecture. *ACS Nano*, 7(3):2320–2325, feb 2013.

[44] S. Lee, J. Sohn, Z. Jiang, H.-Y. Chen, and H.-S. P. Wong. Metal oxide-resistive memory using graphene-edge electrodes. *Nature Communications*, 6(1), sep 2015.

[45] M. Massicotte, P. Schmidt, F. Vialla, K. G. Schädler, A. Reserbat-Plantey, K. Watanabe, T. Taniguchi, K. J. Tielrooij, and F. H. L. Koppens. Picosecond photoresponse in van der waals heterostructures. *Nature Nanotechnology*, 11(1):42–46, oct 2015.

[46] J. Binder, F. Withers, M. R. Molas, . Faugeras, K. Nogajewski, K. Watanabe, T. Taniguchi, A. Kozikov, A. K. Geim, K. S. Novoselov, and M. Potemski. Sub-bandgap voltage electroluminescence and magneto-oscillations in a WSe2 light-emitting van der waals heterostructure. *Nano Letters*, 17(3):1425–1430, feb 2017.

[47] D. Kufer and G. Konstantatos. Highly sensitive, encapsulated mos_2 photodetector with gate controllable gain and speed. *Nano Letters*, 15(11):7307–7313, nov 2015.

[48] K. F. Mak, C. Lee, J. Hone, J. Shan, and T. F. Heinz. Atomically thin mos_2: A new direct-gap semiconductor. *Physical Review Letters*, 105(13):136805, sep 2010.

[49] C. Zhang, A. Johnson, C.-L. Hsu, L.-J. Li, and C.-K. Shih. Direct imaging of band profile in single layer mos_2 on graphite: Quasiparticle energy gap, metallic edge states, and edge band bending. *Nano Letters*, 14(5):2443–2447, may 2014.

[50] K. F. Mak, K. He, C. Lee, G. H. Lee, J. Hone, T. F. Heinz, and J. Shan. Tightly bound trions in monolayer mos_2. *Nature Materials*, 12(3):207–211, dec 2012.

[51] A. De Sanctis, G. F. Jones, D. J. Wehenkel, F. Bezares, F. H. L. Koppens, M. F. Craciun, and S. Russo. Extraordinary linear dynamic range in laser-defined functionalized graphene photodetectors. *Science Advances*, 3(5), may 2017.

5

HIGH MOBILITY IN N-DOPED CVD-GROWN WSE_2 FETS

NOTE: The ideas and data presented in this chapter have been the subject of the following publication (currently under review): *Synthesis of monolayer n-doped WSe_2 from solid state inorganic precursors.* Nanomaterials, under review (2022). M. Och, K. A. Anastasiou, I. Leontis, G. Z. Zemignani, P. Palczynski, A. Mostaed, M. Sokolikova, E. M. Alexeev, A. I. Tartakovskii, J. Lischner, P. Nellist, S. Russo, and C. Mattevi.

In this publication, my contribution was in the fabrication and optoelectronic characterisation of the devices.

INTRODUCTION

The family of TMDs has attracted an increasing interest in the last decade due to their unique optical, electrical and catalytic properties that enable potentially appealing applications[1,2]. Within this large family of materials, monolayer WSe_2 has emerged as an ideal material due to its direct optical bandgap close to the near infra-red region (1.65 eV)[3,4], a large charge carrier mobility[5] and a robust valley-spin degree of freedom[6]. WSe_2 crystallises in the thermodynamically stable hexagonal (2H) crystal phase, or it can be stabilised in the distorted trigonal (1T') phase. In the 1T' phase it exhibits properties of a 2D topological insulator[7], and has been reported to be an active catalyst for the electrocatalytic hydrogen evolution[8]. Furthermore, for the 2H-WSe_2, promising applications have been reported especially in the areas of photovoltaics[9,10], spintronics[11,12], and optoelectronics[13–16]. Additionally, WSe_2 and

TMDs in general are emerging as potentially transformative materials for the future generation of ultra-short channel field effect transistors (FETs) as the charge carriers are confined within the layer and uniformly controlled by the gate voltage[17,18].

An industrially scalable synthesis method is Chemical Vapour Deposition (CVD), which is also the most promising technique that can achieve high quality crystal growth over wafer scale for mass production[19,20], as already demonstrated for III-V semiconductors. To date, monolayer WSe_2 has been synthesised in a form of isolated domains by CVD[21,22], and as large-scale continuous films using Metal-Organic Chemical Vapor Deposition (MOCVD)[23].

In this chapter, we demonstrate the optoelectronic properties of n-type WSe_2 which was synthesised using a novel CVD method and resulted in n-type transport. The novelty relies in the use of the inorganic compound ZnSe as Selenium precursor, which does not require using H_2 as reducing agent or gaseous H_2Se. The obtained triangular monolayer domains extend over tens of micrometres in lateral size, and they exhibit n-type transport, which can be attributed to donor states induced by the deposition of Zn on the surface of the crystal.

The material exhibits electron mobilities of $\sim 10\,\mathrm{cm^2\,V^{-1}\,s^{-1}}$ and hole mobilities up to $50\,\mathrm{cm^2\,V^{-1}\,s^{-1}}$, extrapolated from the transfer curves on fabricated Field Effect Transistor (FET)s. Moreover, the material possesses high intrinsic crystalline quality as demonstrated by the narrow linewidth of the room temperature photoluminescence (PL), while the low temperature emission is dominated by localised emitters due to strong interaction between the crystal and the growth substrate.

After a brief presentation of the synthesis process in the first section of this chapter, an in-depth analysis of the optoelectronic characterisation will follow.

5.1 SYNTHESIS OF MONOLAYER N-DOPED WSE_2

The novel CVD synthesis method for WSe_2 presented in this section was developed by the group of Dr. C. Mattevi at Imperial College London. This method is promising for industrially scalable synthesis of high-quality WSe_2 crystal, while it is also a first step into the control of the charge carrier type and density in it. The latter is of paramount importance for the implementation of WSe_2 in the metal-oxide semiconductor (MOS)FET architecture and complementary metal-oxide semiconductor (CMOS)

logic controlling[24,25].

This would require the doping to be air stable, covalent and controllable at the synthesis level. However, substitutional doping of WSe_2 is still in early research stages, and only a few examples are reported in literature[25–29]. Whilst substitutional *p*-doping of monolayer WSe_2 has been achieved via CVD[30,31], substitutional *n*-doped WSe_2 can only be obtained for bulk crystals via chemical vapour transport[32].

Until now, a large amount of H_2 is used as reducing agent in the growth process, as it increases the reactivity of both metal and halcogen precursors and it has been proven to be fundamental for enabling the growth of WSe_2 from Se powder[33]. However, handling and storing H_2 can be problematic in terms of safety, as it is highly flammable, while H_2Se presents acute toxicity at extremely low exposure concentration. By using ZnSe as selenium precursor the usage of H_2 is not required, which makes the handling process easier and safer. In addition, it leads to the formation of large area monolayer flakes, as shown in Figure 5.1 (a), which are *n*-doped due to the deposition of Zn atoms on the surface of the material as shown in Transmission Electron Microscopy (TEM) images (Figure 5.1 (c),(d)).

The growth was performed in a single-zone tubular furnace sublimating a 50% wt. mixture of H_2WO_4-NaCl along with ZnSe powder loaded in two different alumina crucibles placed next to each other and heated at $825-850\,°C$ at low pressure (approximately $0.1-1\,mbar$) using argon as carrier gas. The target substrate for the WSe_2 synthesis was SiO_2/Si as this is inexpensive and technologically relevant for future scalability of the synthesis. In addition, it gave the best results in terms of thickness control, crystal size and homogeneity in the used system.

As shown in Figure 5.1 (a), the optical examination along with AFM measurements showed that a lateral flake size in the order of tens of μm was achieved ($\sim$ 10-50 µm) with a thickness of $\sim 1\,nm$, which is the expected height of a monolayer on a rough substrate such as silica[21,34]. These lateral dimensions of the WSe_2 triangles are in line with the reported sizes of the majority of CVD-grown monolayers[35–37]. Furthermore, it was found that by increasing the temperature to $850\,°C$ larger and thicker flakes were synthesised.

The critical role played by the new Se precursor, introduced in this novel synthesis approach, can be understood by using different Se-containing inorganic precursors. Alongside ZnSe, the group of Dr. C. Mattevi at Imperial College London, who studied

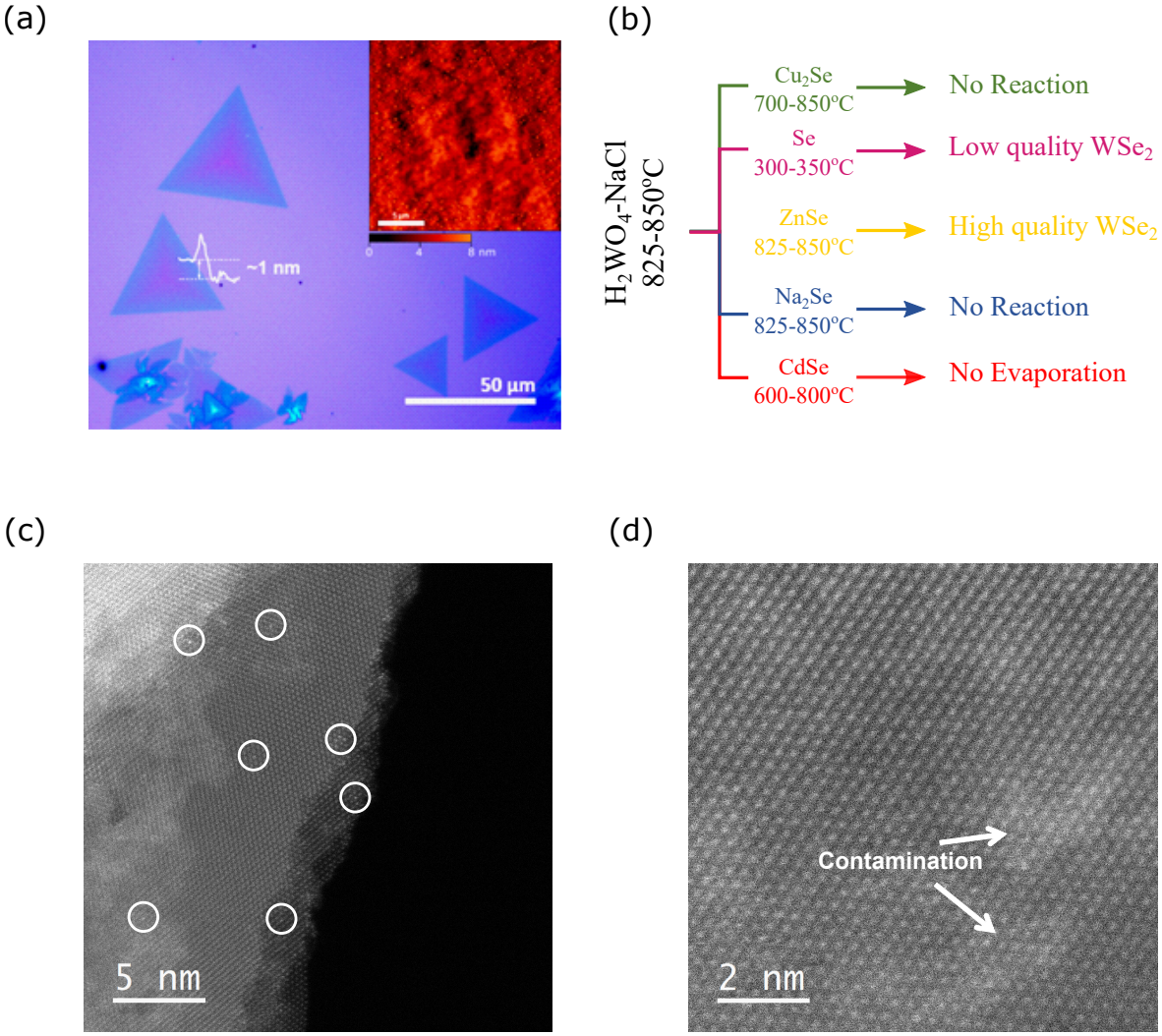

Figure 5.1: Optical and TEM images of CVD-grown WSe_2. (a) Optical micrograph of CVD grown monolayer Zn-doped WSe_2 alongside the thickness measured by AFM. Inset: AFM topographic map of a monolayer flake. (b) Diagram summarising the different Se precursors used in this study with the relative evaporation temperatures and outcome. (c),(d) TEM images of synthesised WSe_2 flakes. The occasional anomalous bright contrast of the W sites is attributed to the presence of extra W and/or Zn atoms on either side of the flake (i.e. adatoms) (c). Islands of contamination which probably contain Zn atoms are observed on the WSe_2 surface. This leads to additional Zn-doping of the flakes.

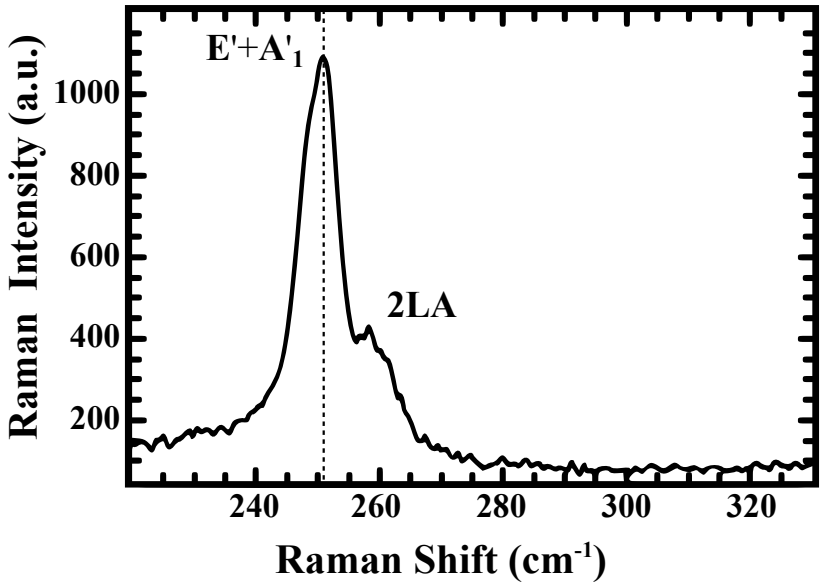

Figure 5.2: Raman spectrum of CVD-grown WSe_2. Typical Raman spectrum (λ = 514 nm) of an as-grown WSe_2 monolayer after PMMA-transfer on target SiO_2. The principal $E^{'}+A_1^{'}$ and 2LA peaks are indicated.

and developed the growth process, tested different Se precursor powders (Cu_2Se, Se-powder, Na_2Se and CdSe) under different temperature conditions. The findings are summarised in Figure 5.1 (b), where it is shown that the highest quality of WSe_2 crystal was obtained while using ZnSe as precursor.

5.1.1 *Raman characterisation of CVD-grown WSe_2 monolayer*

Raman spectroscopy was utilised to investigate the quality of the crystal as it is a non-destructive technique which gives valuable information of the crystal structure and thickness. A representative Raman spectrum of a synthesised WSe_2 flake taken in ambient conditions using 514 nm excitation wavelength at the microscope setup described in Section 2.2.1.1 is presented in Figure 5.2. The dominant peak at 251.8 cm^{-1} is given by the convolution of the first order $E^{'}$ in-plane and $A_1^{'}$ out-of-plane vibrational modes, while the weaker second-order $2LA(M)$ mode is visible at 258.3 cm^{-1}, is close to its expected value of 260 cm^{-1} for monolayer WSe_2 [38–40]. The proximity to the expected position of the $2LA$ peak, along with the absence of the B_{2g}^1 mode at 310 cm^{-1} confirms

the monolayer nature of the flake[38,39], while simultaneously implies the existence of defects.

5.2 FABRICATION OF WSe_2 FIELD-EFFECT TRANSISTORS

In order to probe the optoelectronics properties of the CVD-grown WSe_2 we fabricated FETs with Ti/Au and Zn/Au contacts.

Initially, wet-etching was used to detach the material from the target Si substrate. The donor substrates were spin-coated with a thin ($\sim$ 150 nm) layer of Poly(methyl 2-methylpropenoate) (PMMA) and baked at 150 °C for 2 minutes before they were put in a potassium hydroxide (KOH) solution ($C = 8.9\,M$, $pH \sim 13$) at 70 °C until the entire surface layer of Si was removed. This process leaves the PMMA layer with the attached material floating on the surface of the dilution and is then scooped and transferred into clean de-ionised (DI) water several times to minimise the KOH residues on the flakes which can affect the target substrate. Subsequently, the clean PMMA layer was scooped with a clean Si^{++}/SiO_2 substrate and left on a hot-plate at 50 °C for at least four hours to dry. Finally, it goes through a thorough acetone - DI water - Propan-2-ol (IPA) cleaning to remove the PMMA and other residues from the flake.

The Field Effect Transistors were fabricated using standard electron-beam lithography and thermal deposition of Ti/Au (5/60 nm) or Zn/Au (20/40 nm) for the contacts followed by lift-off in acetone.

5.2.1 *Aims of the study and device geometry*

Various device geometries were fabricated with the aim to characterize the doping, the free charge carrier density, type and mobility as well as the contact resistance at the metal/WSe_2 interface. As discussed in section 2.2.2.1, at the interface of a semiconductor and a metal, an energy barrier is created (*Schottky barrier*), thus affecting the performance of electronic devices. The Transfer Length Method (TLM) is utilised to characterise the contact resistance at the metal/WSe_2 interface. This consists of multiple two-terminal electrical measurements taken between pairs of subsequent metal contacts with varying length of the semiconducting channel (see analysis in section 2.2.2.1 and Eq. 2.19). A measurement of the 2-terminal resistance will contain the WSe_2 resistance as well as twice the metal/WSe_2 contact resistance. The channel

resistance is expected to scale linearly with the geometrical length of the semiconducting channel. Therefore, in a plot of the total resistance as a function of the channel length, the intercept for channel length equal to zero is equal to two times the contact resistance. This value of resistance can be subtracted from the value of the total two terminal resistance measured in field-effect transistors, enabling a more accurate estimate of the charge carrier mobility.

An alternative method for the direct measurement and characterisation of the intrinsic transport properties of the channel and, therefore, the mobility of the charge carriers as well, is the *four-terminal method* (also discussed in Section 2.2.2.1). In this case, the resistance of the semiconducting channel is directly calculated using Eq. (2.20), where V_{probes} and d_{probes} are the voltage difference and the distance between the voltage probes, respectively.

Another aim of this study was to confirm the free charge carrier density and its field effect dependence. This is achieved with *Hall effect* measurements, as described in Section 2.3. During Hall measurements, the device is kept at cryogenic temperatures, leaving no thermally excited carriers inside the channel that can modify the carrier density and type. Due to the existence of magnetic field vertical to the flow of carriers, those are accumulated on the edges of the channel, depending on their charge (positive and negative charges occupy opposite edges). This gives rise to an electrical field that applies force to the moving charges, opposite to that applied of the magnetic field. When the two forces become exactly opposite, equilibrium is reached and the carriers flow in straight line between the source and drain electrodes. By depositing two metal probes vertical to the channel, we can calculate the density of free carriers according to Eq. (2.23).

In order to address these questions, we have fabricated field-effect transistors on p-doped Si/SiO_2 substrates with multi-terminal Hall bar structures and performed scaling transport experiments.

Finally, as moisture can be trapped at the interface of the semiconductor and the deposited contacts during fabrication, thermal annealing under vacuum can be used to remove it and improve the behaviour of the devices. Thus, by measuring the devices before and after thermal annealing we can explore the functional dependence of the aforementioned quantities on crystal quality, fabrication conditions and unwanted contamination.

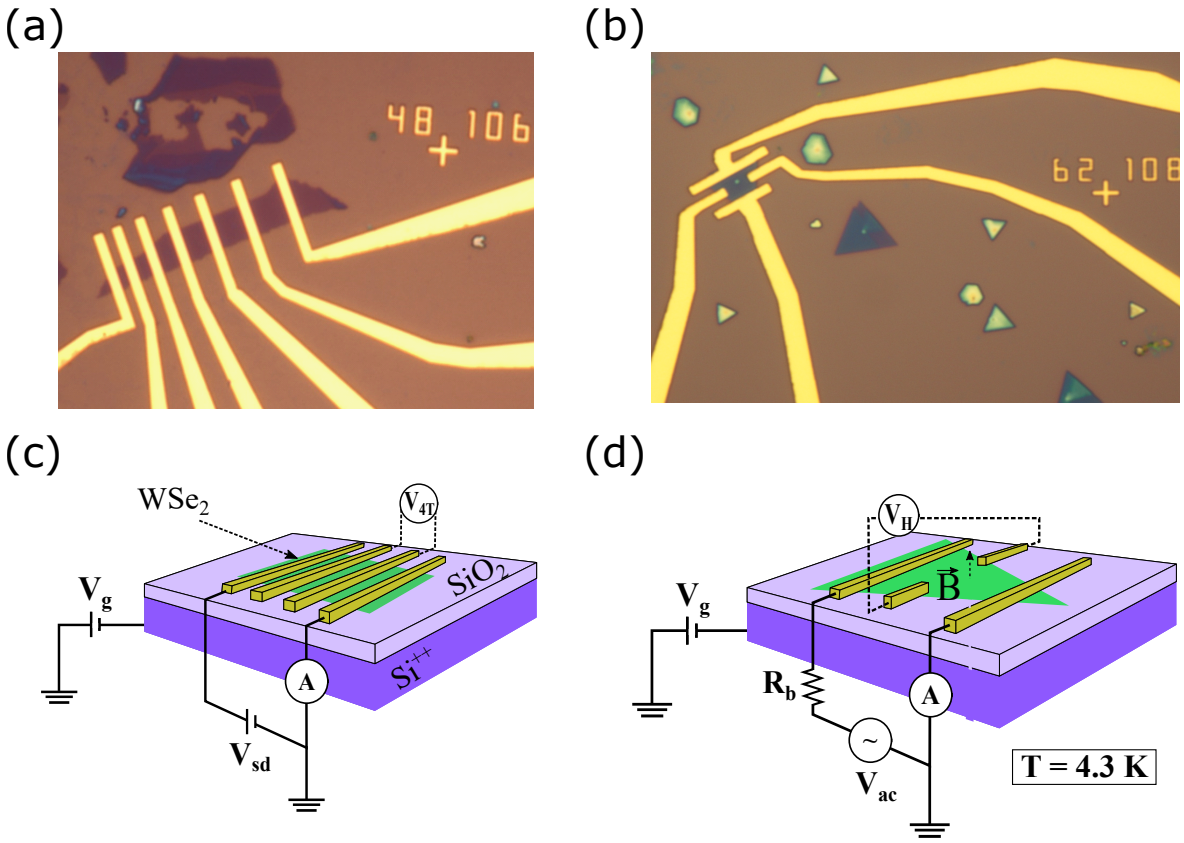

Figure 5.3: Geometries and electrical circuits of studied devices. (a) TLM geometry for studying the electric transport properties of the material. Multiple contacts at different separations are ideal to find the channel's resistivity with TLM. As a reference, the length of the cross marker is 3 µm. (b) Standard geometry for studying the doping of the material using Hall measurements. Hall probes are overlapping with the WSe_2 flake for 1 µm. As a reference, the length of the cross marker is 3 µm. (c) Schematic of the electrical circuit for the two- and four-terminal (dashed line) field-effect measurements of the material. (d) Schematic of the electrical circuit used for Hall measurements. During the measurements the sample was kept at a temperature of 4.3 K.

In Figure 5.3 (a), (b) the main types of the fabricated geometries are shown. Since there are many parameters that can not be controlled during the growth and the transfer of the material, the final shape of the flake is not exactly the same for all the formed flakes. In this case, it resulted in two main shapes we mainly chose to work with; relatively rectangular pieces that were formed after the destruction of triangular flakes (Figure 5.3 (a)) and normal triangular flakes (Figure 5.3 (b)). The former gave us the opportunity to deposit multiple metal contacts over a long area while the change of the geometry of the channel was minimal.

With the contact configuration shown in Figure 5.3 (a), we were able to perform multi-terminal measurements and use Transfer Length Method (TLM) (see Section 2.2.2.1) to determine the contact resistance and to probe directly the resistivity of WSe_2 and the charge carrier mobility. The measurements were taken using the circuit of (Figure 5.3 (c)), where the two- and four-terminal output of the device was monitored.

Furthermore, we selected flakes with triangular shape for the fabrication of multi-terminal Hall-bars (Section 2.3 (b)). As can be seen in the two panels of Figure 5.3 (b), the voltage probes that measure the induced bias perpendicular to the flow of carriers do not overlap with the flake more than 1 µm. By minimising the overlap of the voltage probes with the semiconducting channel, we secure a non-invasive role of these contacts on the flow of current. In Figure 5.3 (d), the corresponding circuit for Hall measurements is shown.

5.3 CHARACTERISATION OF CVD-GROWN WSE_2

5.3.1 *Optoelectronic characterisation*

To ascertain the doping and electrical transport properties of the CVD-grown WSe_2, we fabricated FETs with Ti/Au and Zn/Au contacts. The devices were characterised in vacuum (1×10^{-5} mbar) prior to and after multiple annealing steps aimed at reducing unwanted contamination of the system incurred in the fabrication. For the optoelectronic characterisation of all the devices presented here, the custom-made setup described in Section 2.2.1.2 was used.

Figure 5.4 (a) shows the transfer characteristics of a representative device before and after different annealing conditions, which were measured using the circuit shown in Figure 5.3 (c). Such a comparative plot shows a change of conductive charge types from

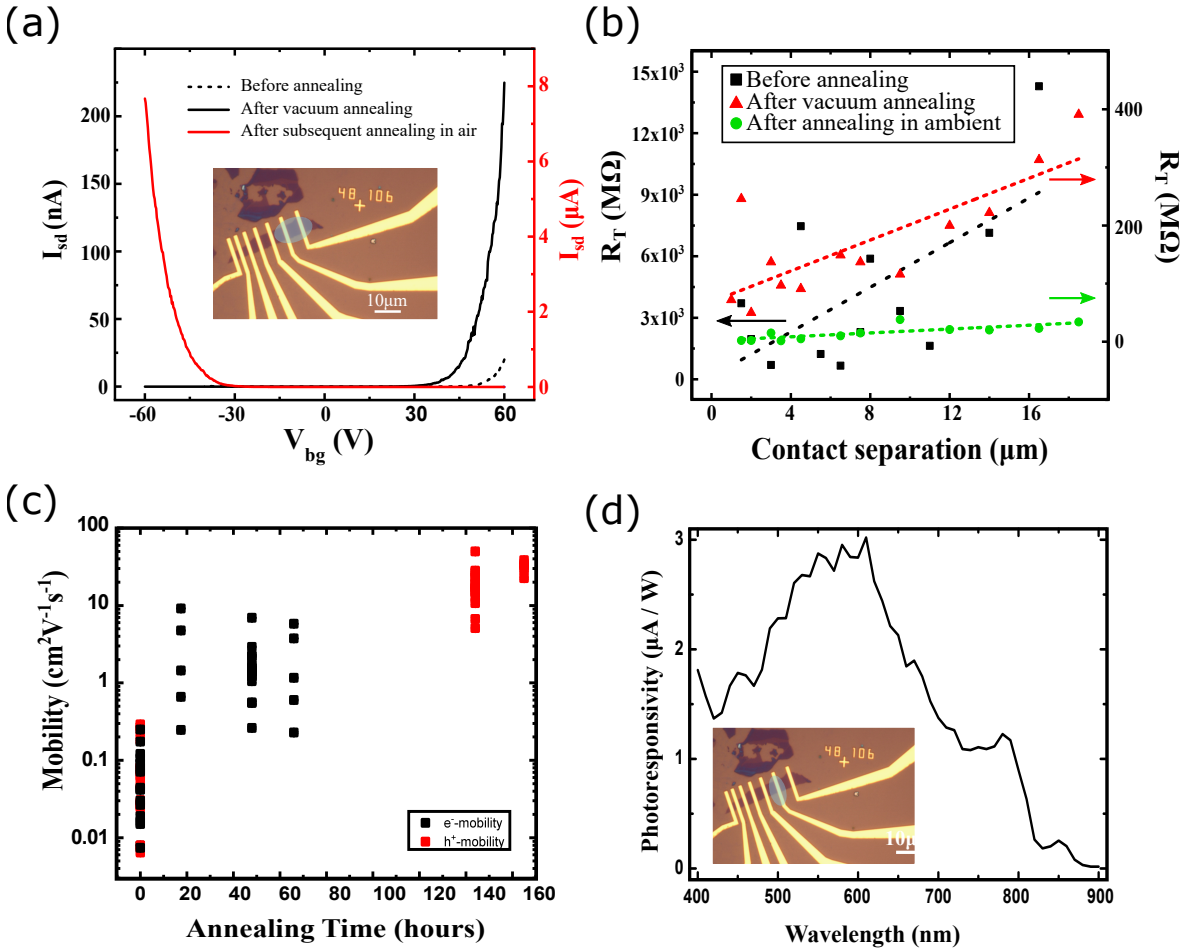

Figure 5.4: Optoelectronic characterisation of WSe_2 FET. (a) Transfer curves of WSe_2 FET (inset) under source-drain bias of $V_{sd} = 1\,V$ (before, after an initial vacuum annealing step and after annealing in ambient conditions). (b) Contact resistance determination for the FET in panel (a), using TLM. (c) Effect of annealing on the mobility of two different devices; one with Ti/Au contacts and one with Zn/Au (panel (a), inset) contacts. (d) Spectral response of device under source and gate bias $V_{sd} = 3\,V$ and $V_{bg} = -50\,V$, respectively.

electrons (before annealing and after vacuum annealing) to holes after air annealing. At the same time, the source-drain current increases upon annealing attaining an ON/OFF ratio of $\sim 10^5$.

Transfer Length Method (TLM) was used after each annealing step to examine the effects of the annealing on the semiconductor. By performing a linear fit to the Ohmic region of the transfer curve of each contact pair (two-terminal configuration), the total resistance (R_{tot}) can be calculated according to Ohm's law

$$R_{tot} = \frac{V_{bg}}{I_{sd}}\,, \tag{5.1}$$

where V_{bg} is the applied bias to the gate and I_{sd} the measured current between the source and drain electrodes of the device.

The results are summarised in Figure 5.4 (b), where the contact resistance (R_c) is extracted before annealing, after vacuum annealing and after subsequent annealing in ambient conditions. The contact resistance (R_c) is extracted by considering the intercept of the linear fit to the R_{tot} data, as described in Section 2.2.2.1 by Equation 2.19

$$R_T = 2R_C + \rho_s \frac{d}{W} \overset{d\to 0}{\Longrightarrow} R_T = 2R_C,$$

where d is the separation of the contacts.

From the data presented in Figure 5.4 (b), it is suggested that thermal annealing reduces the effect of contacts on the transport characteristics of the material and enhances the output of the devices. Specifically, the value of the contact resistance drops from $\sim 205\,\mathrm{M\Omega\,\mu m^{-1}}$ before any annealing, to $105\,\mathrm{M\Omega\,\mu m^{-1}}$ after the vacuum annealing cycles to reach a minimum of $\sim 3\,\mathrm{M\Omega\,\mu m^{-1}}$ after the completion of ambient annealing cycles.

The significant enhancement of the transport characteristics due to the reduction of contact resistance is reflected in the charge carrier mobility ($\mu_i\,,\ i = e^-, h^+$). Following the discussion in Section 1.1.3, the field-effect mobility of the charge carriers can be extracted from either the two- or the four-terminal measured transfer characteristics of a FET using the Drude model ($\sigma_i = n_i q_e \mu_i\ ,\ i = e^-, h^+$), where q_e is the elementary charge, σ_i is the conductivity of the channel and n_i is the induced carrier concentration due to the applied back-gate bias (V_g). The conductivity of the channel

and concentration of the carriers are given by

$$\sigma_i = \alpha q_e \mu_i V_g \quad and \quad n_i = \alpha V_g \,, \quad i = e^-, h^+ \,,$$

where $\alpha = 7.698 \times 10^{10}\,\mathrm{cm^{-2}\,V^{-1}}$ for SiO_2 gate dielectric of 280 nm thickness.

In Figure 5.4 (c), the field-effect mobility values of all the measured devices before and after each annealing cycle are shown. Before annealing, the values of mobility are quite low, not exceeding $0.4\,\mathrm{cm^2\,V^{-1}\,s^{-1}}$. However, as we showed, annealing of the devices enhances their transport characteristics and the charge carrier mobility increases reaching values as large as $10\,\mathrm{cm^2\,V^{-1}\,s^{-1}}$ (vacuum annealing) and $50\,\mathrm{cm^2\,V^{-1}\,s^{-1}}$ (annealing in air).

The improvement of the mobility values and the pure n-type conduction observed after vacuum annealing can be attributed to the reduction of concentration of surface contaminants. These were initially deposited on the surface of the channel as well as at the interface of the channel and the metal contacts. Furthermore, the change of carrier type from n- to p-type upon annealing in ambient is consistent with previous studies on annealing of WSe_2 in the presence of oxygen reporting an increase in hole doping due to the substitution of Se with O[41–44], as described in more detail in the next section.

Finally, we characterised the spectral response of the WSe_2 transistor under a source-drain bias of $V_{sd} = 1\,\mathrm{V}$ and with a gate bias of $V_{bg} = -50\,\mathrm{V}$ (Figure 5.4 (d)). We observed a maximum of photoresponsivity at 610 nm, which corresponds to an energy gap of $E_g \sim 2\,\mathrm{eV}$ in agreement with the theoretical values predicted from the Mott-Wannier exciton model for monolayer WSe_2 on a SiO_2 substrate[45].

5.3.2 *Enhancement of transport properties with annealing*

After the initial characterisation of the optoelectronic properties of the devices, in-situ annealing was conducted by heating the transistors at a temperature of 200 °C maintaining a background pressure of $\sim 10^{-5}$ mbar. Vacuum annealing is an effective method to reduce the concentration of surface contaminants by removing absorbed moisture and solvent molecules[46–48]. In addition, it has been shown to improve the contact adhesion[49] and lower the contact resistance[50]. The results of our characteri-

sation, presented in the previous section, confirm this enhancement of the conductivity of the channel as the devices after vacuum annealing show higher currents and carrier mobility.

To further enhance the device output and test the limitations of the WSe_2 FETs, long annealing was performed at a temperature of 200°C in ambient conditions. Generally, enhancement of the device characteristics due to heavy oxygen doping is observed under ambient annealing[41–44]. This is attributed to the substitution of Se_2 atoms with O_3 and the formation of WO_3, which is highly conductive, islets within the crystal of WSe_2. As a result of the work function difference between WO_3 and WSe_2, the latter is p-doped by the introduction of WO_3 within its crystallic structure and the hole concentration in the device is increased. These in-plane WSe_2-WO_3 heterojunctions formed by the heating of the devices in ambient conditions are responsible for the enhancement of the device characteristics.

5.3.3 *Hall Effect Measurements*

To confirm the free carrier type and concentration, we have characterised the back gate dependence of the Hall coefficient using a 4-terminal Hall bar configuration in a number of as-grown Zn-doped WSe_2 samples (see Figure 5.5 (b)) using a constant current bias of 16µA and perpendicular magnetic field $-2\text{T} \leq B \leq 2\text{T}$. For the characterisation, the sample was mounted on the cryogenic experimental setup described in Section 2.3.2, and was kept at a temperature of 4.3 K for the duration of the experiments.

By performing a sweep of the applied magnetic field while monitoring the induced Hall voltage, V_{Hall}, we can extract the free carrier concentration using Equation 2.24

$$n_{2D} = \frac{I/|q|}{dV_H/dB}\,.$$

As it is clear from the above equation, by performing a linear fit on the data collected while sweeping the magnetic field, we can calculate the charge carriers concentration and type from the slope of the fitted line. This process is shown in Figure 5.5 (a), where the concentration of free carriers has been extracted for $V_{bg} = 80\,\text{V}$ (red data points and fitted line) and for $V_{bg} = 45\,\text{V}$ (black data points and fitted line). For 80 V back-gate bias, the carriers concentration was found to be approximately $6.1\times10^{16}\,\text{m}^{-2}$, while for 45 V back-gate bias $\sim 1.1 \times 10^{16}\,\text{m}^{-2}$. It can be seen that the variance of

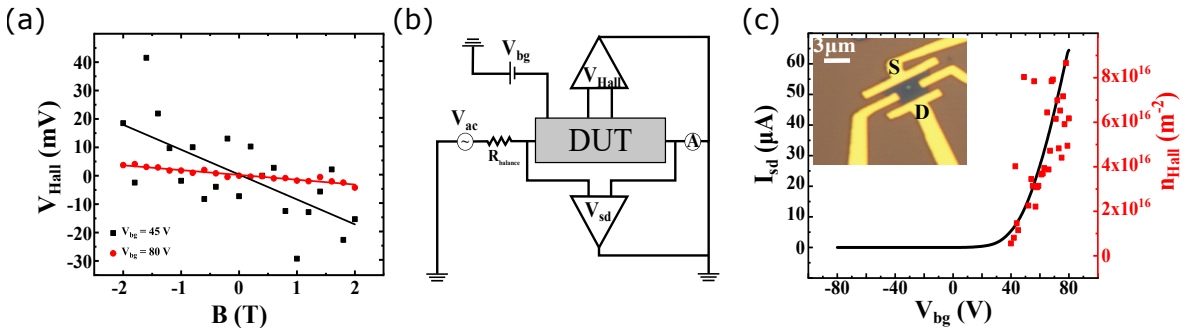

Figure 5.5: Hall effect measurements of WSe_2 FET. (a) Magnetic field sweeps and measured Hall voltage under different back-gate bias of the WSe_2 FET. The continuous lines represent the best linear fits of the data. The slope of the fitted line is used for the calculation of the carrier concentration inside the 2D channel (N_{2D}). (b) Electrical circuit used for the measurements of the tested device (Device Under Test, DUT). (c) Transfer characteristic (black curve, $V_{sd} = 2\,\mathrm{V}$) and gate-dependent Hall free carrier density (red data) measured for a representative Zn-doped Hall bar device (inset). All measurements were performed at $T = 4.3\,\mathrm{K}$.

the data points in reference to the regression line in the case of $V_{bg} = 45\,\mathrm{V}$ is quite high and can be attributed to high resistivity of the channel, implying the existence of many defects.

In Figure 5.5 (c), the extracted values of the concentration of the free charge carriers is plotted along the low-temperature transfer curve of the device, measured between the source and drain electrodes (Figure 5.5 (b)). By extrapolating the linear region of the transfer characteristic curve (black curve in Figure Figure 5.5 (c)) we can calculate the threshold voltage (V_T) of the device. For $V_{bg} \geq V_T$, there is a significant current flow from the source to the drain, meaning that the channel is sufficiently enriched with carriers. The transfer curve shows a threshold voltage of 48.3 V, which justifies the lower values of carrier concentration for sub-threshold gate biases.

These measurements confirm an average intrinsic n-type doping charge density $n_{Hall} > 5 \times 10^{15}\,\mathrm{m}^{-2}$ at the back gate threshold voltage, whereas no valence band conduction was observed. Specifically, the above value was measured at $V_{bg} = 40$volt. Furthermore, the free carrier density increases linearly with the back-gate voltage following the expected functional dependence of the Drude conductivity, $\sigma_e = n_e q_e \mu_e$.

These findings are consistent with the transfer characteristics showing n-type conduction.

Performing Hall measurements on pristine WSe_2 crystals grown using Se powder instead of ZnSe, we observed a much larger resistivity which hindered the performance of electrical measurements, suggesting the material is ambipolar. The aim was to extract the value of free carrier concentration and compare it with the one we extracted for the WSe_2 crystal which was grown with ZnSe powder as precursor. Ideally, the results would clearly show an intrinsic p-type in contrast with the ZnSe-grown material. Although the examined samples did not lead to the determination of the concentration of carriers due to high resistivity, there were indications from the data collected during the sweeps of the magnetic field that the material is ambipolar. This further supports our evidence that the Zn atoms induce n-type doping to WSe_2.

5.4 SUMMARY AND OUTLOOK

In this chapter we presented high-quality n-doped WSe_2 monolayers, grown using a novel inorganic precursor of selenium via CVD. The material exhibits n-type of doping which is further supported by Hall measurements. However, due to the high resistivity of the examined samples, only Hall measurements at back gate voltages comparable to the threshold voltage ($V_T = 48.3$V) of the devices were possible. Thus, we were able to calculate a lower limit for the free electron limit, which is $5 \times 10^{15}\,\mathrm{m}^{-2}$ at $V_{bg} = 40$V.

This n-type of doping can partially be attributed to the presence of adsorbed Zn atoms on the material, but still the majority of the doping is due to the field effect (see Equation 1.15). The doping is very stable, and the material exhibits electron mobilities up to $10\,\mathrm{cm}^2\,\mathrm{V}^{-1}\,\mathrm{s}^{-1}$, making the material viable for electronic devices. Nevertheless, more effort is needed in order to achieve Hall measurements at $V_{bg} = 0$V, which will accurately show the intrinsic doping of the material. Only then a safe conclusion for the role of adsorbed Zn atoms can be reached.

Additionally, we examined a potential way to change the transport properties of the material and enhance the field-effect mobility by annealing the devices in ambient. We showed that mobility is improved almost five times for the ambient-annealed devices, reaching hole mobilities up to $50\,\mathrm{cm}^2\,\mathrm{V}^{-1}\,\mathrm{s}^{-1}$. Although these values of mobility fall short of previously reported ones[5,15,51–53], we need to emphasise that in almost all the

cases we found the reported values were for hole but not for electron mobilility. The data presented here show among the highest n-type mobilities reported for monolayer WSe_2 FETs.

This work will contribute towards the implementation of air stable doping in TMDs and to ultimately achieve high-performance electronic and optoelectronic devices. As the doping occurs during the synthesis itself, it is compatible with large scale synthesis of TMDs.

In summary, more work is needed to obtain cleaner material and probably investigate whether the Zn atoms which are responsible for the n-doping of the material can be incorporated in its crystallic structure. Different fabrication approaches and vacuum annealing parameters need to be tested in order to end up with clean material and interfaces which will allow more precise Hall measurements. Furthermore, different types of devices should be tested in order to fully understand the material; mainly heterostructures were the CVD-grown WSe_2 is encapsulated in hBN or HfO_2 which will remove the effect of the anomalous SiO_2 surface. This, along with using graphene electrodes, thus eliminating the effect of metal contacts on the semiconducting channel, would make it easier to investigate the actual limitations of the material, in terms of its transport properties.

BIBLIOGRAPHY

[1] M. Chhowalla, H. S. Shin, G. Eda, L. J. Li, K. P. Loh, and H. Zhang. The chemistry of two-dimensional layered transition metal dichalcogenide nanosheets. *Nature Chemistry*, 5(4):263–275, mar 2013.

[2] Q. H. Wang, K. Kalantar-Zadeh, A. Kis, J. N. Coleman, and M. S. Strano. Electronics and optoelectronics of two-dimensional transition metal dichalcogenides. *Nature Nanotechnology*, 7(11):699–712, nov 2012.

[3] S. Mouri, Y. Miyauchi, M. Toh, W. Zhao, G. Eda, and K. Matsuda. Nonlinear photoluminescence in atomically thin layered wse_2 arising from diffusion-assisted exciton-exciton annihilation. *Physical Review B*, 90(15):155449, oct 2014.

[4] W. Zhao, Z. Ghorannevis, L. Chu, M. Toh, C. Kloc, P. H. Tan, and G. Eda. Evolution of electronic structure in atomically thin sheets of ws_2 and wse_2. *ACS Nano*, 7(1):791–797, dec 2012.

[5] A. Allain and A. Kis. Electron and hole mobilities in single-layer wse_2. *ACS Nano*, 8(7):7180–7185, jun 2014.

[6] Z. Wang, J. Shan, and K. F. Mak. Valley- and spin-polarized landau levels in monolayer wse_2. *Nature Nanotechnology*, 12(2):144–149, oct 2016.

[7] Z. Pedramrazi, C. Herbig, A. Pulkin, S. Tang, M. Phillips, D. Wong, H. Ryu, M. Pizzochero, Y. Chen, F. Wang, E. J. Mele, Z. X. Shen, S. K. Mo, O. V. Yazyev, and M. F. Crommie. Manipulating topological domain boundaries in the single-layer quantum spin hall insulator 1t'-wse_2. *Nano Letters*, 19(8):5634–5639, jul 2019.

[8] Q. Sun, Y. Dai, C. Niu, Y. Ma, W. Wei, L. Yu, and B. Huang. Lateral topological crystalline insulator heterostructure. *2D Materials*, 4(2):025038, feb 2017.

[9] N. Flöry, A. Jain, P. Bharadwaj, M. Parzefall, T. Taniguchi, K. Watanabe, and L. Novotny. A $wse_2/mose_2$ heterostructure photovoltaic device. *Applied Physics Letters*, 107(12):123106, sep 2015.

[10] S. Ko, J. Na, Y. S. Moon, U. Zschieschang, R. Acharya, H. Klauk, G. T. Kim, M. Burghard, and K. Kern. Few-layer wse_2 schottky junction-based photovoltaic devices through site-selective dual doping. *ACS Applied Materials & Interfaces*, 9(49):42912–42918, dec 2017.

[11] H. Yuan, X. Wang, B. Lian, H. Zhang, X. Fang, B. Shen, G. Xu, Y. Xu, S. C. Zhang, H. Y. Hwang, and Y. Cui. Generation and electric control of spin-valley-coupled circular photogalvanic current in wse_2. *Nature Nanotechnology*, 9(10):851–857, sep 2014.

[12] C. Jin, J. Kim, M. I. B. Utama, E. C. Regan, H. K., . Cai, Y. Shen, M. J. Shinner, A. Sengupta, K. Watanabe, T. Taniguchi, S. Tongay, A. Zettl, and F. Wang. Imaging of pure spin-valley diffusion current in ws_2-wse_2 heterostructures. *Science*, 360(6391):893–896, may 2018.

[13] F. Withers, O. Del Pozo-Zamudio, S. Schwarz, S. Dufferwiel, P. M. Walker, T. Godde, A. P. Rooney, A. Gholinia, C. R. Woods, P. Blake, S. J. Haigh, K. Watanabe, T. Taniguchi, I. L. Aleiner, A. K. Geim, V. I. Fal'ko, A. I. Tartakovskii, and K. S. Novoselov. Wse_2 light-emitting

tunneling transistors with enhanced brightness at room temperature. *Nano Letters*, 15(12):8223–8228, nov 2015.

[14] D. Unuchek, A. Ciarrocchi, A. Avsar, K. Watanabe, T. Taniguchi, and A. Kis. Room-temperature electrical control of exciton flux in a van der waals heterostructure. *Nature*, 560(7718):340–344, jul 2018.

[15] H. Fang, S. Chuang, T. C. Chang, K. Takei, T. Takahashi, and A. Javey. High-performance single layered wse_2 p-FETs with chemically doped contacts. *Nano Letters*, 12(7):3788–3792, jun 2012.

[16] N. R. Pradhan, D. Rhodes, S. Memaran, J. M. Poumirol, D. Smirnov, S. Talapatra, S. Feng, N. Perea-Lopez, A. L. Elias, M. Terrones, P. M. Ajayan, and L. Balicas. Hall and field-effect mobilities in few layered p-wse_2 field-effect transistors. *Scientific Reports*, 5(1), mar 2015.

[17] M. Chhowalla, D. Jena, and H. Zhang. Two-dimensional semiconductors for transistors. *Nature Reviews Materials*, 1(11), aug 2016.

[18] F. Schwierz, J. Pezoldt, and R. Granzner. Two-dimensional materials and their prospects in transistor electronics. *Nanoscale*, 7(18):8261–8283, 2015.

[19] Z. Cai, B. Liu, X. Zou, and H. M. Cheng. Chemical vapor deposition growth and applications of two-dimensional materials and their heterostructures. *Chemical Reviews*, 118(13):6091–6133, jan 2018.

[20] M. Samadi, N. Sarikhani, M. Zirak, H. Zhang, H. L. Zhang, and A. Z. Moshfegh. Group 6 transition metal dichalcogenide nanomaterials: synthesis, applications and future perspectives. *Nanoscale Horizons*, 3(2):90–204, 2018.

[21] S. Li, S. Wang, D. M. Tang, W. Zhao, H. Xu, L. Chu, Y. Bando, D. Golberg, and G. Eda. Halide-assisted atmospheric pressure growth of large wse_2 and ws_2 monolayer crystals. *Applied Materials Today*, 1(1):60–66, nov 2015.

[22] J. K. Huang, J. Pu, C. L. Hsu, M. H. Chiu, Z. Y. Juang, Y. H. Chang, W. H. Chang, Y. Iwasa, T. Takenobu, and L. J. Li. Large-area synthesis of highly crystalline wse_2 monolayers and device applications. *ACS Nano*, 8(1):923–930, dec 2013.

[23] S. M. Eichfeld, L. Hossain, Y. C. Lin, A. F. Piasecki, B. Kupp, A. G. Birdwell, R. A. Burke, N. Lu, X. Peng, J. Li, A. Azcatl, S. McDonnell, R. M. Wallace, M. J. Kim, T. S. Mayer, J. M. Redwing, and J. A. Robinson. Highly scalable, atomically thin wse_2 grown via metal-organic chemical vapor deposition. *ACS Nano*, 9(2):2080–2087, feb 2015.

[24] L. Loh, Z. Zhang, M. Bosman, and G. Eda. Substitutional doping in 2d transition metal dichalcogenides. *Nano Research*, 14(6):1668–1681, aug 2020.

[25] K. Zhang and J. Robinson. Doping of two-dimensional semiconductors: A rapid review and outlook. *MRS Advances*, 4(51-52):2743–2757, sep 2019.

[26] S. Feng, Z. Lin, X. Gan, R. Lv, and M. Terrones. Doping two-dimensional materials: ultra-sensitive sensors, band gap tuning and ferromagnetic monolayers. *Nanoscale Horizons*, 2(2):72–80, 2017.

[27] H. Gao, J. Suh, M. C. Cao, A. Y. Joe, F. Mujid, K. H. Lee, S. Xie, P. Poddar, J. U. Lee, K. Kang,

P. Kim, D. A. Muller, and J. Park. Tuning electrical conductance of mos_2 monolayers through substitutional doping. *Nano Letters*, 20(6):4095–4101, may 2020.

[28] K. Zhang, D. D. Deng, B. Zheng, Y. Wang, F. K. Perkins, N. C. Briggs, V. H. Crespi, and J. A. Robinson. Tuning transport and chemical sensitivity via niobium doping of synthetic mos_2. *Advanced Materials Interfaces*, 7(18):2000856, aug 2020.

[29] K. Zhang, B. M. Bersch, J. Joshi, R. Addou, C. R. Cormier, C. Zhang, K. Xu, N. C. Briggs, K. Wang, S. Subramanian, K. Cho, S. Fullerton-Shirey, R. M. Wallace, P. M. Vora, and J. A. Robinson. Tuning the electronic and photonic properties of monolayer mos_2 via in situ rhenium substitutional doping. *Advanced Functional Materials*, 28(16):1706950, feb 2018.

[30] S. K. Pandey, H. Alsalman, J. G. Azadani, N. Izquierdo, T. Low, and S. A. Campbell. Controlled p-type substitutional doping in large-area monolayer wse_2 crystals grown by chemical vapor deposition. *Nanoscale*, 10(45):21374–21385, 2018.

[31] S. J. Yun, D. L. Duong, D. M. Ha, K. Singh, T. L. Phan, W. Choi, Y. M. Kim, and Y. H. Lee. Ferromagnetic order at room temperature in monolayer ws_2 semiconductor via vanadium dopant. *Advanced Science*, 7(9):1903076, mar 2020.

[32] R. Mukherjee, H. J. Chuang, M. R. Koehler, N. Combs, A. Patchen, Z. X. Zhou, and D. Mandrus. Substitutional electron and hole doping of wse_2: Synthesis, electrical characterization, and observation of band-to-band tunneling. *Physical Review Applied*, 7(3):034011, mar 2017.

[33] H. R. Rasouli, N. Mehmood, O. Çakıroğlu, and T. S. Kasırga. Real time optical observation and control of atomically thin transition metal dichalcogenide synthesis. *Nanoscale*, 11(15):7317–7323, 2019.

[34] B. Liu, M. Fathi, L. Chen, A. Abbas, Y. Ma, and C. Zhou. Chemical vapor deposition growth of monolayer wse_2 with tunable device characteristics and growth mechanism study. *ACS Nano*, 9(6):6119–6127, may 2015.

[35] Y. C. Lin, B. Jariwala, B. M. Bersch, K. Xu, Y. Nie, B. Wang, S. M. Eichfeld, X. Zhang, T. H. Choudhury, Y. Pan, R. Addou, C. M. Smyth, J. Li, K. Zhang, M. A. Haque, S. Fölsch, R. M. Feenstra, R. M. Wallace, K. Cho, S. K. Fullerton-Shirey, J. M. Redwing, and J. A. Robinson. Realizing large-scale, electronic-grade two-dimensional semiconductors. *ACS Nano*, 12(2):965–975, jan 2018.

[36] H. Kim, G. H. Ahn, J. Cho, M. Amani, J. P. Mastandrea, C. K. Groschner, D. H. Lien, Y. Zhao, J. W. Ager, M. C. Scott, D. C. Chrzan, and A. Javey. Synthetic wse_2 monolayers with high photoluminescence quantum yield. *Science Advances*, 5(1), jan 2019.

[37] A. S. Bandyopadhyay, N. Adhikari, and A. B. Kaul. Quantum multibody interactions in halide-assisted vapor-synthesized monolayer wse_2 and its integration in a high responsivity photodetector with low-interface trap density. *Chemistry of Materials*, 31(23):9861–9874, nov 2019.

[38] W. Zhao, Z. Ghorannevis, K. K. Amara, J. R. Pang, M. Toh, X. Zhang, C. Kloc, P. H. Tan, and G. Eda. Lattice dynamics in mono- and few-layer sheets of ws_2 and wse_2. *Nanoscale*, 5(20):9677, 2013.

[39] H. Terrones, E. Del Corro, S. Feng, J. M. Poumirol, D. Rhodes, D. Smirnov, N. R. Pradhan,

Z. Lin, M. A. T. Nguyen, A. L. Elías, T. E. Mallouk, L. Balicas, M. A. Pimenta, and M. Terrones. New first order raman-active modes in few layered transition metal dichalcogenides. *Scientific Reports*, 4(1), feb 2014.

[40] E. del Corro, H. Terrones, A. Elias, C. Fantini, S. Feng, M. A. Nguyen, T. E. Mallouk, M. Terrones, and M. A. Pimenta. Excited excitonic states in 1l, 2l, 3l, and bulk wse_2 observed by resonant raman spectroscopy. *ACS Nano*, 8(9):9629–9635, sep 2014.

[41] M. Yamamoto, S. Dutta, S. Aikawa, S. Nakaharai, K. Wakabayashi, M. S. Fuhrer, K. Ueno, and K. Tsukagoshi. Self-limiting layer-by-layer oxidation of atomically thin wse_2. *Nano Letters*, 15(3):2067–2073, feb 2015.

[42] M. Yamamoto, S. Nakaharai, K. Ueno, and K. Tsukagoshi. Self-limiting oxides on wse_2 as controlled surface acceptors and low-resistance hole contacts. *Nano Letters*, 16(4):2720–2727, mar 2016.

[43] B. Liu, Y. Ma, A. Zhang, L. Chen, A. N. Abbas, Y. Liu, C. Shen, H. Wan, and C. Zhou. High-performance wse_2 field-effect transistors via controlled formation of in-plane heterojunctions. *ACS Nano*, 10(5):5153–5160, may 2016.

[44] J. Seo, K. Cho, W. Lee, J. Shin, J. K. Kim, J. Kim, J. Pak, and T. Lee. Effect of facile p-doping on electrical and optoelectronic characteristics of ambipolar wse_2 field-effect transistors. *Nanoscale Research Letters*, 14(1), sep 2019.

[45] A. V. Stier, N. P. Wilson, G. Clark, X. Xu, and S. A. Crooker. Probing the influence of dielectric environment on excitons in monolayer wse_2: Insight from high magnetic fields. *Nano Letters*, 16(11):7054–7060, oct 2016.

[46] P. Zhao, A. Azcatl, P. Bolshakov, J. Moon, C. L. Hinkle, P. K. Hurley, R. M. Wallace, and C. D. Young. Effects of annealing on top-gated mos_2 transistors with hfo_2 dielectric. *Journal of Vacuum Science & Technology B, Nanotechnology and Microelectronics: Materials, Processing, Measurement, and Phenomena*, 35(1):01A118, jan 2017.

[47] H. Qiu, L. Pan, Z. Yao, J. Li, Y. Shi, and X. Wang. Electrical characterization of back-gated bi-layer mos_2 field-effect transistors and the effect of ambient on their performances. *Applied Physics Letters*, 100(12):123104, mar 2012.

[48] J. H. Kim, J. Lee, J. H. Kim, C. C. Hwang, C. Lee, and J. Y. Park. Work function variation of mos_2 atomic layers grown with chemical vapor deposition: The effects of thickness and the adsorption of water/oxygen molecules. *Applied Physics Letters*, 106(25):251606, jun 2015.

[49] J. Kang, W. Liu, and K. Banerjee. High-performance mos_2 transistors with low-resistance molybdenum contacts. *Applied Physics Letters*, 104(9):093106, mar 2014.

[50] B. W. H. Baugher, H. O. H. Churchill, Y. Yang, and P. Jarillo-Herrero. Intrinsic electronic transport properties of high-quality monolayer and bilayer mos_2. *Nano Letters*, 13(9):4212–4216, aug 2013.

[51] P. Chen, J. Pan, W. Gao, B. Wan, X. Kong, Y. Cheng, K. Liu, S. Du, W. Ji, C. Pan, and Z. L. Wang. Anisotropic carrier mobility from 2h wse_2. *Advanced Materials*, page 2108615, jan 2022.

[52] W. Liu, J. Kang, D. Sarkar, Y. Khatami, D. Jena, and K. Banerjee. Role of metal contacts

in designing high-performance monolayer n-type wse_2 field effect transistors. *Nano Letters*, 13(5):1983–1990, apr 2013.

[53] H. C. P. Movva, A. Rai, S. Kang, K. Kim, B. Fallahazad, T. Taniguchi, K. Watanabe, E. Tutuc, and S. K. Banerjee. High-mobility holes in dual-gated wse_2 field-effect transistors. *ACS Nano*, 9(10):10402–10410, sep 2015.

6

FINAL REMARKS AND OUTLOOK

The largest part of this thesis was dedicated to the novel method of photo-oxidation of HfS_2 and to the use of the resulting high-k HfO_2 in novel optoelectronic devices. Each of the chapters discussing the applications of the photogenerated oxide presented a novel idea and/or demonstrated a fully characterised prototype device where their advantages over current technology were highlighted.

Specifically, Chapter 3 began by laying the foundations of the mechanism of photo-oxidation of HfS_2. There, the importance of the importance of the presence of aqueous oxygen in the environment where the photo-oxidation takes place was emphasised and the chemical reactions of reduction-oxidation that lead to the formation of HfO_2 were presented. Furthermore, the second half of the third chapter was dedicated to the contrast study of an area where the oxidation was not uniform. By varying the laser power along a displacement axis, it is possible to end up with different degrees of oxidation along the path followed. The analysis was based on the fact that HfS_2 is almost entirely transparent in the visual range, thanks to its wide bandgap, and showed a correlation between the optical contrast along a HfO_2 gradient and the level of oxidation. This could be a very important point as it would give a whole new level of control in the process, resulting in a 2D oxide with graded dielectric properties. A two-dimensional dielectric with a gradient of refractive index could be incorporated in van der Waals (vdW) heterostructures and act as an exciton waveguide.

Subsequently, the first nanoelectronic devices incorporating HfO_2 were presented in Chapter 4 and included resistive switching Random Access Memories (ReRAM) and optoelectronic devices where both light detection and emission are possible. This chapter began with a characterisation of the insulating properties of HfO_2, where the

breakdown field of the oxide was found to be $\sim 0.6\,\mathrm{V\,nm^{-1}}$ and its dielectric constant $\sim$ 15. The ReRAM devices presented here exhibited ambipolar switching and maintained a steady behaviour for 100 SET/RESET cycles, while the largest memory window reached $R_{HRS}/R_{LRS} \sim 10^4$. Additionally, an optoelectronic device of quantum well architecture was presented where light emission and detection were possible in the same device. The electroluminescence (EL) intensities were comparable to those that use hBN barriers but this device exhibited 10^6 times faster photodetection than planar MoS_2 ones. All these showed the compatibility of the photogenerated oxide with other 2D materials and open a new path for application in semi-transparent and flexible vdW nanoelectronics.

Finally, the optoelectronic characterisation FETs with a channel of monolayer WSe_2 grown with a novel CVD method was presented in Chapter 5. After an initial discussion of the novelties of the growth process, the enhancement of transport properties via vacuum and ambient annealing and the optoelectronic characterisation of the devices followed. The examined devices showed high ON/OFF ratios ($\sim 10^5$) and carrier mobility (up to $50\,\mathrm{cm^2\,V^{-1}\,s^{-1}}$ upon vacuum annealing), showing a maximum of photoresponsivity at $\lambda = 610\,\mathrm{nm}$. Additionally, the results of Hall measurements performed in order to determine the intrinsic carrier doping, were discussed. An average intrinsic n-type doping with charge density of $n_{Hall} > 5 \times 10^{15}\,\mathrm{m^{-2}}$ were calculated, confirming that it is the first reported CVD-grown monolayer WSe_2 with an n-type doping.

PUBLICATIONS

The ideas and data presented in this thesis are subject of the following publications:

- N. Peimyoo, M. D. Barnes, Jake D. Mehew, A. De Sanctis, I.Amit, J. Escolar, K. A. Anastasiou, A. P. Rooney, S. J. Haigh, S. Russo, M. F. Craciun and F. Withers. *Laser writable high-k dielectric for van der Waals nano-electronics.* Science Advances, 2019.

- M. Och, K. A. Anastasiou, I. Leontis, G. Z. Zemignani, P. Palczynski, A. Mostaed, M. Sokolikova, E. M. Alexeev, A. I. Tartakovskii, J. Lischner, P. Nellist, S. Russo, and C. Mattevi. *Synthesis of monolayer n-doped WSe_2 from solid state inorganic precursors.* Nanomaterials, under review (2022).